

Patrick Falk, BSc

A visual-based particle counter: simulation and design

MASTER THESIS

For obtaining the academic degree
Diplom-Ingenieur

Master Programme of
Technical Physics



Graz University of Technology

Supervisor:

Ao.Univ.-Prof. Dipl.-Ing. Dr.techn. Roland Resel
Institute of Solid State Physics

Graz, June 2014

Deutsche Fassung:
Beschluss der Curricula-Kommission für Bachelor-, Master- und Diplomstudien vom 10.11.2008
Genehmigung des Senates am 1.12.2008

EIDESSTÄTTLICHE ERKLÄRUNG

Ich erkläre an Eides statt, dass ich die vorliegende Arbeit selbstständig verfasst, andere als die angegebenen Quellen/Hilfsmittel nicht benutzt, und die den benutzten Quellen wörtlich und inhaltlich entnommenen Stellen als solche kenntlich gemacht habe.

Graz, am

.....
(Unterschrift)

Englische Fassung:

STATUTORY DECLARATION

I declare that I have authored this thesis independently, that I have not used other than the declared sources / resources, and that I have explicitly marked all material which has been quoted either literally or by content from the used sources.

.....
date

.....
(signature)

My special thanks and appreciation go to my parents Christa and Anton Falk, who kept me grounded during my whole studies. Without their encouragement I would never have been able to achieve my goals.

I want to thank my adviser at AVL List Dr. Alexander Bergmann for initiating this thesis and Dr. Roland Resel for supervising me on behalf of TU Graz. Furthermore, I want to thank my colleagues at work for their advice and assistance during the whole project.

Abstract

In the last decade particle-number counting techniques have become important in exhaust measurements of combustion engines due to new legal measures. Since the size distribution of generated soot particles in common diesel engines went down to a range of 100 nm, the concentration of respirable dust became the crucial value in terms of exhaust emission standards. This thesis discusses the theoretical feasibility for a visual-based particle counter using linear and two-dimensional detector arrays to increase the current counting limitation of 20000 particles per cm^3 . The work focuses on the simulation and design of different optical setups in the bright and dark field mode and their resulting requirements for detectors and light sources. General simulations excluding optical effects showed a theoretical gain of the counting limit of up to 500% applying two-dimensional detector arrays. Using a single linear detector resulted in a performance gain of 150%. In terms of dark field imaging techniques, setups like telecentric lens or certain alignments of detector and light source using a simple imaging optic showed low feasibility. Either the generated signal is in the noise range of the detector or the required read-out frequency is not achievable by two-dimensional arrays. Additionally, high demands on the laser beam profile proved necessary for dark field setups. Instead an optical alignment in the bright field mode including an aperture stop indicated to be implementable. Thus an experiment was set up and first particles were detected successfully.

CONTENTS

Contents

| | | |
|----------|---|-----------|
| 1 | Introduction | 1 |
| 2 | Determination of counting limit | 4 |
| 2.1 | Theoretical considerations | 4 |
| 2.1.1 | Velocity and density distribution | 4 |
| 2.1.2 | Coincidence | 7 |
| 2.2 | Simulation | 9 |
| 2.3 | Results | 13 |
| 2.3.1 | One linear detector (1D) | 15 |
| 2.3.2 | Two linear detectors (2D) | 18 |
| 2.3.3 | Single photo diode (0D) | 22 |
| 2.3.4 | Comparison: Single photo diode (0D) and two linear detectors (2D) | 23 |
| 2.4 | Summary | 25 |
| 3 | Optical considerations | 27 |
| 3.1 | Fundamentals | 27 |
| 3.2 | <i>Radiant Zemax</i> | 28 |
| 3.3 | Characteristics of a single decane particle | 29 |
| 3.4 | Optical design | 32 |
| 4 | Dark field | 34 |
| 4.1 | Imaging setups | 34 |
| 4.1.1 | Simple imaging using two aspherical lenses | 35 |
| 4.1.2 | Telecentric lens setup | 37 |
| 4.1.3 | Orthogonal alignment | 39 |
| 4.1.4 | Scheimpflug alignment | 41 |
| 4.1.5 | Fiber bundles | 43 |
| 4.2 | Detection | 45 |
| 4.2.1 | Responsivity | 47 |
| 4.2.2 | Read-out frequency | 50 |
| 4.3 | Illumination | 53 |
| 4.3.1 | Power | 53 |
| 4.3.2 | Collimation | 53 |
| 4.4 | Summary | 56 |
| 5 | Bright field | 58 |

CONTENTS

| | | |
|----------|----------------------------------|-----------|
| 5.1 | Imaging setups | 58 |
| 5.1.1 | Aperture stop setup | 58 |
| 5.1.2 | Fiber bundles | 60 |
| 5.2 | Detection | 60 |
| 5.2.1 | Responsivity | 61 |
| 5.2.2 | Read-out frequency | 63 |
| 5.3 | Illumination | 64 |
| 5.3.1 | Power | 64 |
| 5.3.2 | Collimation | 64 |
| 5.4 | Summary | 65 |
| 6 | Experimental verification | 66 |
| 6.1 | Setup | 66 |
| 6.2 | Results | 70 |
| 7 | Conclusion | 75 |
| 8 | Appendix | 76 |

1 Introduction

The condensation particle counter has now been a system to count soot particles in the automotive industry for many decades. Small particles, which are not big enough to get detected directly by optical imaging methods, can initiate nucleation in a supersaturated environment. Thus, droplets are created around the particles which can be detected optically more easily because of their enlarged size. To produce the nucleation, different techniques like adiabatic expansion, thermal diffusion or mixing hot with cold gas have been developed. Aitken first mentioned measuring particles by using adiabatic expansion to initiate condensation nuclei. In the 1950's General Electric's Research Laboratory invented an automated photoelectric condensation nuclei counter, which creates supersaturation by rapid expansion. Nowadays condensation particle counters, like the ones developed by *TSI*, cool the saturated gas down to reach supersaturation and initiate nucleation. Next figure illustrates the process flow of this common principle. [1] [2] [3] [4] [5]

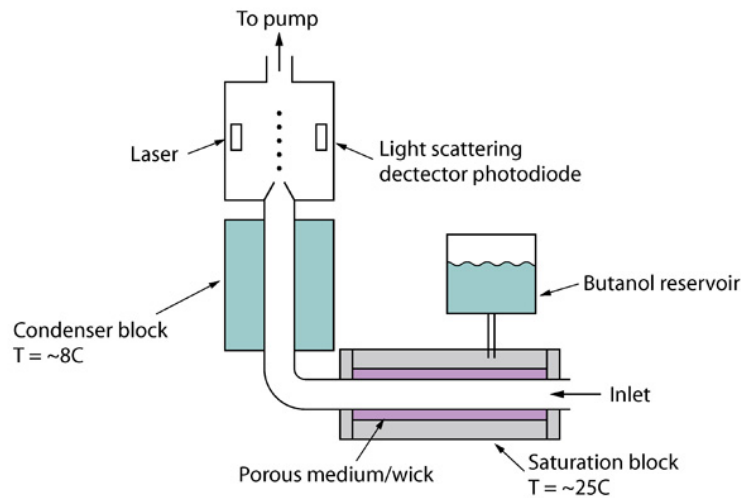


Figure 1: Schematic of the condensation particle counter by *TSI* [10]. It basically consists of three parts: the saturation block, the condenser block and the measuring cell.

In the saturation block the pre-treated aerosol is mixed with the gaseous working fluid, for example decane or butanol. The vapor streams out of a wick or a porous medium until the system is saturated. In a next step the stream flows into the condenser block where it is cooled down. The system is now in a supersaturated state and the gaseous operating medium condenses on the particles which work as condensation nuclei. The size of the particles can be controlled precisely by the time they remain in the condenser block. In the *TSI*-setup the length of the condenser is chosen to generate particles with a diameter of approximately

1 INTRODUCTION

$5\ \mu\text{m}$. The initial size of the particles ($\sim 100\ \text{nm}$) does not affect the final diameter, since the radius grows by a factor of 50. This ends up in a much bigger final volume of the sphere compared to the initial, since the volume varies with the cube of radius. After the vapor condensation the particles pass through a nozzle, to detect the particles consecutively. In the measuring cell the particles pass a laser beam and scatter light in all room directions. Two condenser lenses focus the stray light on a single photo diode. The main beam is stopped by a beam dump, which is positioned in front of the lenses. If no particle passes the beam no signal is generated on the diode. Thus, the setup is working in the dark field mode. Each time a particle passes the beam light is scattered and a voltage pulse on the diode is created. This pulse is used in signal analysis for counting.[1] Condensation particle counters like discussed in this section are able to measure particle densities up to $20000\ \text{particles} / \text{cm}^{-3}$. [6] This counting limit is mainly determined by the probability of coincidence. It is the number of events the signal analysis cannot distinguish between two particles. An event like this occurs when two particles pass the laser beam within a critical time span. This time span is determined by the comparator threshold defined in the signal analysis (see figure 2).

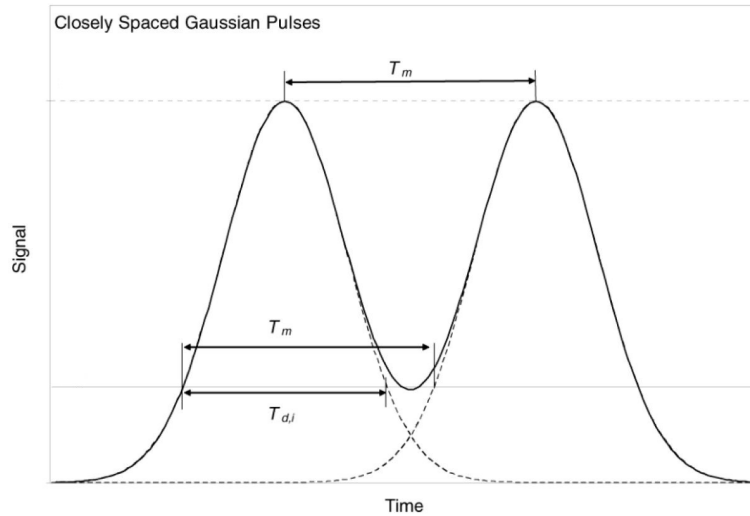


Figure 2: Minimum time span T_m for two detectable pulses ($T_{d,i}$ width of pulse i at threshold level) in a comparator system. Two particles which generate signal within this certain time duration cannot be separated.[11]

Since particle number measurements get more important with recent exhaust legislation, higher counting limits need to be achieved. This thesis discuss the feasibility of new visual-based counting principles to measure higher particle densities. The most fundamental difference compared to the current used measuring cell will be the omission of the nozzle. Therefore the illuminated particles should get imaged on detector arrays instead of a simple

1 INTRODUCTION

photo diode. Since common photo arrays experienced a dramatic gain in performance in the last years different optical imaging setups are studied. This enables new dimensions in spatial resolution and thus countable particle densities in much higher ranges. Two particles which pass the illuminated area within the critical time span but at different positions should be imaged separately on detector arrays. Thus, coincidence cases as shown in figure 2 should be avoided.

In the following the determination of the theoretical limit of a setup including detectors arrays is shown. Different optical setups in terms of alignment, detector and illumination requirements are discussed, both in the dark field and in the bright field mode. The feasibility of a certain imaging setup is shown in an experimental verification.

2 Determination of counting limit

2.1 Theoretical considerations

2.1.1 Velocity and density distribution

The velocity and density distribution are important parameters to describe the flow of particles within a pipe. For the condensation particle counter these distributions are not known. As a first step it is assumed that the motion of the particles is laminar. Thus, the velocity distribution $v(r)$ is given by the average velocity \bar{v} and the radius of the pipe R (equation 1).

$$v(r) = 2\bar{v} \left(1 - \frac{r^2}{R^2} \right) \quad (1)$$

The velocity v_{\max} of the fastest particle can be determined with equation 2.

$$v_{\max} = 2\bar{v} \quad (2)$$

In figure 3, left picture the typical cross section velocity of a laminar flow is shown.

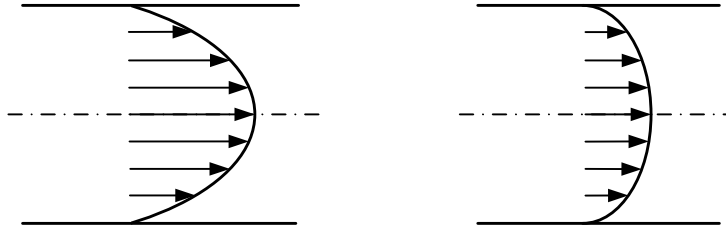


Figure 3: Laminar (left part) and turbulent (right part) velocity distribution within a pipe.

If the flow becomes turbulent the velocity distribution becomes flatter and flatter (see figure 3, right picture). Mathematically this can be described by equation 3, where the exponent n is a function of the Reynolds-number Re . The Reynolds-number is used to distinguish a laminar from a turbulent flow.

$$v(r) = \bar{v} \frac{(n+1)(2n+1)}{2n^2} \left(1 - \frac{r}{R} \right)^{1/n} \quad (3)$$

With a higher exponent n the laminar flow is distributed more uniformly. Thus a laminar velocity distribution results in the greatest possible particle velocity v_{\max} . Fast particles require higher time resolutions and thus result in less counting performance. On these grounds a laminar velocity distribution can be assumed to be the worst case in terms of counting limit.

2 DETERMINATION OF COUNTING LIMIT

Following considerations and simulations are performed for a laminar velocity distribution.

The flow rate Q , which is defined as the passing volume V per time t , can be calculated by integrating the velocity distribution $v(r)$ above the pipe cross section A . [7] [8] [9]

$$Q = \frac{dV}{dt} = \dot{V} = \int_{(A)} d\dot{V} = \int_{(A)} dA \cdot v(r) = 2\pi \int_{(A)} dr \cdot r \cdot v(r) \quad (4)$$

The flow rate Q in the condensation particle counter is constant and known as: [6]

$$\dot{V} = 1 \frac{\text{l}}{\text{min}}$$

Thus, the flow velocity \bar{v} in a $\varnothing 20$ mm pipe (area $A = \pi \text{ cm}^2$) can be calculated by inserting equation 1 in equation 4 to:

$$\bar{v}_{\varnothing 20} = \frac{\dot{V}}{4\pi \int_0^R \left(r - \frac{r^3}{R^2}\right) dr} = 0.053 \frac{\text{m}}{\text{s}} = 5.3 \frac{\text{cm}}{\text{s}}$$

The flow velocity in the current system, using a $\varnothing 0.5$ mm nozzle (area $A = 0.2 \text{ mm}^2$) adds up to:

$$\bar{v}_{\varnothing 0.5} = 84.8 \frac{\text{m}}{\text{s}} = 8480 \frac{\text{cm}}{\text{s}}$$

The velocity drops with a factor 1600 in a system without nozzle! Thus, the velocity of the fastest particle in the laminar system without nozzle is determined by equation 2 to:

$$v_{\varnothing 20, \text{max}} = 10.6 \frac{\text{cm}}{\text{s}}$$

This adds up to a time

$$t_{\text{min}} = 9.4 \times 10^{-5} \text{ s} \approx 0.1 \text{ ms}$$

for the fastest particle to move through a $10 \mu\text{m}$ illuminated area. This dwell time defines important requirements the detector has to fulfill. On the one hand the detector has to read-out with a sufficient high frequency to capture a particle at least once. On the other hand high read-out frequencies result in short exposure times, which make high demands on the sensitivity of the detector (see section 4.2).

To get a first impression of the general limits of detector array setups, the sample rate is primarily not considered. This means that simulations are at first independent of detector limits. Therefore, the velocity distribution does not affect the coincidence probability, since the time resolution of the detector system is assumed to be high enough. However, the most

2 DETERMINATION OF COUNTING LIMIT

important criterion in terms of coincidence probability is the average particle density within the pipe. It mainly determines the probability of a coincidence event. A second important influence on the probability of a coincidence cases is the local density distribution. It defines the particle density as a function of radius within the pipe. Due to thermal effects or other external influences, like pre-treatment of the gas or cold pipe walls (see thermophoresis), particles are distributed in several ways. For centered, laminar-like distributions most particles are placed along the symmetric axis of the pipe. If the flow becomes turbulent the particles are distributed in more uniform way over the pipe cross-section. Since the imaged distance on the detector varies with the radius (see figure 4), the density distribution becomes even more important.

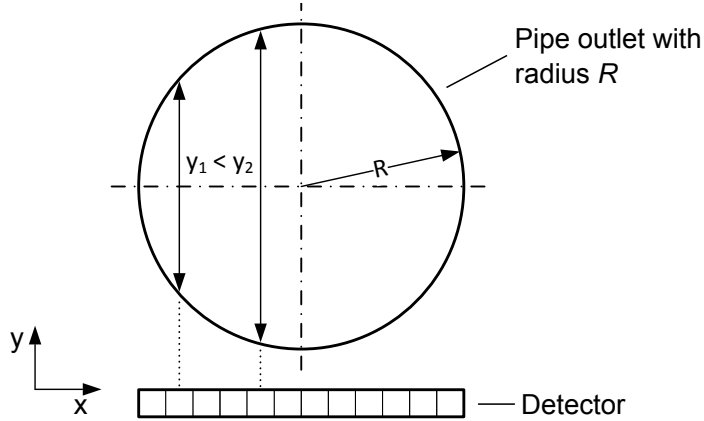


Figure 4: Imaged distance y_i on the detector. The probability of coincidence cases at pixels along the symmetry line in y -direction is higher than the one of pixels on the brink.

Hence, the simulations were carried out for different densities and distributions i.e. in formula 5:

$$\rho(r) = 1 - \left(\frac{r}{R}\right)^n ; n = 2, 6, 0 \quad (5)$$

A distribution with exponent $n = 2$ describes the laminar case where the density is concentrated along the symmetric axis of the pipe and decreases parabolically with the radius r . In the case of $n = 0$ the particles are distributed uniformly along the whole pipe cross section. $n = 6$ belongs to a flattened distribution somewhere in between the two cases discussed before; equal to a turbulent distribution. An effect which contributes to a flat or uniform distribution is the thermophoresis. If there is a gradient in temperature as it can occur in the condensation particle counter (hot gas and cool pipe walls), particles will be forced to move towards colder regions (see figure 5). For sub-micron sized particles the drift is caused by higher kinetic energies of hot particles and therefore their higher momenta. In case of bigger particles the force, caused by thermophoresis is a consequence of microscopic gas-flow on the

2 DETERMINATION OF COUNTING LIMIT

particle surfaces. [13]

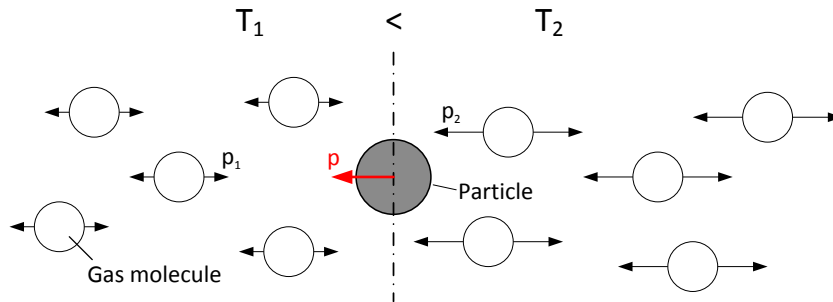


Figure 5: Principle of thermophoresis: Brownian motion of molecules in hotter regions is stronger than in colder region. A particle within the temperature gradient T_1 to T_2 acquires higher kinetic energy from hot molecules than from the cold. This results in an effective momentum p .

Hot gas in a condensation particle counter contributes to a flattened particle distribution within the pipe since the particles move to colder regions (cool pipe walls). In terms of the following considerations the laminar case can be still assumed to be the worst.

2.1.2 Coincidence

A very important part of the simulations is the definition of coincidence cases. While using only one linear image sensor, coincidence occurs when two or more particles are imaged on the same pixel, which means that the particles mask each other (see left part in figure 6).

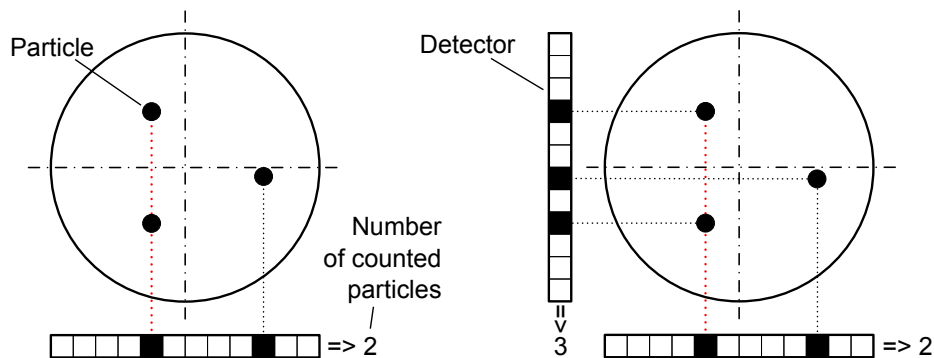


Figure 6: Left part: Coincidence case by using one linear image sensor (one-dimensional detector). The number beside the detector indicates the number of counted particle; Right part: Avoiding coincidence by using two linear detector arrays (two-dimensional detector setup). Since the linear detectors are aligned orthogonal all three particles are counted.

2 DETERMINATION OF COUNTING LIMIT

Since the definition of coincidence cases is a function of spatial resolution or rather the number of pixels, first simulations are based on imaging the particles on a 4000 pixel detector. The size of one pixel matches with the particle size generated in the condensation particle counter ($D = 5 \mu\text{m}$). If the distance of two particles x is less than $15 \mu\text{m}$, they are not imaged separately on a detector array (see figure 7). It is assumed that at least one single pixel in between needs to be totally unexposed.

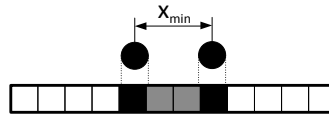


Figure 7: Minimal distance to resolve two particles on a 4000 pixel detector: $x_{min} \geq 15 \mu\text{m}$. Below this distance a single unexposed pixel is not observable.

To determine the counting limit for a two-dimensional detector setup, like it is shown in figure 6, the cross coincidence between both detectors needs to be evaluated. Thus, the definition of the cross coincidence can be divided into two parts:

1. Coincidence occurs when the distance of two particles $r(x, y) < 15 \mu\text{m}$ (see figure 8, left picture).
2. In a special configuration as shown in figure 8, right picture, one of the particles is not counted either.

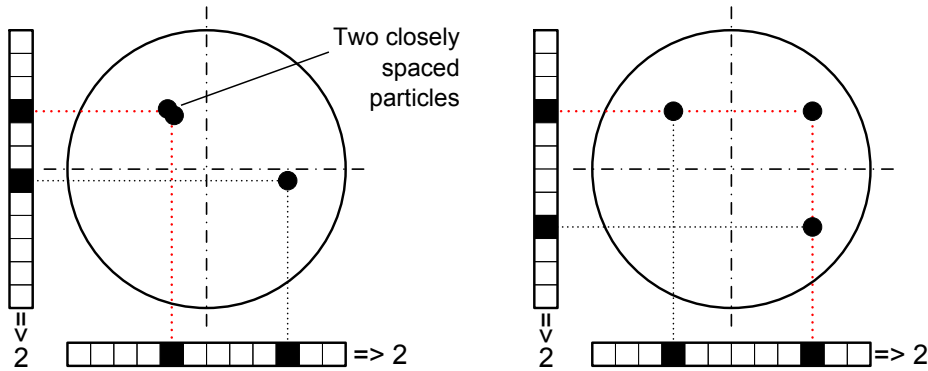


Figure 8: Cross coincidence cases by using two orthogonal linear image sensors. Coincidence only appears for closely spaced particles (left part) or for special alignments of three (or more) particles (right part).

The coincidence probability drops dramatically for a tow-dimensional detector setup. Two particles cannot hide behind each other anymore, except for a view special alignments (see figure 8).

2 DETERMINATION OF COUNTING LIMIT

2.2 Simulation

The aim of the simulations was to determine the amount of relative coincidence cases as a function of the particle density. The relative coincidence is the ratio of missed particles to the total number of passed particles. A typical value in particle measurements is to know which particle density is countable to stay below 10% relative coincidence. This density is designated to be the counting limit, like introduced in the section above. This section describes the structure of the simulation code, which was written in *Matlab*. The parameters of the simulation are discussed in the following:

Particle density, ρ : As was introduced in the section above the particle density (particles/cm³) is the crucial parameter. In the simulations the density was varied to determine the counting limit.

Width of illuminated area, W : Defines the height of the light beam which illuminates the passing particles. The illuminated area was to assumed to be $W = 10 \mu\text{m}$ thick and collimated. In further considerations for section 4.3, this parameter was varied.

Particle diameter, D_{Particle} : The diameter of the particles was assumed to be $D_{\text{Particle}} = 5 \mu\text{m}$.

Pipe diameter, D_{Pipe} : The diameter of the particle outlet for the new setup was assumed to be $D_{\text{Pipe}} = 2 \text{ cm}$. In the existing particle counter a nozzle with a diameter of $D_{\text{Pipe}} = 0.5 \text{ mm}$ is applied.

Pixel size, S : The size of a single sensor element was assumed to be in the range of D_{Particle} : $S = 5 \mu\text{m} \times 5 \mu\text{m}$.

Number of pixels, N : Simulations were performed for a detector with $N = 4000$ pixels. The number of pixel was varied in section 2.3.2.

Radius of coincidence, $R_{\text{Coincidence}}$: The minimum distance of two particles to resolve them. The radius of coincidence is a function of the number of pixels N . Since the particle diameter $D_{\text{Particle}} = 5 \mu\text{m}$ and the piper diameter $D_{\text{Pipe}} = 2 \text{ cm}$ are assumed to be constant the radius of coincidence can be stated as:

$$R_{\text{Coincidence}} = D_{\text{Particle}} + 2 \cdot \frac{D_{\text{Pipe}}}{N}$$

Time steps, T : This parameter defines the number of measurement events. Since the particle density is subjected to statistical fluctuations, T has to set sufficient high to determine an accurate mean value.

2 DETERMINATION OF COUNTING LIMIT

In a first step the particles are placed into a random position on a sufficient fine grid within a defined volume. The position of the particles within the x - y -plane (see figure 4) is evaluated according to the density distribution. Therefore, numbers are sampled from a distribution by using the "Rejection Method":

To generate random numbers within an interval $[a, b]$ out of a probability density function $g(x)$

$$0 \leq g(x) \leq 1, \quad \int_a^b g(x) dx = 1, \quad x \in [a, b] \quad (6)$$

find a another probability density function $h(x)$

$$0 \leq h(x) \leq 1, \quad \int_a^b h(x) dx = 1, \quad (7)$$

and a constant c which satisfies

$$g(x) \leq c \cdot h(x), \quad \forall x \in [a, b]. \quad (8)$$

From this follows that $c \cdot h(x)$ envelopes $g(x)$ in the interval $[a, b]$ (see figure 9).

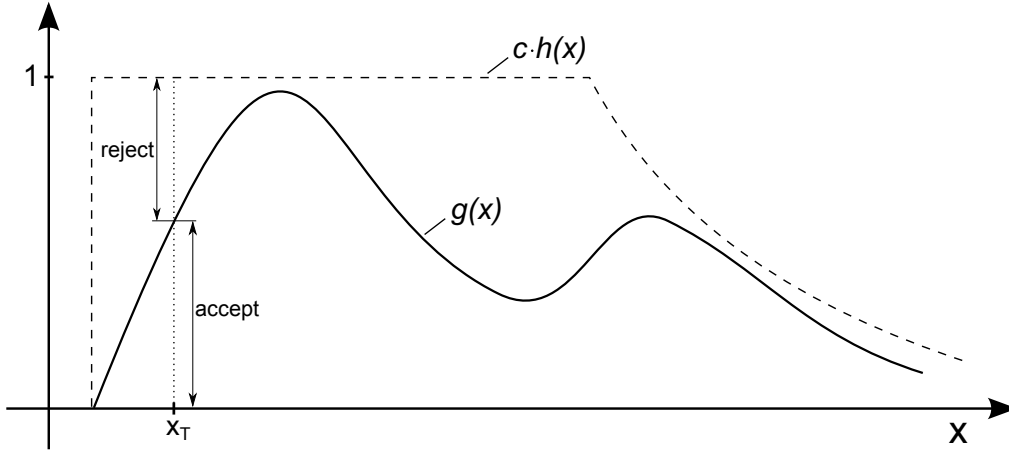


Figure 9: Probability density function $g(x)$ and enveloping function $c \cdot h(x)$. If for a trial random variable x_T from $h(x)$: $r \cdot c \cdot h(x_T) < g(x_T)$, then x_T is accepted; otherwise the variable is rejected.

A way to implement the rejection method in a source code is stated below:

2 DETERMINATION OF COUNTING LIMIT

Algorithm:

```
begin:
  Generate a trial random variable  $x_T$  from  $h(x)$ 
  Generate a uniform random number  $r \in [0, 1]$ 
  if  $r \cdot c \cdot h(x_T) < g(x_T)$  then
    accept  $x_T$ 
  else
    go to begin
  end if [12]
```

The x -, y - and the uniformly distributed z - coordinate are stored in a $3 \times N$ matrix. The radius of the pipe is assumed to be as 1 cm. With equation 9:

$$V = r^2 \pi \cdot h \quad (9)$$

for a cylinder volume V (assumed to be $V = 1 \text{ cm}^3$), the height h can be calculated to:

$$h = \frac{1}{\pi} \text{ cm}$$

Depending on the position $r = r(x, y)$ in the x - y -plane the velocity distribution (equation 1) assigns each particle a certain velocity $v = v(r)$. For each time step the new position of the particles are calculated with formula 10:

$$x(t) = x_0 + t \cdot v \quad (10)$$

x_0 is the position of a particle at time $t = 0$. When a particle leaves the volume, it has to re-enter on the bottom side with newly generated x - and y -coordinates. It is important that the particle is additionally re-evaluated with the velocity distribution (equation 1). Consequently, the probability density function for particles, which re-enter the volume, is defined by:

$$p(r) = \rho(r) \cdot v(r) \quad (11)$$

If a particle is on a grid position within the illuminated area it will be counted. By using the coincidence rules explained above, the number of lost particles is identified. With the average values over a certain number of time steps the ratio between the coincidence cases and passed particles is determined for different densities and distributions. This ratio determines the maximum counting limit. Since the particle distribution within the pipe in the condensation particle counter is not known, first simulations were done for three different kinds of particle-

2 DETERMINATION OF COUNTING LIMIT

density distributions:

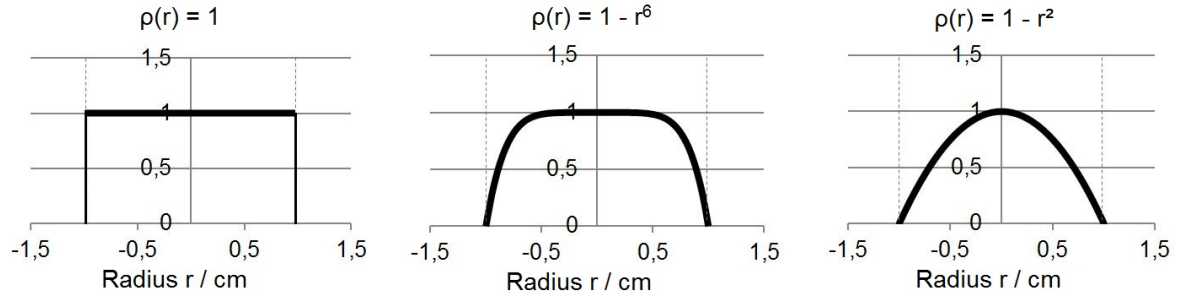


Figure 10: Used particle distributions in simulations. $\rho(r) = 1$ stands for a constant distribution of particles within the plug flow. $\rho(r) = 1 - r^6$ states a turbulent case and $\rho(r) = 1 - r^2$ a laminar distribution. The latter indicates the worst case in terms of coincidence probability since a high amount of particles is located along the symmetric axis.

To ensure a constant flow rate for all particle distributions, usually the areas below the curves are normalized. Since the loop in the rejection method runs till a certain number of particles is accepted, it is not required to normalize the distributions. A normalization would just lead to a other constant c or probability density function $h(x)$.

2 DETERMINATION OF COUNTING LIMIT

2.3 Results

In a first step simulations with high particle densities were done for the particle distributions introduced in the section above. The number of particles within a thin laser band were counted for several time steps. In each of the following three figures (11, 12 and 13) the accumulated particle density as function of the pipe cross section is plotted. This equates to the number of particles which are imaged on a detector element as a function of x -position (see figure 4). Additional particles got counted within a small band along the symmetric axis to verify the density function. Thus, the density function, the determined particle distribution along the axis and the accumulated particle density are plotted. The particle density was defined to be $\rho = 175000$ particles/cm³ to ensure a high number of counting events.

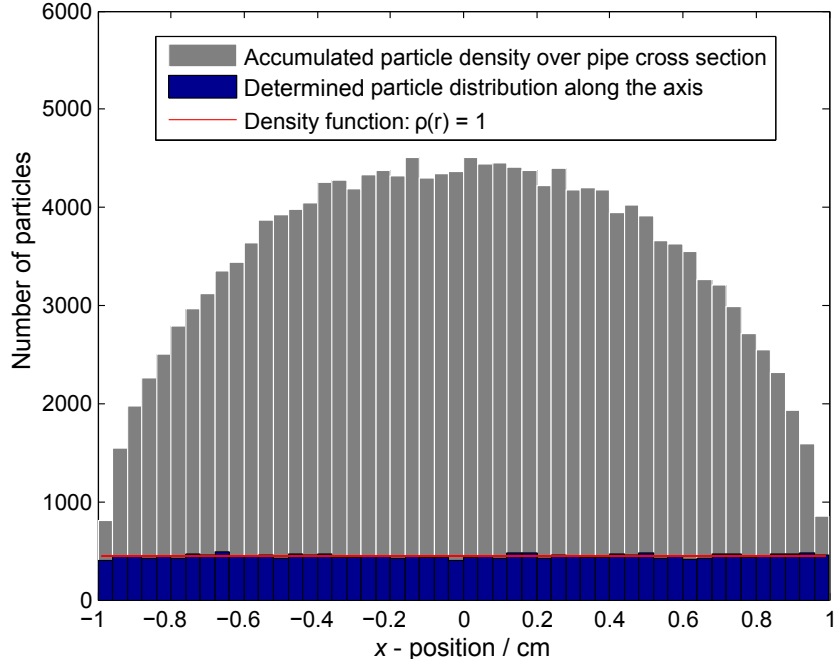


Figure 11: Counted particles as a function of x -position for a given density distribution: $\rho(r) = 1$. The accumulated particle density gives the number of imaged particles on a single detector element. This corresponds to the number of particles along the y -direction as a function of x -coordinate (see figure 4). List of parameters: see appendix (section 8).

Next figure shows the accumulated particle density simulating a turbulent particle distribution for the same amount of particles ($\rho = 175000$ particles/cm⁻³). The accumulated distribution is narrower since the particles are not distributed uniformly within pipe anymore ($\rho(r) = 1 - r^6$). The determined particle distribution along the axis indicates the turbulent distribution of particles within the pipe.

2 DETERMINATION OF COUNTING LIMIT

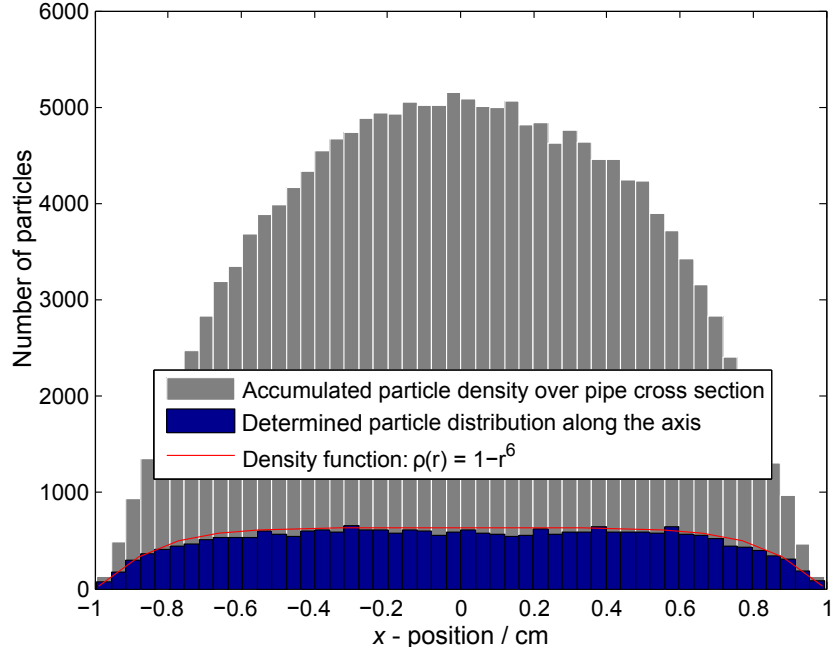


Figure 12: Counted particles as a function of pipe cross-section for a turbulent density distribution: $\rho(r) = 1 - r^6$. The accumulated particle density narrows compared to the uniform distribution in figure 11. This results in a high number of coincidence cases. List of parameters: see appendix (section 8).

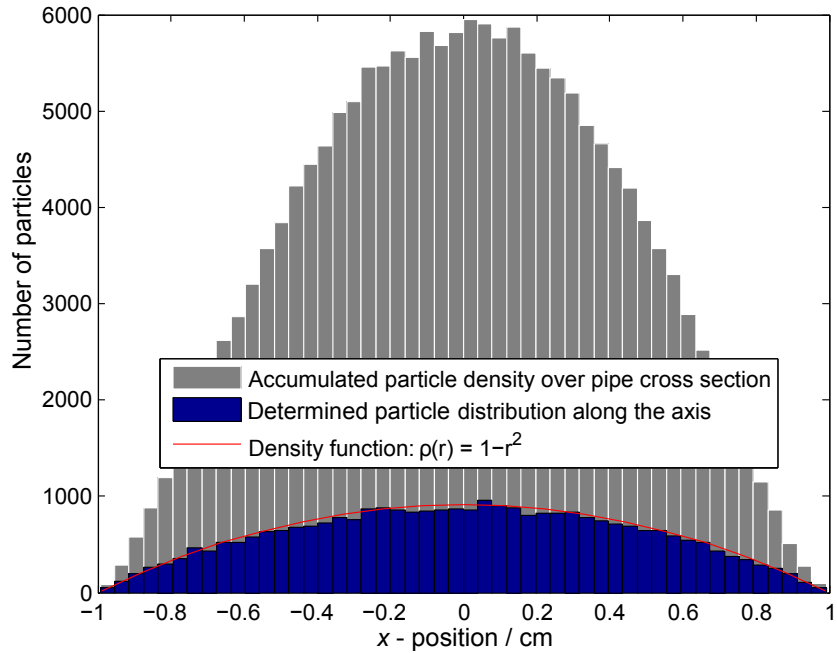


Figure 13: Accumulated particle density as a function of pipe cross-section for a laminar density distribution: $\rho(r) = 1 - r^2$. List of parameters: see appendix (section 8).

2 DETERMINATION OF COUNTING LIMIT

As depicted in figure 13 the laminar-like distribution $\rho(r) = 1 - r^2$ is the one with the highest density along the symmetric axis perpendicular to the detector. Thus the accumulated particle density shows a narrower distribution than for the turbulent or constant one. Hence the probability for coincidence events is highest for the laminar distribution. This results suggest that a constant distribution will result in a higher counting rate than a laminar particle distribution. In the following section simulations were performed for linear detector arrays in one- and two-dimensional alignments (see figure 6). To compare these results with the existing setup, simulations were performed applying a single photo diode as well (zero-dimensional setup).

2.3.1 One linear detector (1D)

In this section the theoretical counting limit is determined for a single linear detector with 4000 pixels (see left part in figure 6). The counting limit is defined as the density at 10% relative coincidence. To determine this density the relative coincidence was calculated for a sufficient high number of time steps T for certain particle densities. The averaged densities were fitted and the counting limit computed.

In figure 14 the determined relative coincidences are plotted for certain particle densities distributed uniformly ($\rho(r) = 1$). These data points are fitted with following function:

$$y(x) = a \left(1 - e^{-bx}\right) \quad (12)$$

This function describes the relation between counting limit and particle density in a one-dimensional detector setup very well. At very high densities the pipe is more or less totally filled up with particles and a coincidence event appears almost at every counting event. By using equation 12 and the determined fit-parameters a and b the density at 10% relative coincidence was determined and stated below the figure.

As for the laminar particle distribution, the counting limit was determined for a turbulent ($\rho(r) = 1 - r^2$) and laminar ($\rho(r) = 1 - r^2$) particle distribution as well. The results are shown in figure 15 and 16. The same function (equation 12) like in figure 14 was used to fit the data points and to compute the density at 10% relative coincidence or more precisely the counting limit. The simulation parameters to each figure are specified in the list of parameters in the appendix (section 8).

2 DETERMINATION OF COUNTING LIMIT

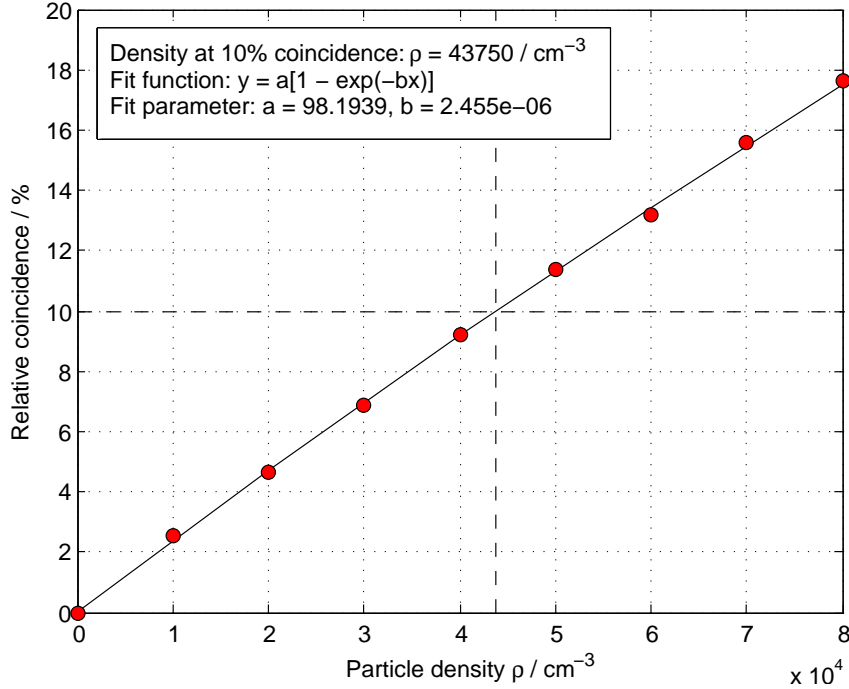


Figure 14: Relative coincidence as a function of particle density for $\rho(r) = 1$. Determined density at 10% relative coincidence (Counting limit): $\rho = 43750 \text{ cm}^{-3}$.

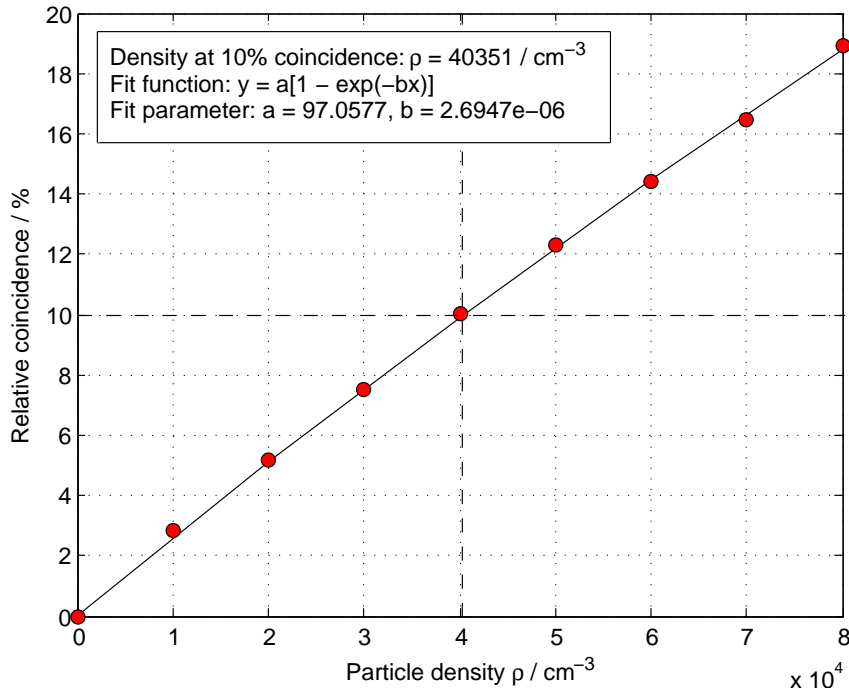


Figure 15: Relative coincidence as a function of particle density for $\rho(r) = 1 - r^6$. Determined density at 10% coincidence (Counting limit): $\rho = 40351 \text{ cm}^{-3}$.

2 DETERMINATION OF COUNTING LIMIT

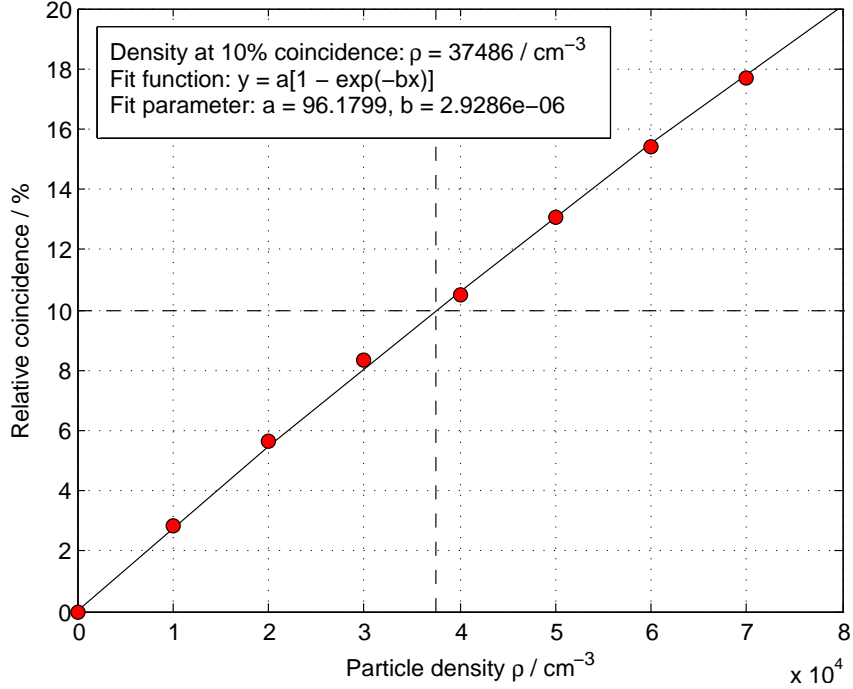
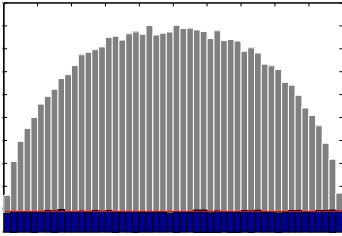
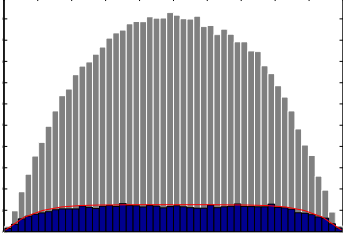
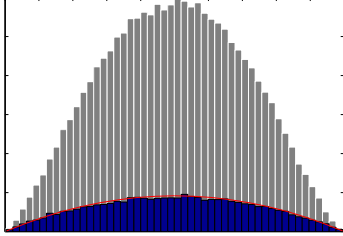


Figure 16: Relative coincidence as a function of particle density $\rho(r) = 1 - r^2$. Calculated density at 10% coincidence (Counting limit): $\rho = 37486 \text{ cm}^{-3}$.

For a good statistic and decrease of fitting errors the counting limit for each particle distribution was determined 10 times. Same parameters like in the simulations above were used. The computed counting limits are listed in table 1 and the averaged values and the standard deviations are stated. As the averaged counting limits in the table below indicate, the counting performance depends on the particle distribution. Uniformly distributed particles within the pipe adds up to higher measurable particle densities than for laminar distributed particles. The differences are in a range of $\sim 15\%$.

2 DETERMINATION OF COUNTING LIMIT

Table 1: Calculated counting limits for three different particle distributions to obtain standard deviation. The parameters are listed in the appendix.

| Densities at 10% relative coincidence / cm^{-3} | | |
|---|---|---|
| $\rho(r) = 1$ | $\rho(r) = 1 - r^6$ | $\rho(r) = 1 - r^2$ |
|  |  |  |
| 43910 | 40559 | 37197 |
| 43712 | 40584 | 37173 |
| 43637 | 40161 | 37246 |
| 43859 | 40001 | 37107 |
| 43495 | 39908 | 37319 |
| 43560 | 40370 | 37406 |
| 43791 | 39981 | 37127 |
| 43581 | 40355 | 37229 |
| 43753 | 39985 | 37134 |
| 43750 | 40061 | 37486 |
| 43705 ± 134 | 40197 ± 251 | 37243 ± 126 |

In the next section the theoretical counting limit for a setup including two orthogonal aligned linear detectors was determined and discussed.

2.3.2 Two linear detectors (2D)

A two-dimensional detector setup like depicted in figure 6 (right part) shows great potential achieving high measurable particle densities. In this section the counting limit of an orthogonal detector alignment is determined, by obeying the coincidence rules discussed in section 2.1.2. Therefore, the calculated relative coincidence values for certain particle densities were averaged for a sufficient high number of time steps T . These mean values are plotted in the

2 DETERMINATION OF COUNTING LIMIT

next figure. A cubic function (equation 13) was used to fit the data points:

$$y = ax^3 + bx^2 + cx + d \quad (13)$$

With the computed coefficients of equation 13 the density at 10% relative coincidence or rather the counting limit was determined and stated in the figure below.

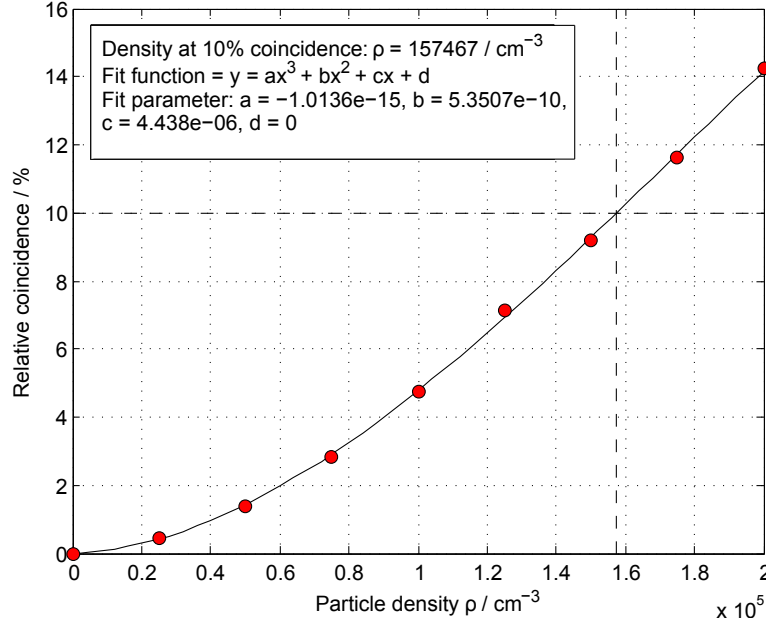


Figure 17: Relative coincidence as a function of particle density ρ for an orthogonal alignment of two linear detectors. Determined density at 10% coincidence (Counting limit): $\rho = 157467 \text{ cm}^{-3}$. Distribution of particles: $\rho(r) = 1$. The parameters are listed in the appendix (section 8).

The computed counting limit for an orthogonal alignment of two linear detector arrays ($\rho = 157467 \text{ cm}^{-3}$) is in much higher range than for a one-dimensional detector setup ($\rho = 43750 \text{ cm}^{-3}$). Thus, the counting limit is increased by a factor of ~ 3.6 or rather 360%.

The following graphs (figure 18 and figure 19) depict the same simulations for a turbulent and laminar particle distribution. Like the simulations in section 2.3.1 for a one-dimensional detector setup demonstrated, the density at 10% relative coincidence or rather the counting limit decreases for turbulent and laminar distributions. The computed counting limits for an two-dimensional detector alignment increase with a flattened particle distribution.

2 DETERMINATION OF COUNTING LIMIT

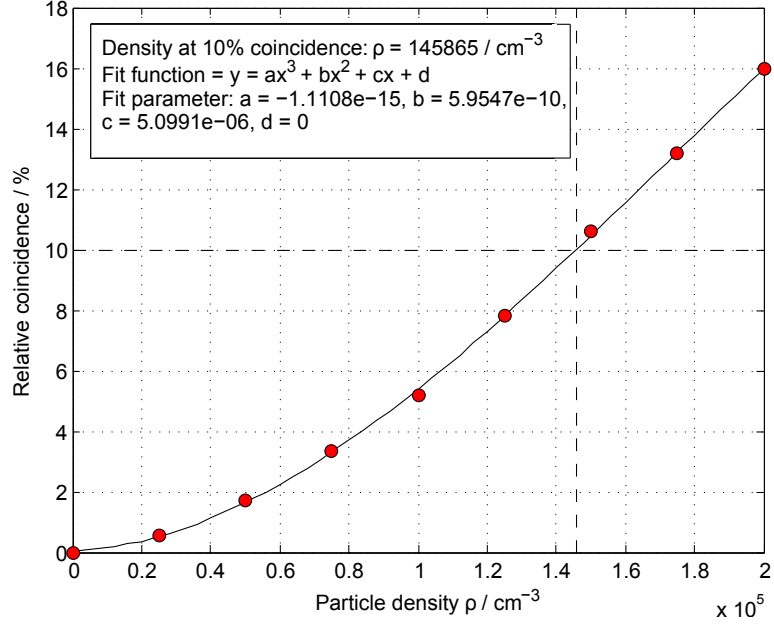


Figure 18: Relative coincidence as a function of particle density ρ for an orthogonal alignment of two linear detectors. Determined density at 10% cross-coincidence: $\rho = 145865 \text{ cm}^{-3}$; Distribution of particles: $\rho(r) = 1 - r^6$. List of all parameters: see appendix (section 8).

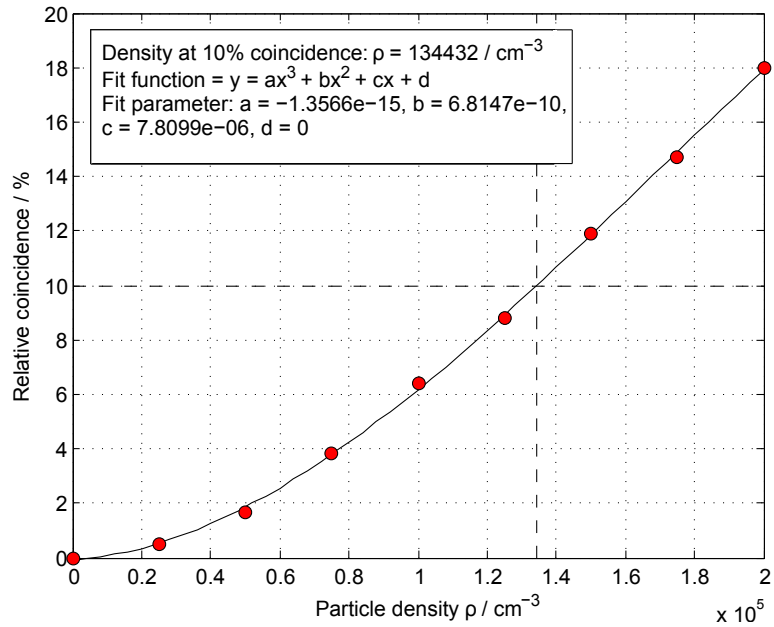
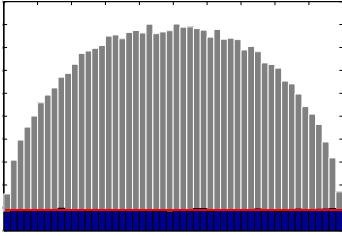
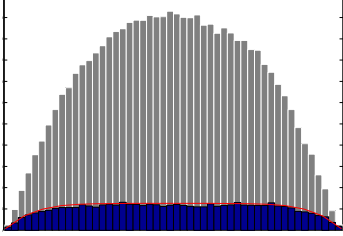
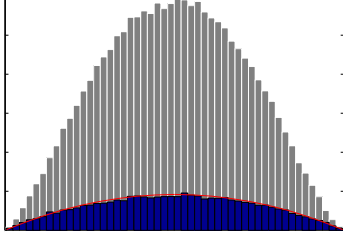


Figure 19: Relative coincidence as a function of particle density ρ for an orthogonal alignment of two linear detectors. Determined density at 10% cross-coincidence: $\rho = 134432 \text{ cm}^{-3}$; Distribution of particles: $\rho(r) = 1 - r^2$. List of all parameters: see appendix (section 8).

2 DETERMINATION OF COUNTING LIMIT

As stated for the uniform particle distribution the counting limit is increased by $\sim 360\%$ for the turbulent and laminar distribution as well, compared to a one-dimensional detector setup. To obtain a better statistic and the standard deviation of the counting limit, simulations were performed for every density distribution 10 times. For each computation a sufficient high number of times steps or rather measurements was performed. The averages values are listed in table 2.

Table 2: Calculated counting limits for three different particle distributions to obtain standard deviation. The parameters are listed in the appendix.

| Densities at 10% relative cross-coincidence / cm^{-3} | | |
|--|--|--|
| $\rho(r) = 1$ | $\rho(r) = 1 - r^6$ | $\rho(r) = 1 - r^2$ |
|  |  |  |
| 157074 | 145872 | 137600 |
| 158388 | 146268 | 135422 |
| 156875 | 147060 | 134665 |
| 156883 | 146527 | 134354 |
| 157679 | 145855 | 135781 |
| 157283 | 145952 | 135345 |
| 158490 | 144835 | 134726 |
| 157662 | 145905 | 136808 |
| 157015 | 145392 | 135213 |
| 157467 | 145865 | 134433 |
| 157482 ± 583 | 145953 ± 601 | 135435 ± 1055 |

The calculated counting limits for a two-dimensional detector setup show a huge gain in performance compared to a one-dimensional detector setup. So far all performed simulations are based on detectors with $N = 4000$ pixels. Since the counting limit is a function of pixel number, simulations were performed for detectors with several numbers of pixel. Like discussed in the simulations above the counting limit was computed with the cubic fit-function (equation 13). The simulations were performed for certain pixel numbers and plotted in the

2 DETERMINATION OF COUNTING LIMIT

next figure. The computed counting limits are fitted with equation 12:

$$y(x) = a(1 - e^{-bx})$$

The dashed line indicates the theoretical maximum counting limit of a two-dimensional detector setup. At this point the pipe is filled up with particles.

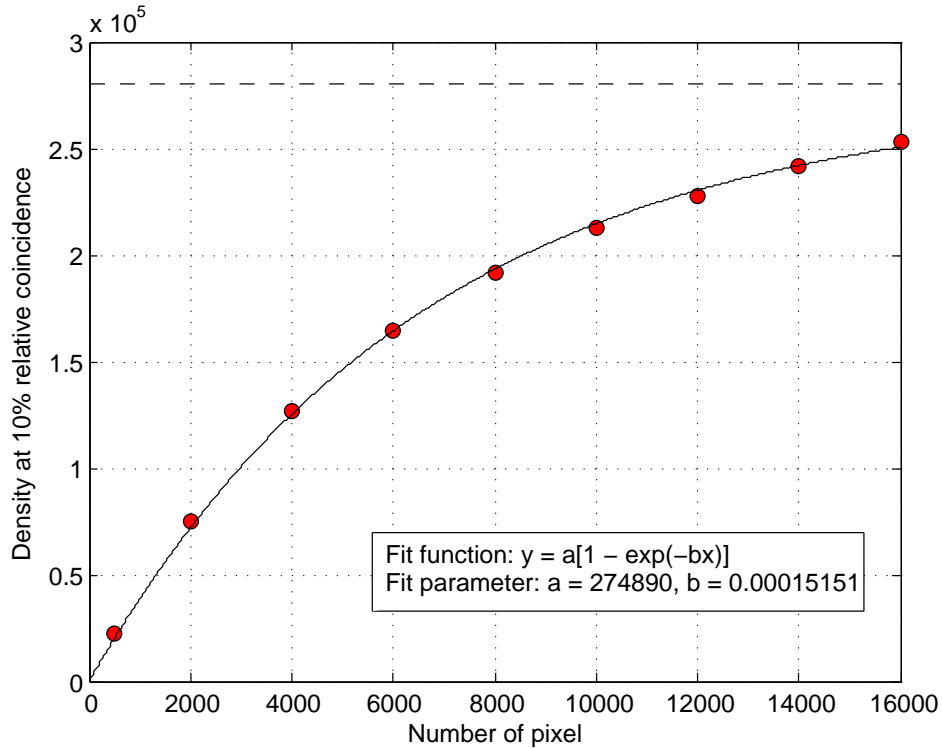


Figure 20: Densities at 10% relative coincidence as a function of pixel number for a two-dimensional detector setup. For higher number of pixels the counting limit increases. List of all parameters: see appendix (section 8).

As depicted in figure 20 with higher numbers of pixels the counting limit is increasable even more. Theoretically counting limits of $\rho = 250000$ particles/cm³ are achievable for a setup using two linear detectors in an orthogonal alignment with $N = 16000$ pixel elements.

2.3.3 Single photo diode (0D)

To conclude this section a simulation for a single, one-dimensional photo diode was performed. This is equivalent to the currently applied measurement principle. Thus, the diameter of the

2 DETERMINATION OF COUNTING LIMIT

gas exhaust was changed to $D_{\text{Pipe}} = 0.5 \text{ mm}$. Instead of a linear detector with a certain number of pixels a single photo diode or rather a one-pixel-detector was implemented in the simulations. The particles in the existing cell are counted by a simple comparator circuit. Therefore, the dead time of the system is defined by the width of the Gaussian peak at the comparator level (see figure 2). From the labor the dead time is known to be $t_{\text{dead}} = 200 \text{ ns}$. Thus, when a particle is counted by the detector, the system is not able to observe more particles within the next 200 ns. This process is independent of x - or y -coordinates of the particles. Hence the particle distribution does not affect the counting, or rather, the coincidence-probability in this zero dimensional setup. Like in the sections above the relative coincidence was determined for certain particle densities and a sufficient high number of time steps T . With fit-function 12 the counting limit at 10% relative coincidence or rather the counting limit was determined. The simulation run was performed 10 times and the averaged value computed to:

$$\underline{25325 \pm 905 \text{ cm}^{-3}}$$

This calculated value corresponds very well to the known value from the experiment: $\rho_{\text{exp}} \sim 20000 \text{ cm}^{-3}$. Actually, the stated counting limit in catalogs of common particle counters is $\rho = 10000 \text{ cm}^{-3}$. [6]

2.3.4 Comparison: Single photo diode (0D) and two linear detectors (2D)

A setup including two linear detectors in an orthogonal alignment promises a counting limit of at least $\rho = 135435 \text{ particles/cm}^3$. This is equal to a performance gain of >500% since the theoretical counting limit of the currently applied zero-dimensional setup is $\rho = 25325 \text{ particles/cm}^3$. By increasing the number of pixels up to 10000 pixel per line, performance gains beyond 900% are theoretically possibly (see figure 20). However, to compare these setups, simulations for the two-dimensional setup need to be performed including a line rate of the detector. The line rate is defined by the number of lines or rather pictures per second. In the previous simulations the line rate was assumed to be high enough to detect all particles, independent of their velocity. If the line rate is not in a sufficient high range the theoretical counting limit decreases. To get a first impression whether the theoretical counting rates can be reached or not, simulations for some randomly chosen line detectors were performed. Therefore, the line rates and pixel numbers were taken out of the data sheet to determine the counting limit for the three different particle distributions. By including line rates in the simulations the particle velocity distribution becomes important. It was assumed to be laminar ($v(r) = 1 - r^2$), since this distribution will cause the lowest counting limit (see section 2.1). All of the following considerations are done by applying a CMOS

2 DETERMINATION OF COUNTING LIMIT

chip, which senses charges continuously (see section 4.2). That means that the exposure time claims 100% of a single read-out process. No additional dead times, like they would appear in CCD chips, need to be considered. Thus, the limiting factor in the simulations is given by the line rate of the detector. The reciprocal value of the line rate is equal to the length of a single read-out process. Within a read-out process a detector element manages to count one single particle. If a second particle is imaged within this read-out process on the same pixel, a coincidence event appears. The table below lists the computed counting limits for some randomly chosen detectors.

Table 3: Computed counting limits for a two-dimensional setup considering line rates of randomly chosen detectors. List of simulation parameters: see appendix (section 8).

| Manufacturerer | Product | Number of pixels | Line rate / s^{-1} | Counting limit / cm^{-3} | | |
|----------------|---------------|---------------------|-------------------------|----------------------------|---------------|---------------|
| | | | | $y = 1$ | $y = 1 - r^6$ | $y = 1 - r^2$ |
| Hamamatsu | S104531024Q | 1x1024 | 9596 | 37319 | 34129 | 30713 |
| Hamamatsu | S11639 | 1x2048 | 4672 | 74727 | 69862 | 65257 |
| Awaiba | DR-2k-7-invar | 1x2048 | 80000 | 78498 | 72747 | 67595 |
| Awaiba | DR-4k-7 | 1x4096 | 80000 | 157649 | 145770 | 134783 |

As shown in table 3, with high enough line rates the theoretical counting limit can be reached. It is not guaranteed that these detectors fulfill all requirements, which may come up with optical implementation. Further considerations in terms of detector requirements are discussed in section 4.2 and 5.2.

2 DETERMINATION OF COUNTING LIMIT

2.4 Summary

Simulations to investigate the coincidence behavior of a particle stream within a pipe for different density distributions were performed. The detector was defined to be a 4000×1 pixel array with a pixel size equivalent to the size of the particles. The width of illuminated area was assumed to be $W = 10 \mu\text{m}$. All computations were performed for a sufficient high number of time steps T .

For former considerations the detector was assumed to be fast enough concerning read-out frequency. Thus the velocity distribution did not take affect on the counting limit. The simulations were performed with three different particle distributions:

- $\rho(r) = 1$... Uniform
- $\rho(r) = 1 - r^6$... Turbulent
- $\rho(r) = 1 - r^2$... Laminar

In table 4 the determined counting limits are stated for the three density distributions using one single detector array (1D).

Table 4: Counting limits for an one-dimensional setup using a single line detector.

| Distribution | ρ_N/cm^{-3} |
|---------------------|-------------------------|
| $\rho(r) = 1$ | 43705 ± 134 |
| $\rho(r) = 1 - r^6$ | 40197 ± 251 |
| $\rho(r) = 1 - r^2$ | 37243 ± 126 |

A laminar particle distribution ($\rho(r) = 1 - r^2$) indicates the lowest counting limit since a high number of particles are localized in the middle of the pipe. Instead a system with uniform distributed particles ($\rho(r) = 1$) shows a better measurement efficiency. Therefore, a mechanism which force the particles to move uniformly distributed within pipe would increase the maximum counting rate up to approximately 15%.

The following table lists the counting limits for a setup using two linear detectors in an orthogonal alignment.

2 DETERMINATION OF COUNTING LIMIT

Table 5: Counting limits for a two-dimensional setup using two line detectors in an orthogonal alignment.

| Distribution | ρ_N/cm^{-3} |
|---------------------|-------------------------|
| $\rho(r) = 1$ | 157482 ± 583 |
| $\rho(r) = 1 - r^6$ | 145953 ± 601 |
| $\rho(r) = 1 - r^2$ | 135435 ± 1055 |

As stated in table 4 and 5 the counting limit is increased by a factor of ~ 3.6 when applying a second linear detector in an orthogonal way.

To compare these results with the currently applied zero-dimensional setup, the counting limit of the zero-dimensional setup was computed by implementing a single photo diode in the simulations to:

$$\rho = (25650 \pm 628) \text{ cm}^{-3}$$

This corresponds to the determined value from the experiment, which is known to be $\rho_{\text{exp}} = 20000 \text{ cm}^{-3}$. Thus, using two linear detectors would increase the counting performance of the condensation particle counter up to more than 500%. For higher pixel numbers even higher counting limits are possible (see figure 20).

Furthermore, it was shown that these results can be achieved if line rates of randomly chosen detectors are included.

3 Optical considerations

3.1 Fundamentals

Most visual-based devices in particle measurements use scattered light to gain information about particle mass or number. These systems are based on the different scattering theories. For example by using a laser in the optical range, such as a helium-neon source with a wavelength of $\lambda = 632.8 \text{ nm}$, three different types of scattering processes as a function of particle size are described:

$$\begin{aligned} \text{Rayleigh:} & \quad 0.1 \mu\text{m} > D_{\text{particle}} \\ \text{Mie theory:} & \quad 0.1 \mu\text{m} \leq D_{\text{particle}} \leq 5 \mu\text{m} \\ \text{Classic scattering:} & \quad 5 \mu\text{m} < D_{\text{particle}} \end{aligned}$$

The diameter of particles which are generated in the condenser block of condensation particle counter is $D_{\text{Particle}} = 5 \mu\text{m}$. Consequently, in general, Mie theory does not describe the process sufficiently enough. Classic scattering is the dominant process. Thus, the focus of this thesis does not lie on the development of a new counting principle based on scatter theories of small particles. Its aim is to discuss the possibilities of using an imaging system which make use of the classical scatter processes, like reflection and refraction.

In general the imaging process is realizable applying two different techniques:

1. Bright field (BF)

This is a basic method for imaging. The sample is illuminated from below and absorbs or scatters a fraction of the transmitted light. The detector or the observer is placed above and is directed directly into the light source. The contrast of the picture is given by the amount of scattered and absorbed light [17].

2. Dark field (DF)

This method uses scattered light to image the probe. It does not make use of the transmitted or absorbed light. Consequently, if there is no sample in the system, the observer or the detector can only see a black picture. [18]

Both ways bring advantages and disadvantages with them. To elaborate different ideas regarding the imaging setup, an optical simulation tool called *Zemax* was used. A short description of this program, developed by *Radiant*, is given in the following section.

3 OPTICAL CONSIDERATIONS

3.2 Radiant Zemax

Zemax is a program which can model, analyze, and assist in the design of optical systems. The interface to **Zemax** has been designed to be easy to use, and with a little practice it can allow very rapid interactive design. Most **Zemax** features are accessed by selecting options from either dialog boxes or pull-down menus. Keyboard shortcuts are provided for quickly navigating or bypassing the menu structure. [19]

In **Zemax** you can basically work in two different modes:

1. Sequential mode

Sequential ray tracing is one of the core technologies in Zemax. Sequential ray tracing is used to model almost all imaging systems, including a focal systems. It is fast, flexible, and easy to optimize and tolerance. The sequential approach is that light travels from surface to surface in a defined order. This allows a great simplification in ray tracing, as we always know which surface a ray will hit next. OpticStudio supports both sequential and full non-sequential ray-tracing to give you complete capabilities for any system. [20]

2. Non-Sequential mode

It is a powerful and general technology for tracing rays in systems where there are multiple optical paths. Typical uses include:

- *Illumination systems, especially those with multiple or complex optical sources*
- *Systems like interferometers, in which light that has traveled through several different optical systems must be coherently recombined*
- *Stray light analysis in otherwise sequential optical systems*

The non-sequential model is that there is no pre-defined path for any ray. A ray is launched and hits whatever object is in its path, and it may then reflect, refract, diffract, scatter, split into child rays etc. It is a far more general technology than sequential ray-tracing. Also, you work with parametric 3D solids instead of sequential surfaces, and this makes the system setup somewhat easier with full 3D placement of all system objects. [21]

3 OPTICAL CONSIDERATIONS

3.3 Characteristics of a single decane particle

To get a first impression of that the intensity distribution of an illuminated particle looks like, a simple simulation with *Zemax* by using the non-sequential mode was performed. Thus, only geometrical optics, like refraction and reflection is considered! Diffraction effects are not part of this section.

In the simulation a particle with a diameter of $5\ \mu\text{m}$ got illuminated by a light source. The cross-section area of the source was assumed to be in the size range of the particle. The refraction index of the particle was specified as $n = 1.411$, which corresponds to the refraction index of decane [14]. Since the imaginary part of n is zero at the desired wavelength, the decane particle is non-absorbing. A beam stop was placed behind the particle to absorb the main beam. This alignment was surrounded by a spherical detector. Thus, scattered light in all room direction was imaged. The schematic setup is depicted in figure 21.

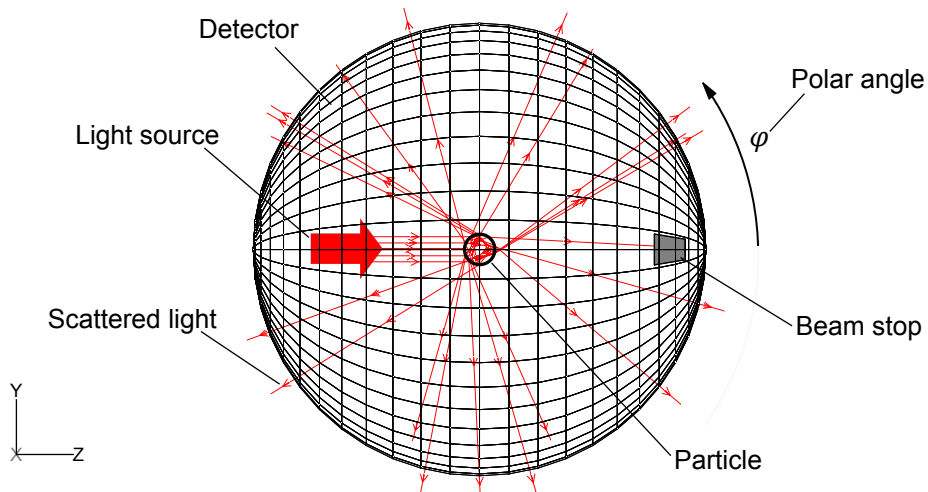


Figure 21: Schematic Simulation setup for obtaining the scattering distribution of a single decane particle. The particle is illuminated from the left side with a collimated laser beam. Thus the light gets scattered and imaged on the spherical detector. A beam dump stops the main beam before it hits the detector.

With a setup like in figure 21 a simulation run was performed for 4×10^9 analysis rays. This is the maximum number of rays *Zemax* is able to compute. Following figure depicts the computed intensity in the y - z -plane as a function of polar angle φ . All further input parameters are listed in the appendix.

3 OPTICAL CONSIDERATIONS

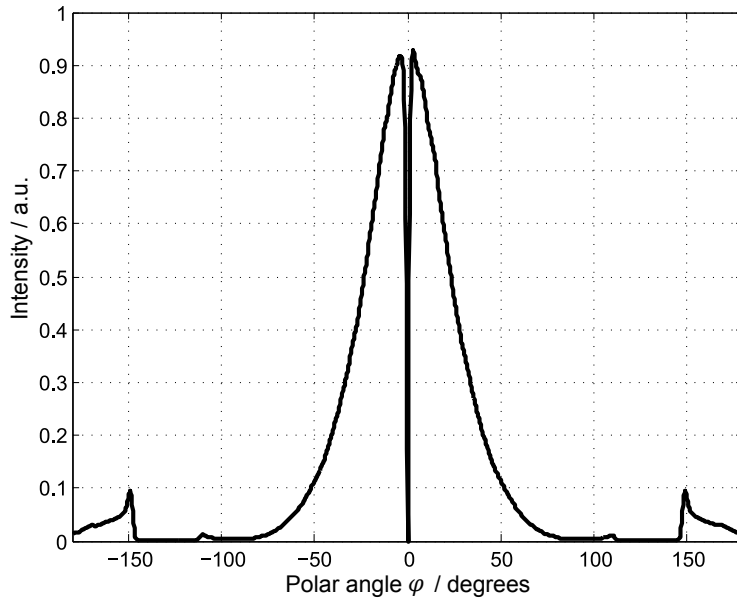


Figure 22: Scattering intensity as a function of polar angle in the y - z -plane. A huge peak in forward direction, or rather at low polar angles is observable. The drop at polar angle $\varphi = 0^\circ$ indicates the beam dump. The two peaks at $\sim 150^\circ$ are caused by inner reflections, which would cause the rainbow effect for different wavelengths. List of parameters: see appendix (section 8).

Figure 22 shows a high dependency of scattered light on the direction of illumination. To ensure highest signal gain a detector should be aligned in forward direction (see figure 23, right part).

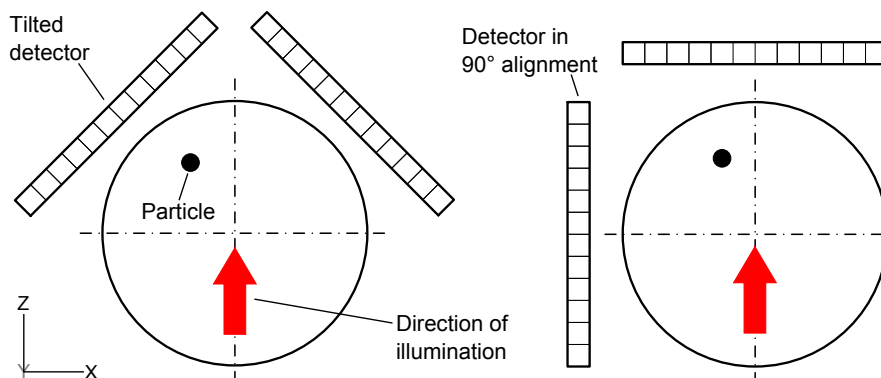


Figure 23: General ways of aligning detectors as a function of the illumination direction. The light beam is indicated by the red arrow.

3 OPTICAL CONSIDERATIONS

To realize a 2-dimensional setup as it is shown in figure 23 (right part), a second detector has to be alignment in 90°-direction. This detector gains signal perpendicular to the illumination direction. Like it is depicted in figure 21 the light yield in this direction is very low. Instead two detector arrays tilted in the x - z -plane (see figure 23, left part) will result in an equally distributed signal gain on both detectors. Additionally to the scattering distribution the distance r between particle and detector influences the signal output. For imaging setups (which are discussed later) this factor is given by the numerical aperture. But in general the total signal output on the detector is a function of polar angle φ and the radial distance r . The polar angle dependence is given in figure 23, whereas the radial intensity part drops with $\frac{1}{r^2}$. Basically the total amount of scattered light is a function of laser power, refraction index of the particle and its diameter. In common condensation particle counters the diameter of particles is adjustable with the condenser length (see section 1). Thus a simulation with *Zemax* was set up to determine the total amount of scattered light (integrated over all room angles) as function of particle diameter. Therefore the total power on a spherical detector (setup similar as in figure 21) was computed for certain particle diameters (see figure 24).

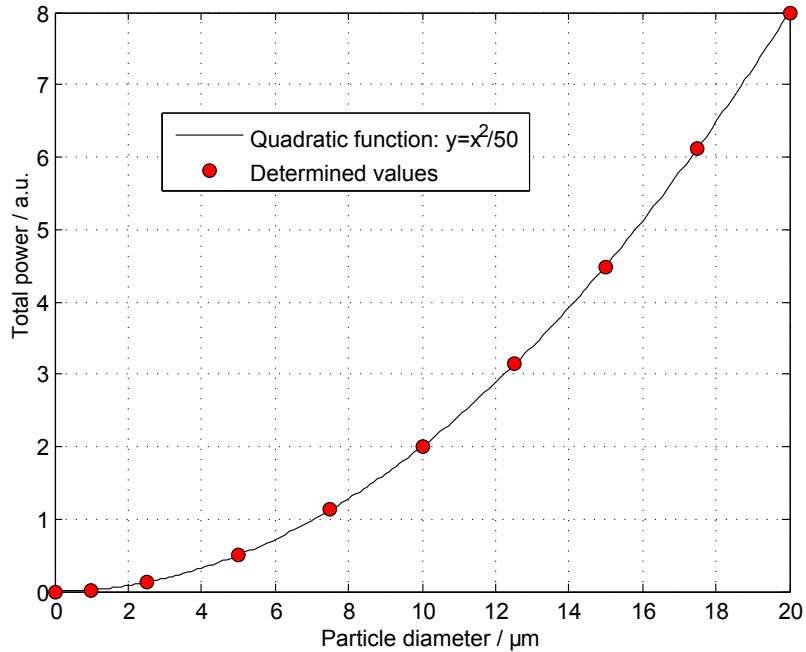


Figure 24: Total power of scattered light as a function of particle diameter. Since the cross-section area of particles increases quadratically with the radius, the amount of scattered light does as well. List of parameters: see appendix (section 8).

Since the cross-section area of the particles is a function of r^2 , the total power increases

3 OPTICAL CONSIDERATIONS

quadratically with particle size. The cross-section area defines the area which is illuminated by the light source. Thus the data points are fitted with a quadratic function. Like depicted in figure 24 the total amount of scattered light can be increased significantly by generating bigger particles in condenser block in condensation particle counter.

These results were used to to set up appropriate imaging setups, discussed in following sections.

3.4 Optical design

To realize a spatial resolving imaging system an optical setup is required. Without an appropriate optic, scattered light will illuminate a wide area of the detector. There will be slight differences in intensity along the detector length depending on the particle's position, but in practice it will hardly be possible to distinguish between two particles over the whole detector area. The following figure shows the detector image of a simulation in the non-sequential mode with two particles within the illuminated area. The detector, a 4096×1 pixel array with a pixel size of $5 \mu\text{m} \times 2000 \mu\text{m}$ was placed above the illuminated area right after the pipe in forward direction (Analog to the dark field setup in figure 27). The height of 2 mm was chosen to get a better statistic; the changes of information are, therefore, marginal.



Figure 25: Dark field image of a 4096×1 pixel array detector with two particles within measuring volume. Each stripe indicates a single pixel element. Due to the fact, that no optic was used to focus the scattered light, a counting analysis is almost impossible. Therefore an imaging optic is necessary. List of parameters: see appendix (section 8).

As shown in figure 25 it is hard to read out a number of particles within the measuring volume. Especially if two particles pass the illuminated area at closer distances. Thus, it is essential to use an optic in order to capture scattered light in a dark field imaging system. A basic way to image an object on a detector can be realized by using a simple lens, as shown in figure 26. This works pretty well for points lying on the focal plane, normal to the optical axis. For objects with different positions along the z-axis, the focus changes along the z-axis. This results in a disc on the detector, which grows with the distance of the particles to the focal plane.

3 OPTICAL CONSIDERATIONS

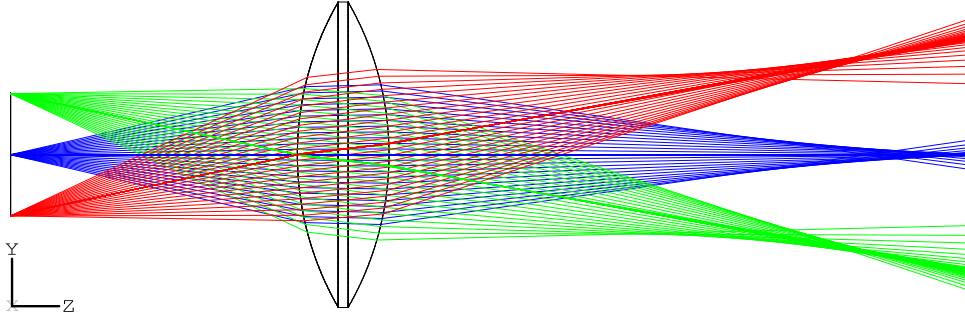


Figure 26: Schema of imaging using a single biconvex lens. In a basic setup like this, it is only possible to focus points which are lying on the focal plane ($z = 0$). All the other points are out of focus. The rays are not focused perfectly on the detector due to spherical aberrations of the lens.

To minimize the spherical aberrations and keep the focal length short, two aspherical lenses could be used here instead of a single biconvex lens. By applying a second movable lens along the optical axis (in z -direction) focusing is possible. But as far as the complexity an auto-focus implicates in a particle counting system is concerned, a dynamic solution will not be discussed in this thesis. The aim should rather be to find a cost-efficient optic in a basic way, where moveable parts are not necessary. In the next sections optical setups in the bright- and in dark-field mode are discussed. Their effects on detector and light source requirements are elaborated on. Therefore, the feasibility of lens setups and other methods obtaining optical resolution, like applying fiber bundles, are evaluated and summarized at the end of each section.

4 Dark field

In this next section simulations for different optical setups exclusively in the dark field mode are presented and discussed.

4.1 Imaging setups

Basically, in a dark field setup a flat laser beam, like it is shown in figure 27, illuminates the passing particles. A detector located aside the beam is used for imaging. In a bright field setup, on the other hand, the detector is located directly in the beam.

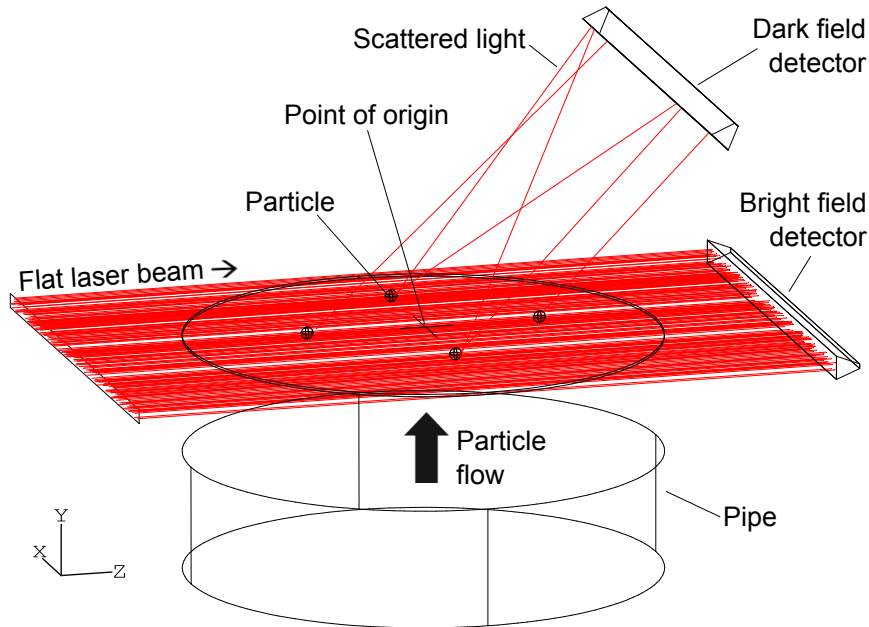


Figure 27: General differences between a bright field and a dark field setup. In the bright field setup the detector is located directly in the beam, while it is positioned aside in a dark field setup.

For all following simulations the power of the illuminating light source was defined to be $P = 0.1 \text{ W}$. The source emits parallel rays within a rectangular area with dimensions of $20 \text{ mm} \times 0.01 \text{ mm}$. The particles were always positioned in a way, that the whole volume was illuminated. The point of origin is positioned on the symmetric axis of the pipe on the level of the flat laser beam. The total power values are stated for a single particle.

4 DARK FIELD

4.1.1 Simple imaging using two aspherical lenses

Figure 28 shows the arrangement of the two aspherical lenses for imaging scattered light on a line detector with 4000 pixels. It is positioned at the back focal length of the lens setup. The pixel size was assumed to be $5\ \mu\text{m}$ (H) \times $2000\ \mu\text{m}$ (V). Usually, the vertical size (V) of common detectors is in a range of $5\ \mu\text{m}$ to $200\ \mu\text{m}$. Since a linear detector array is used, a large vertical pixel size does not change the picture information significantly. In terms of total power, the signal is less dependent on vertical displacements or changes in focus. Aspherical lenses are used to minimize spherical aberrations. A rectangular light source with 20 mm broadness and $10\ \mu\text{m}$ height illuminates the passing particles. An absorbing volume (beam stop) in front of the lenses stops the main beam.

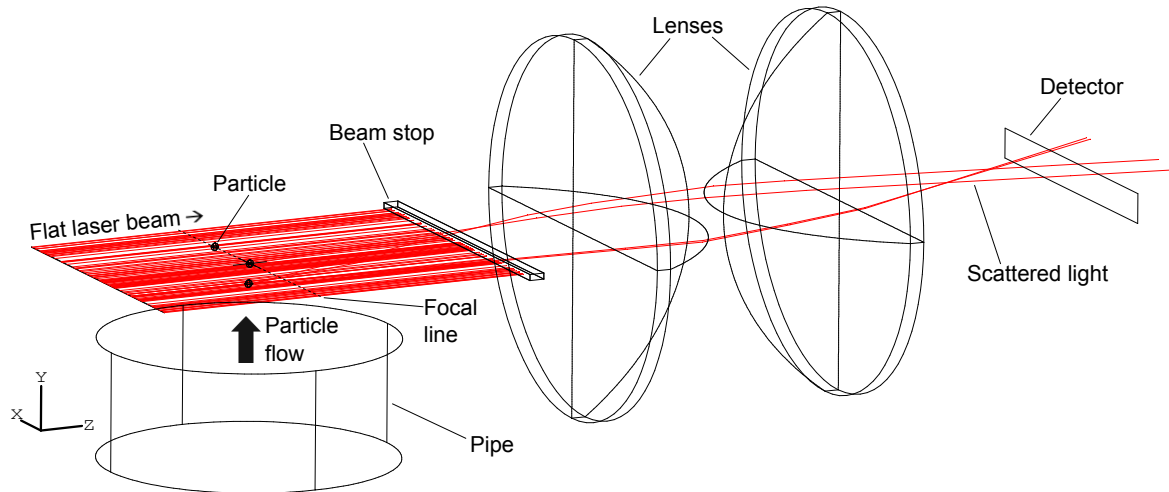


Figure 28: Dark field setup using two aspherical lenses. Two particles are positioned within the flat laser beam on the focal line of the lens setup, the third one in an off-axis z -position. The scattered light in forward direction is focused on a linear detector.

A simulation run was performed for three particles positioned within the illuminated area. Like depicted in figure 28 two of them are sited on the focal line in the x - y -plane. The distance between focal line and lenses accords to the focal length of the setup. Thus the focal line is imaged clearly on the detector. A third particle is shifted 2.5 mm in the negative z -direction. Thus it is not positioned on the focal line. Figure 29 shows the computed detector intensity as a function of pixel position. Only scattered light is imaged on the detector since the main beam is absorbed by the beam stop. A list of all simulation parameters is stated in the appendix.

4 DARK FIELD

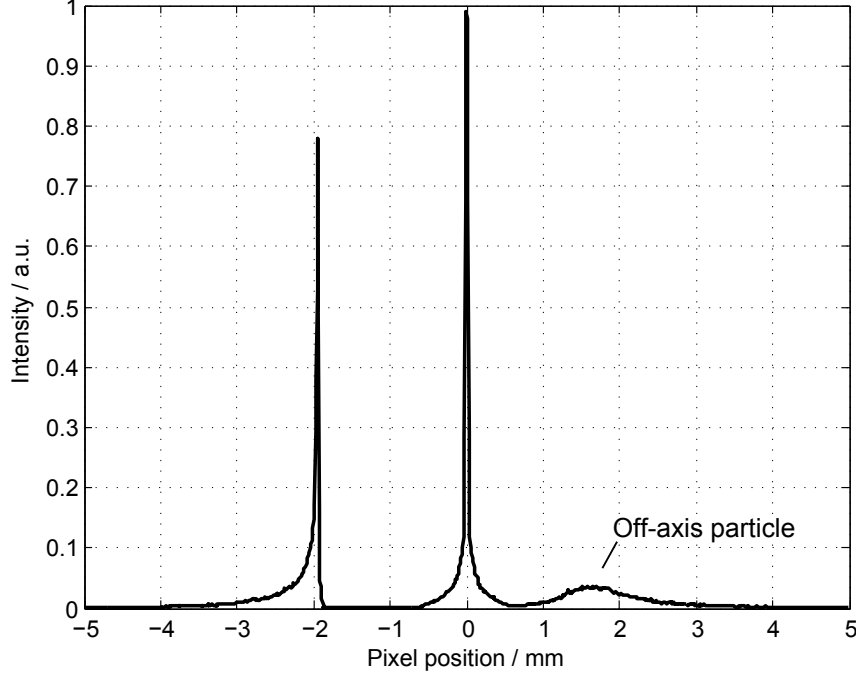


Figure 29: Scattered light of three particles imaged on a linear detector array with 4000 pixels. The two peaks indicate the particles which are positioned on the focal line. The third, off-axis particle is blurred out on the detector. Total detected power generated by a single particle: $P_{\text{total}} = 6.0050 \times 10^{-6} \text{ W}$. List of parameters: see appendix (section 8).

The two particles positioned on the focal plane are imaged clearly on the detector. But the third, off-axis particle is not imaged on the detector in a proper way. There is just a blurred signal visible which can hardly be identified as a signal particle.

The simulations in section 2 showed that a second linear detector orthogonally aligned is necessary to obtain the highest performance in terms of counting limit. Thus the detector signal applying the same imaging setup but in a 90° alignment was determined (see figure 23) using the same parameters. Since the optic did not change, the determined intensity distribution of the detector looks similar to the graph in figure 29. But the total power of a single particle on the detector was determined to:

$$P_{90^\circ} = 6.9133 \times 10^{-8} \text{ W}$$

Compared to the setup in forward direction, with an obtained power on the detector of $P_{0^\circ} = 6.0050 \times 10^{-6} \text{ W}$ the signal in 90° -direction drops by a factor of $F \sim 100$. This result was expected since the intensity in 90° -direction drops significantly (see figure 22). This low signal strength leads to high demands on the detector, which are discussed in section 4.2.

4 DARK FIELD

In terms of optic, neither a forward directed nor a 90° alignment, would result in a consistent counting process. Due to the blurred signal an off-axis particle would generate, the electronic analysis will be very challenging and the number of coincidence events will increase as well. Thus, an objective is needed to focus particles with different z positions. In a dynamic system like in the condensation particle counter a objective with moveable parts would result in high complexity and therefore in decreasing coincidence limits. The attention should lie here on simple, economically priced solutions. By applying a slit nozzle particles will pass the flat beam within the focal plane. Thus a setup like this would lead to a performance gain of to 150% (see section 2). Since a slit nozzle eliminates the possibility of imaging additionally in an orthogonal direction no more investigations are done. The following sections discuss other approaches for imaging off-axis particles.

4.1.2 Telecentric lens setup

A way to avoid the focusing problematic would be to use a telecentric lens. In a setup like it is shown in figure 30, only parallel or small-angle scattered light is imaged on the detector.

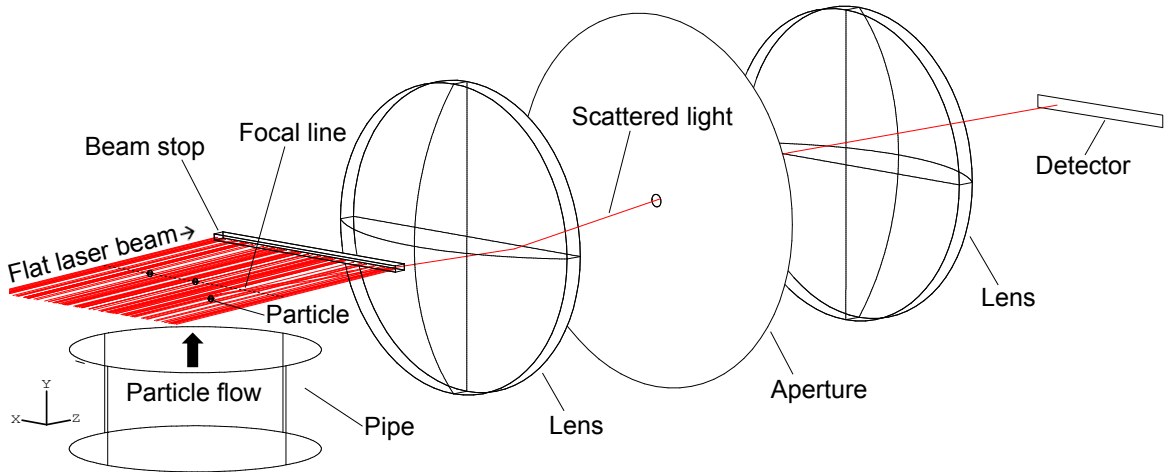


Figure 30: Schematic of a telecentric lens setup using two plan-convex lenses and an aperture between them. The slightly tilted light source ($\varphi = 2.5^\circ$, rotated about the x -axis) illuminates a small band above the pipe. Scattered light in z -direction is imaged on the detector. The main beam is absorbed by the beam stop.

The diameter of aperture D_A defines the amount of imaged light. For small diameters just little signal is imaged on the detector, but a greater depth of focus can be reached. Thus, an additional objective is not necessary. With this setup particles are imaged clearly on the detector, independent of their positions within the pipe (see figure 31).

4 DARK FIELD

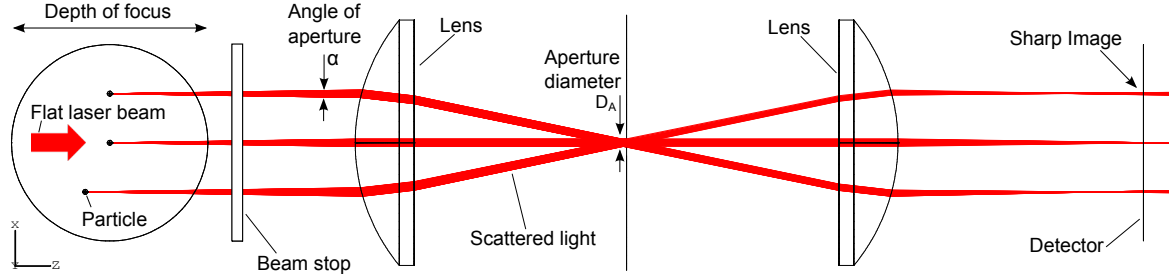


Figure 31: Aperture stop: The aperture diameter D_A defines the angle of aperture α . With lower angles the depth of focus is extended. Thus particles with various z positions are imaged clearly on the detector. In this figure just scattered light is plotted.

For this simulations the same detector like in the section above was positioned in focus distance to the second lens. Figure 32 depicts the intensity plotted as a function of position for three particles. Two particles were positioned along the focal line and a third one in an off-axis z -position. 4×10^9 analysis rays were computed.

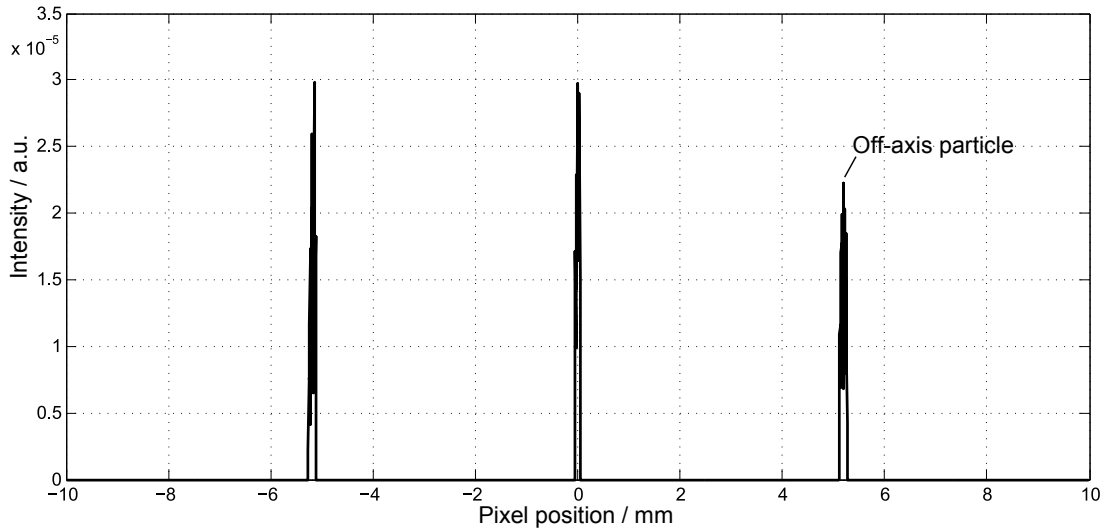


Figure 32: Detector signal as a function pixel of position. Since the angle of aperture is small, a great depth of focus is realized. All three particles are imaged clearly on the detector. The total power on the detector was determined to be $P = 1.1607 \times 10^{-8}$ W for a single particle. List of parameters: see appendix (section 8).

All particles are imaged sharp on the detector. Hence an additional objective is not necessary. The total power generated by a single particle is in low range since an aperture stop is applied. Thus, the requirements in terms of detector sensitivity are demanding (see section 4.2).

4 DARK FIELD

4.1.3 Orthogonal alignment

A different way of imaging particles on the detector in a proper way can be realized by putting the laser beam and optical axis in an orthogonal alignment. A tilted laser and tilted optical axis in a way like shown in figure 33, would result in sharp image of particles. Independent of their position within the illuminated area, all particles are located on the focal plane. Applying a two-dimensional detector array, like depicted in the next figure is reasonable here. Thus, additional optics and detectors are not necessary in order to obtain the maximum counting limit. A setup with only one linear (one-dimensional) detector and an additional cylindrical lens in front of the detector is realizable as well. But the focus in this section lies on the applicability of one single two-dimensional detector array, to gain maximum performance in terms of counting limit.

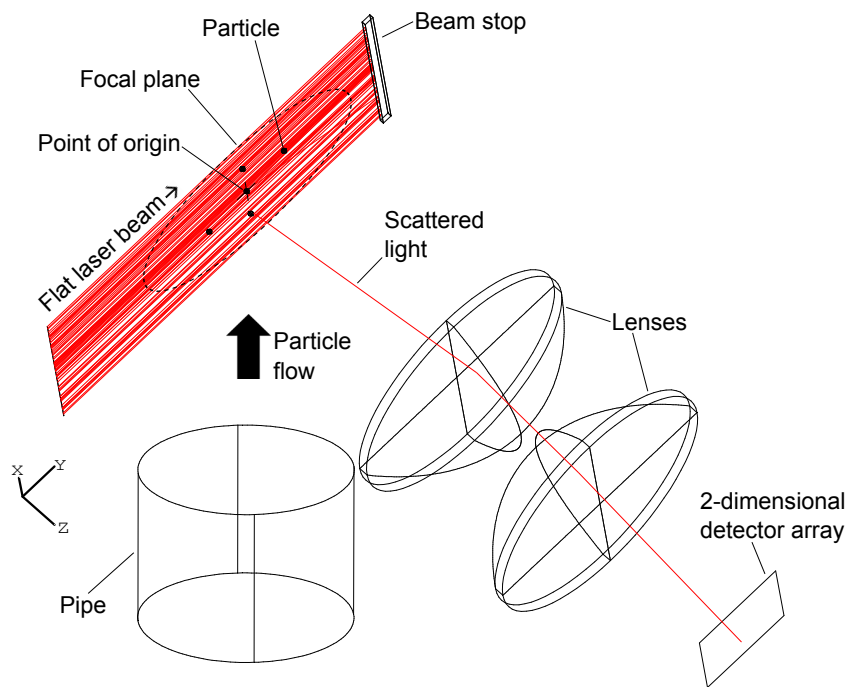


Figure 33: Orthogonal alignment including two plan-convex lenses and a flat laser beam which proceeds perpendicular with respect to the detector lot. All particles which pass the flat laser beam are positioned in the focal plane of the lens setup. The scattered light is imaged on a two-dimensional detector array.

A setup like depicted in figure 33 enables a sharp imaging of all particles, independent of their position within the pipe or rather within the illuminated area. Thus a simulation was performed for 5 particles positioned within the the flat laser beam (coordinates see figure 34). Particles positioned along the y -axis were shifted 0.1 mm in x -direction. This ensures

4 DARK FIELD

a homogenous illumination of all particles. Otherwise particles would be positioned in the shadow of the first one. The number of pixels for the two-dimensional detector array was assumed to be 1000×1000 . Following figure shows the intensity distribution as function of pixel position of the two-dimensional detector array.

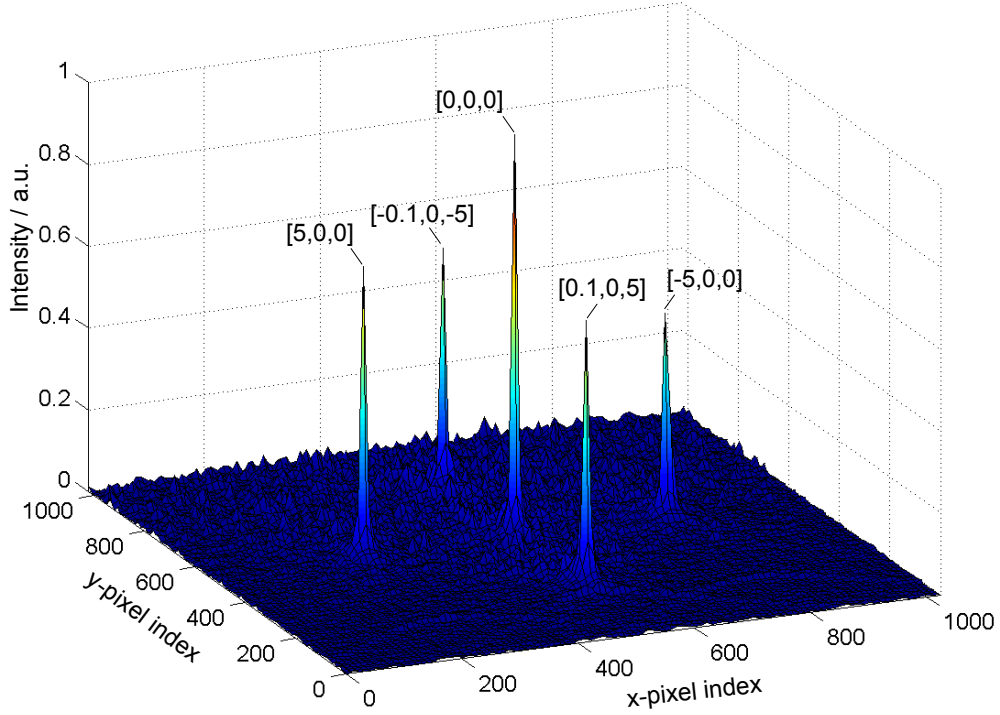


Figure 34: Signal distribution of five imaged particles on a two-dimensional detector array. Five sharp peaks are clearly visible. Each particle, independent of position is imaged in a proper way on the detector. The coordinates $[x,y,z]$ (in mm) correspond to the positions of the five imaged particles. Computed signal of a single particle: $P_{\text{Total}} = 6.75 \times 10^{-8}$ W. List of parameters: see appendix (section 8).

As depicted in figure 34 all particles are imaged properly on the detector, independent of their positions. The peak of the centered particle is stronger, since the effective angle of aperture is the largest for this particle. With bigger lenses the differences in intensity would be minimized. Like it is illustrated in figure 33 a compact alignment of the components limits the numerical aperture of the setup. The lenses could not be chosen as big as required since they would collide with the pipe. Due to the fact that just scattered light in $\varphi = 90^\circ$ direction is imaged on the detector the total amount of generated signal is in a very low range (see "scattering distribution of a single particle" in section 3.3). The total power generated by a

4 DARK FIELD

single particle in orthogonal alignment was computed to:

$$P_{\text{Total}} = 6.75 \times 10^{-8} \text{ W}$$

Thus P_{Total} is in the same low range as the total power of a single particle in the telecentric setup. To realize a gain in signal scattered light from low angle regions should be used for imaging instead.

4.1.4 Scheimpflug alignment

A way to image scattered light from low angle regions can be realized by obeying a special geometric rule called "Scheimpflug principle". This geometric principle describes the orientation of the focus plane of an optical setup when the image plane is not aligned parallel to the lens plane. The condition of maximum sharpness for arbitrary focal plane alignments is, that the focus-, lens- and image-plane have to intersect in one point. [26]

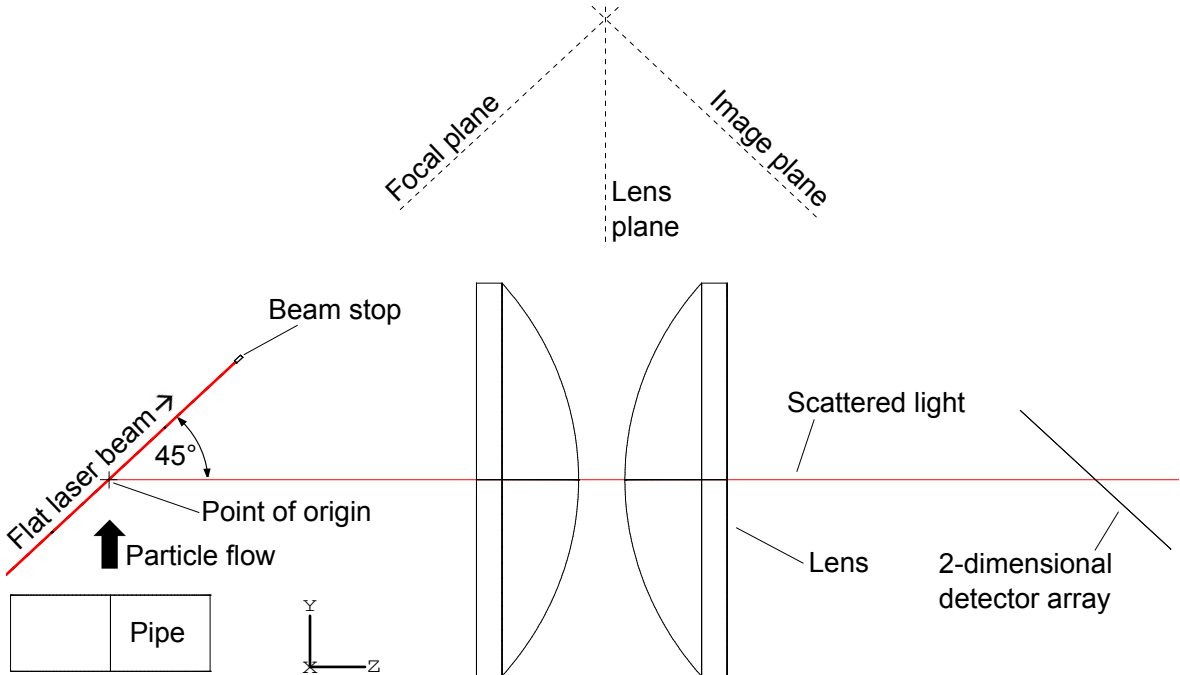


Figure 35: By obeying the "Scheimpflug rules" the imaging angle in the orthogonal alignment is reduced to $\varphi = 45^\circ$. The numerical aperture of the system is arbitrary since the lenses cannot clash with the pipe. Focal-, lens- and image-plane intersect in one point.

Figure 35 depicts the implementation of the Scheimpflug principle for the orthogonal alignment-setup introduced in the section above. By adjusting this alignment in line with the

4 DARK FIELD

Scheimpflug principle the focal plane can be chosen arbitrarily. Thus, a gain in signal should be observable since the imaging angle φ is reduced from $\varphi = 90^\circ$ to $\varphi = 45^\circ$ (see "scattering distribution of a single particle" in section 3.3, figure 22). A simulation run with 4×10^9 analysis rays was performed for five particles within the flat laser beam. Next figure shows the computed intensity profile of the two-dimensional detector array. A list of parameters is stated in the appendix.

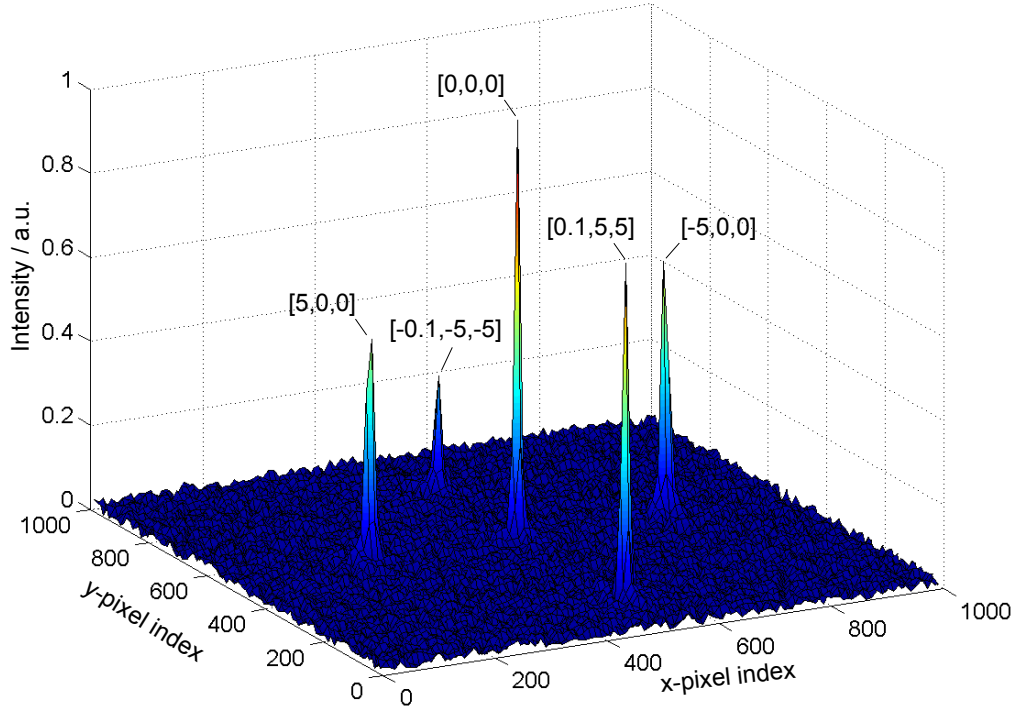


Figure 36: Detector signal as a function of pixel index. The coordinates $[x,y,z]$ (in mm) correspond to the positions of the five imaged particles. A higher peak for particles with positive z -positions is observable, since the numerical aperture increases. The generated signal of a single particle was determined to $P_{\text{Total}} = 1.59 \times 10^{-6}$ W. List of parameters: see appendix (section 8).

By applying the Scheimpflug principle particles are imaged clearly on the detector. The total power generated by a single particle was computed to:

$$P_{\text{Total}} = 1.59 \times 10^{-6} \text{ W}$$

Compared to the orthogonal setup (discussed in section 4.1.3) the total power is increased by a factor of ~ 25 .

4 DARK FIELD

4.1.5 Fiber bundles

In this section the implementation of fiber bundles is discussed. Fiber bundles are arrays of single glass fiber cables with a certain numerical aperture. By using bundles with low numerical apertures only light from certain regions is coupled into the fiber. Thus fiber bundles can be used to gain spatial resolution. To realize fiber arrays in *Zemax*, a surface in front of the detector was specified to transmit rays only within a certain angle. This angle is defined by the numerical aperture of the fibers. For the simulations the aperture angle was assumed to be $\alpha = 11.5^\circ$, which is equal to a numerical aperture of $NA = 0.2$ in air since:

$$NA = \sin(\alpha) \quad (14)$$

Figure 37 shows a fiber bundle setup in *Zemax*. Three particles are positioned within the flat laser beam and depicted disproportionately big for better illustration. The fiber bundle layer is positioned in front of the detector. The detector was assumed to be a 4000×1 pixel array. To achieve the full resolution of the detector the number of fibers must be at least 4000 as well. Otherwise the number of fibers determines the spatial resolution. In the simulations the number of fibers was assumed to be sufficient high anyway, since a layer was used. In this case only the aperture angle defines the spatial resolution.

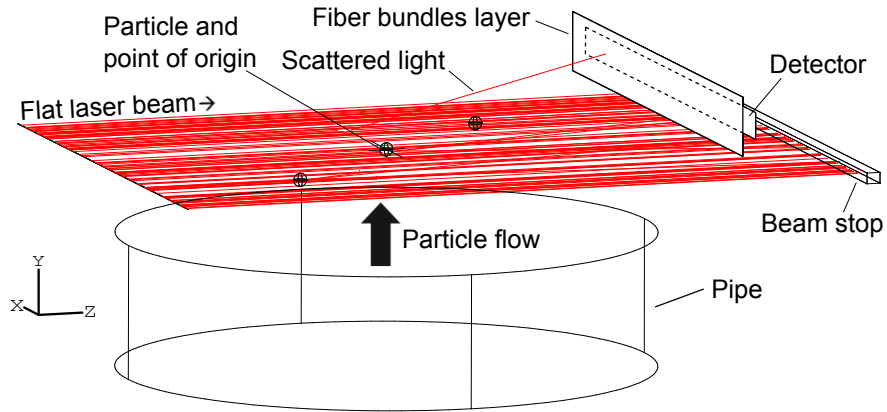


Figure 37: Fiber bundle setup: The numerical aperture of the fibers is realized by a layer, which allows only rays within a certain angle to pass. Three particles with different x - and z -coordinates are positioned within the flat laser beam.

A simulation with 4×10^9 analysis rays was performed. The computed intensity as a function of pixel position is plotted in figure 38. The parameters of simulation are listed in the appendix.

4 DARK FIELD

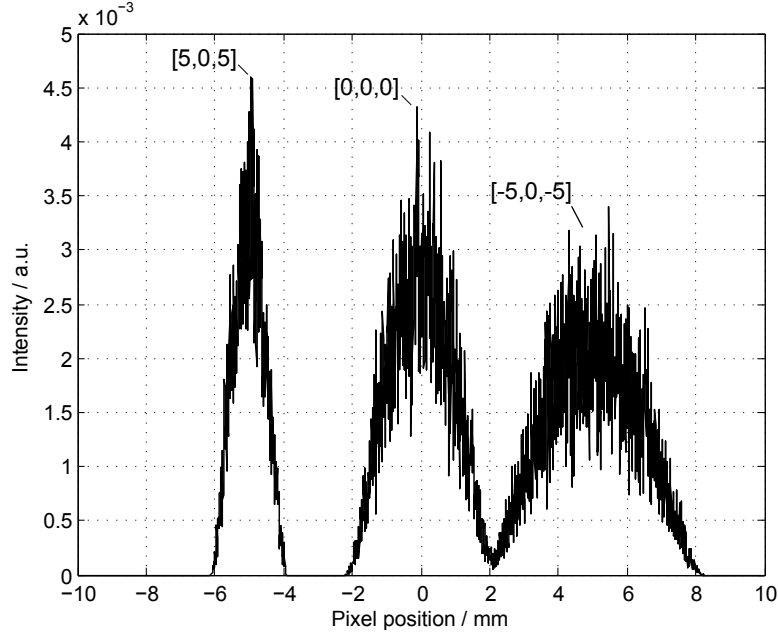


Figure 38: Intensity as function of pixel position for three imaged particles. The coordinates $[x, y, z]$ (in mm) correspond to the positions of the imaged particles. The numerical aperture of the fiber bundle layer was defined to be $NA = 0.2$. With longer particle-detector distances greater cones of scattered light are imaged on the detector. Even for particle 1 ($P_1 = [5, 0, 5]$) the signal blurs out over a wide range. List of parameters: see appendix (section 8).

The signal blurs out with larger distances between detector and particles. Thus bundles with a very low numerical aperture ($NA \ll 0.2$) and a high number of fibers are required for a consistent counting process. Since bundles with maximum 128 fibers and numerical apertures over $NA \geq 0.1$ are available, fiber bundles do not show high potential in a dark field setup.

In the next section the detector requirements are elaborated for the discussed imaging setups, based on the computed signals.

4.2 Detection

Two main technologies for capturing light digitally are applied nowadays; the charged coupled device (CCD) and the complementary metal oxide semiconductor (CMOS) technology. Each of them brings strengths and weaknesses with them, giving advantages in different applications. In this following section the differences between CCDs and the CMOSs are explained and the main features characterizing an image sensor are discussed.

In a CCD image sensor the photon-to-electron and the electron-to-voltage conversion takes place separately. Thus generated electrons of each pixel element are shifted to its neighbor and converted to voltage at the end of the array. In a CMOS chip the electron-to-voltage conversion takes place directly at each sensor element. Figure 39 depicts the architecture of a CCD and CMOS chip.

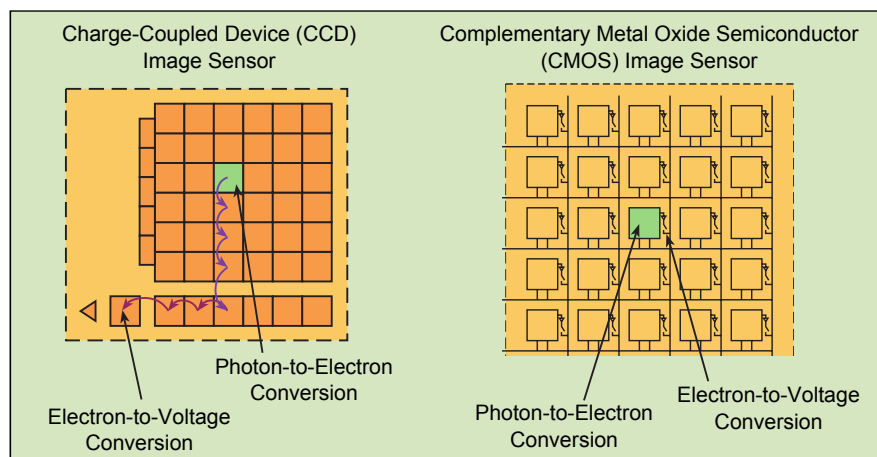


Figure 39: Architecture of a CCD and CMOS sensor: In a CCD chip (left part) the photon-to-electron and electron-to-voltage conversion is performed separately. Thus, once an array has been exposed to light, the generated electrons are shifted step by step out of the chip, to be converted into voltage. In a CMOS ship (right part) the charge generation is performed individually for each sensor element. This enables a continuous charge collection without any dead times. [24]

The CCD setup is flexible in terms of the application's demands since most functions take place on the camera's printed circuit board. Due to the fact that the charges are readout along the whole pixel array, long readout periods or rather dead times appear. In particle counters long dead times result in an increase of coincidence events, since particles could pass the illuminated area within this time span. By using the CMOS technology the signal sensing or rather the charge collection is continuous since the photon to electron and electron to voltage conversion happens on each pixel element individually. Due to this simultaneous read-out

4 DARK FIELD

process, dead times do not occur during illumination. The generated electrons are not shifted along the detector array. These two different chip architectures have significant implications in terms of sensor capabilities and limitations. The following attributes characterize the performance of an image sensor:

Responsivity:

The generated output voltage of a sensor as a function of incoming light intensity. It is stated for the linear area of the responsive curve (see figure 40). CMOS sensors are marginally superior to CCDs.

Dynamic range:

Defines the linear area of a detector. It is the ratio of the saturation equivalent exposure (*SEE*) to its noise equivalent exposure (*NEE*) value. *SEE* indicates the saturation level, *NEE* states the noise level, also referred to the signal threshold of a detector.

Read-out frequency, also known as frame rate:

States the number of generated pictures (or frames) per seconds of an imaging device. Since all of the camera functions can be placed on the image sensor and each pixel is read out individually, CMOS detectors are advantageous here. For linear detectors the term "line rate" is used.

Uniformity:

If all pixels of the detector are exposed to identical illumination conditions the generated signal does not need to be consistent. This is true especially for CMOS sensors, since the electron-to-charge conversion is performed individually for each pixel element. Continuous chip development have made the uniformity of some CMOS imagers more similar to that of CCDs.

Anti-blooming:

Blooming occurs when a light source overloads the sensitivity of a pixel and thus compromises other pixels. In general CMOS are naturally immune to blooming effects, since the single sensor elements are not connected to each other.

Shuttering:

Shuttering is the arbitrary start and stop of exposure. It controls the time interval a sensor converts incoming photons to electrons within a single read-out process. This is superior to CCD devices.

Windowing:

Windowing is the ability to read out only a small region of interest. Since CMOS chips read out each pixel separately, this technology has good ability in windowing. [23] [25]

4 DARK FIELD

In terms of a visual-based particle counter charge generation and time resolution are important parameters. Thus responsivity and read-out frequency are the critical characteristics of the detector. Considering the results of dark field simulations, the detector requirements are worked below concerning responsivity and read-out frequency. Since the frame rates of CMOSs are much higher than for CCDs and a CMOS sensor allows a continuous charge collection, the following sections are forced on the CMOS technique.

4.2.1 Responsivity

Considering the telecentric lens and the orthogonal alignment setup a high sensitivity of the detector is very important. In the nomenclature of electronic devices we are talking about responsivity, since more factors than the sensitivity of the sensor, like analogue to digital converters and amplifiers are influencing the output signal of the camera system. Thus the responsivity is a better criterion of performance. Commonly it stated by the chip manufacturers as $V/(\mu\text{J}/\text{cm}^2)$ and describes the gradient of the linear area of the response curve like it is shown in figure 40.

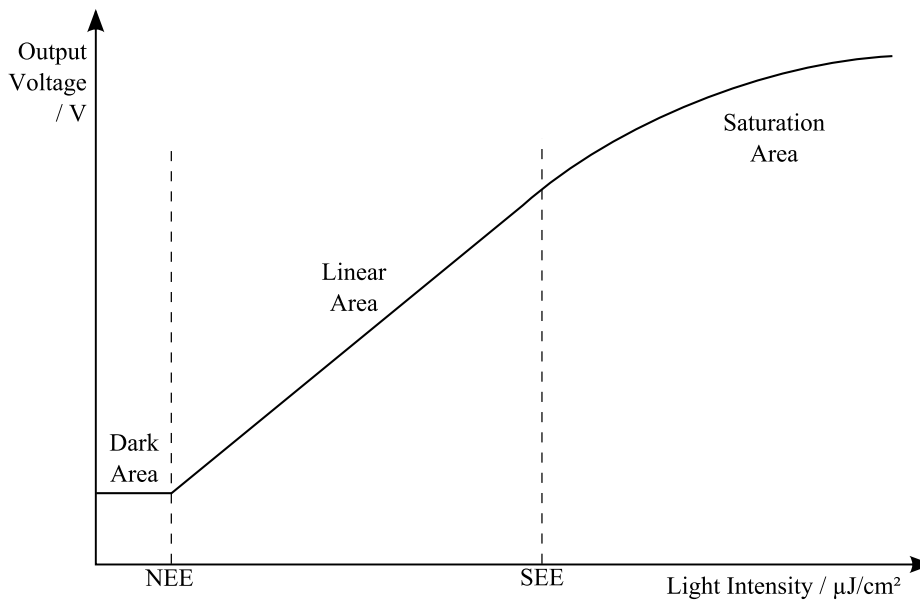


Figure 40: Responsive curve of a detector. The intensity of incoming light has to overcome the noise equivalent exposure level (NEE) to create an analyzable signal on the detector. Above the saturation equivalent exposure value (SEE) the generated voltage is not linear anymore.

Like it is shown in the graph, the response curve of a detector is subdivided into three parts.

4 DARK FIELD

The first part, which is called the dark area, is the region where the incoming light generates a non-detectable signal on the sensor. If the intensity reaches the noise level, called the noise equivalent exposure (NEE), the sensor starts to generate an output voltage. The signal increases linearly with incoming light intensity. Above the saturation equivalent exposure (SEE) value the sensor response does not behave linearly. [22]

The important criterion regarding dark field setups is the NEE -value. The intensity of incoming light needs to overcome this threshold value to generate a noticeable signal on the detector. Therefore the NEE should be as low as possible, to assure the measurability of low intensities. The following equation states the condition for the detector in terms of responsivity:

$$NEE_{\text{detector}} \stackrel{!}{<} I_{\text{light}} \cdot t_{\text{exposure}} \quad (15)$$

To determine the maximum NEE of the detector the intensity of the incoming light and the time a particle remains within the illuminated area need to be known. The detector converts charge continuously, since it is assumed to be a CMOS chip. Thus, the time a particle remains in the laser beam is equal to the exposure time t_{exposure} . For the simulations in section 2 the minimal exposure time was stated to be $t_{\text{exposure}} = 0.1$ ms, which is the time it takes the fastest particle to pass the illuminated area. These fastest particles generate the lowest possible signal on the detector. Slower particles stay within the illuminated area for a longer time and therefore, create a signal over a longer time span anyway. In this case the read-out frequency of the detector is the limiting factor (see section 4.2.2). But to ensure that even the fastest particles are detectable, following consideration are based on short exposure times ($t_{\text{exposure}} = 0.1$ ms).

In the next figure the transit of a particle and its corresponding detector signal, generated in a telecentric lens-setup is shown (Setup: see figure 4.1.2). The particle immediately generates a significant signal on the detector when it touches the laser beam. As depicted in figure 41 the generated total power of particles positioned at $y_1 = -5 \mu\text{m}$ and $y_2 = 5 \mu\text{m}$ is in the same order like for particles positioned in between. Thus the minimum exposure time can be assumed to be:

$$t_{\text{exposure,min}} = 0.14 \text{ ms}$$

This is the time span for the fastest particle to travel a distance of $y = 15 \mu\text{m}$ vertically. The velocity of the fastest particle was determined in section 2 to: $v_{\text{max}} = 10.6 \frac{\text{cm}}{\text{s}}$.

4 DARK FIELD

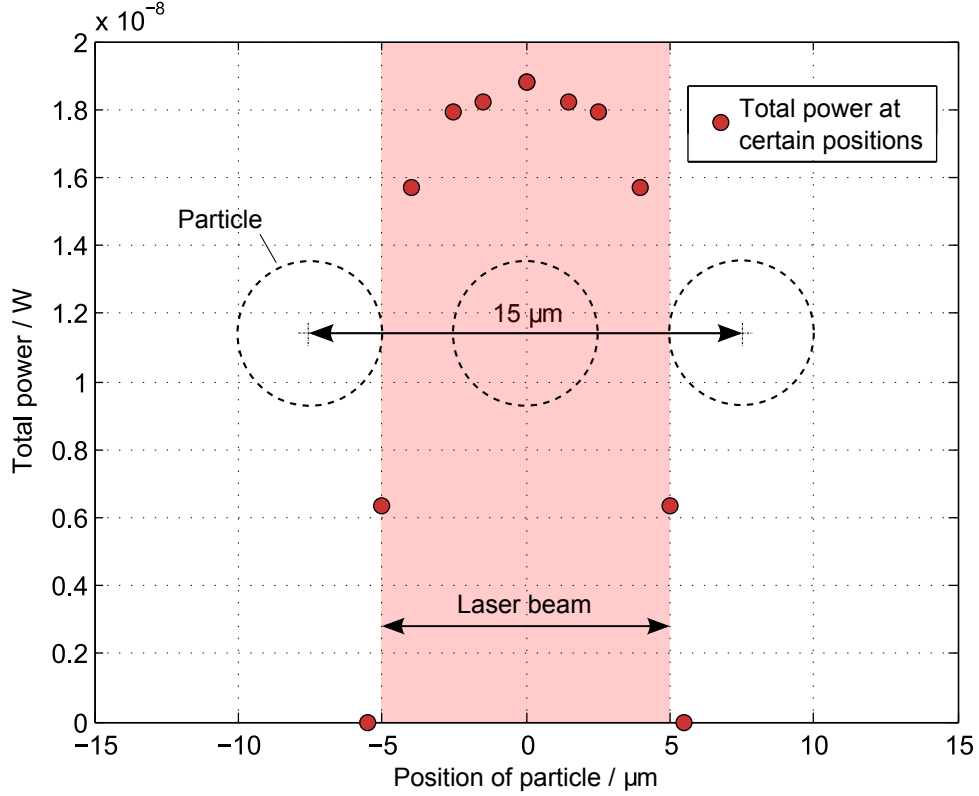


Figure 41: Generated signal as a function of particle position in a telecentric lens setup. For a distance of $15 \mu\text{m}$ in vertical direction a particle generates a significant signal. List of parameters: see appendix (section 8).

Since the detector will work with a certain read-out frequency the minimal exposure time needs to be divided by two. This considers the event a fast particle is imaged within two read-out processes. Thus, only the half exposure time contributes effectively to the charge generation within a single read-out process. Therefore, the minimal exposure time has to be stated as:

$$t_{\text{exposure,min}} = 0.07 \text{ ms}$$

The generated total power by a single particle in the telecentric lens and the orthogonal setup was computed in section 4.1 to:

$$P_{\text{sim}} \approx 10^{-8} \text{ W}$$

4 DARK FIELD

With the effective detector area of $A = (0.2 \times 0.2) \text{ cm}^2$ the intensity can be calculated to:

$$I_{\text{sim}} = \frac{P_{\text{sim}}}{A} = 2.5 \cdot 10^{-3} \frac{\text{W}}{\text{m}^2}$$

To determine the required NEE -value of the detector the intensity needs to be multiplied by the exposure time.

$$NEE_{\text{detector}} \stackrel{!}{<} I_{\text{sim}} \cdot t_{\text{exposure}} = 1.88 \cdot 10^{-7} \frac{\text{J}}{\text{m}^2} = 1.88 \cdot 10^{-2} \frac{\text{nJ}}{\text{cm}^2}$$

Thus, the required NEE -value for the telecentric lens and orthogonal setup including a $P_{\text{laser}} = 0.1 \text{ W}$ light source can be stated as:

$$NEE_{\text{detector}} \lesssim 10^{-2} \frac{\text{nJ}}{\text{cm}^2} = 10 \frac{\text{pJ}}{\text{cm}^2}$$

Noise levels of common detectors are in a range of $\sim 10 \frac{\text{pJ}}{\text{cm}^2}$. Therefore the amount of imaged scattered light is not in a sufficiently high range to generate charge on the detector. A higher laser power than $P_{\text{Laser}} = 0.1 \text{ W}$ would increase the amount of scattered light and hence the incoming intensity on the detector significantly (see section 4.3). For larger aperture diameters in the telecentric lens setup the generated signal on the detector would be increased as well since the angle of aperture opens. But this would decrease the optical resolution of the system.

In a dark field setup the SEE is not a critical value since the system only has to distinguish between particle or no particle. Therefore, a proportionality in intensity is not an important requirement. With the small amount of scattered light which is imaged on the detector in a telecentric lens setup the SEE would never be reached anyway.

Next section discusses the minimum line rate which is necessary to obtain the maximum counting limit.

4.2.2 Read-out frequency

The minimum NEE determined in the section above was calculated for the fastest particles in the system. Slower particles generate a signal over a much longer time span. Thus the minimum line rate to gain the maximum intensity without decreasing the counting limit needs to be determined.

A simulation run to determine the counting limit for different line rates was performed using the *Matlab*-routine, as was introduced in section 2. A constant, turbulent and laminar

4 DARK FIELD

particle distributions by using a 4000 pixel array detector were considered. The computed counting limits for certain line rates are plotted in the following figure. The dashed line indicates the line rate, where the maximum counting limit or rather 100% of performance is reached.

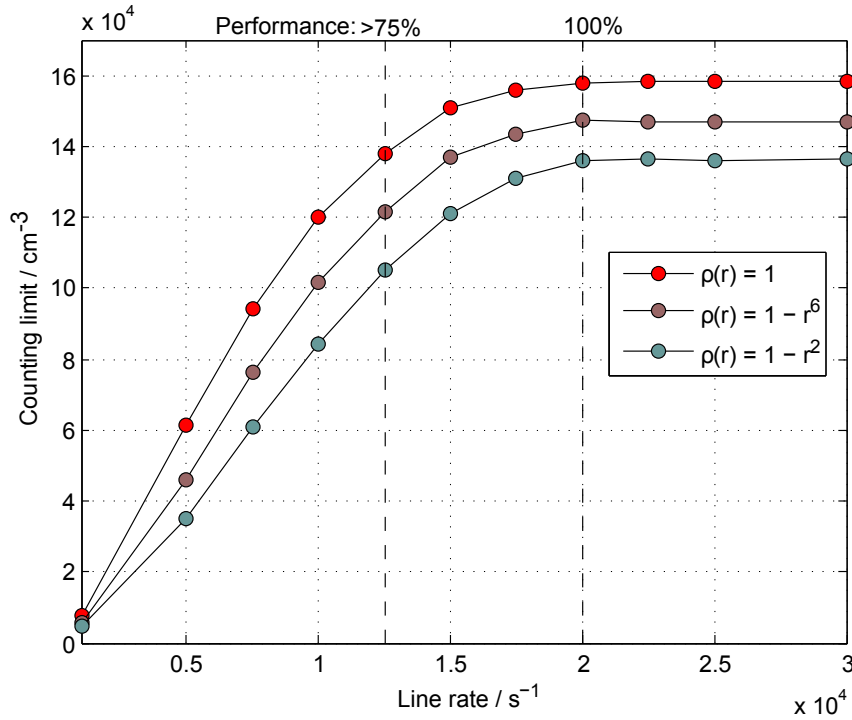


Figure 42: Counting limit as a function of line rate and particle distribution. Above 20000 lines per second, 100% performance is reached and no more time-dependent coincidence events appear. At 12500 lines per seconds still 75% of the maximum counting limit is achievable. The particle distribution does not effect the performance. List of parameters: see appendix (section 8).

As the simulation results in figure 42 show, the minimum line rate to obtain the maximum counting limit is ensured with 20000 lines per second. This is the point where the fastest particles are resolved in time at least once. Thus, a detector with a higher line rate is not necessary to gain maximum performance. Next figure depicts the same simulation like in figure 42 but for different numbers of pixels. The simulation was performed for a laminar particle distribution. As it was expected the minimum line rate to obtain the maximum counting limit is independent of number of pixel. Figure 43 indicates that time and spatial resolution are not linked.

4 DARK FIELD

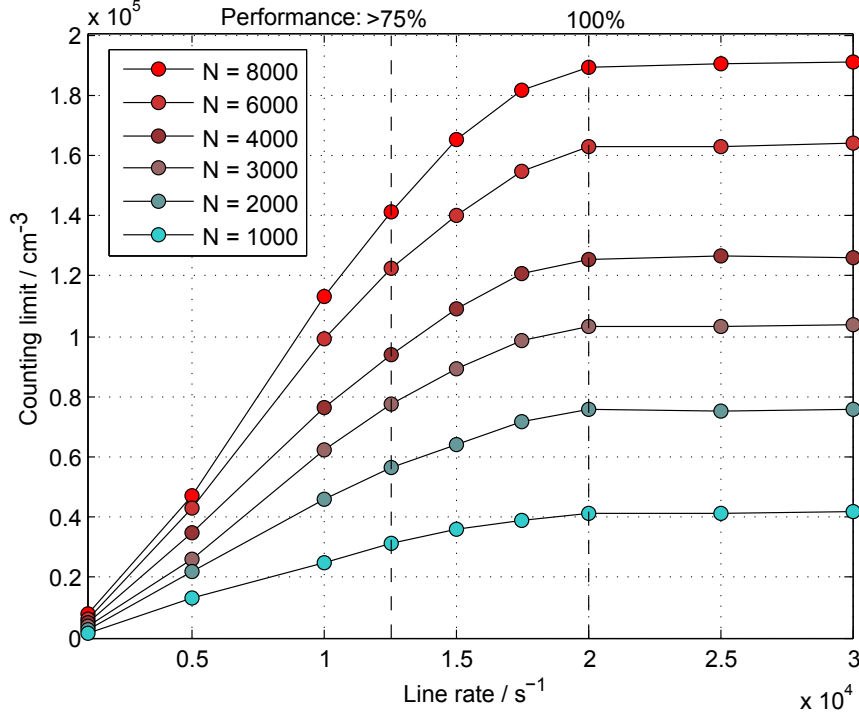


Figure 43: Counting limit as a function of the line rate for different pixel numbers N . The distribution of particles was chosen to be $\rho(r) = 1 - r^2$. As expected, the minimum line rate stays constant for different pixel numbers. List of parameters: see appendix (section 8).

Since a longer exposure time or rather a lower line rate increases the signal on the detector, a compromise between counting limit and exposure time needs to be found (The exposure time is assumed to be as long as a read-out process lasts). In the section above the required NEE -value was elaborated for signals generated by the fastest particles. To stay in this signal range the exposure time, which is defined by the line rate, should not be shorter than $t_{\text{exposure, min}} = 0.07$ ms. $t_{\text{exposure, min}}$ is the time the fastest particle remains within the illuminated area or rather generates a signal. A line rate of 12500 lines per second is equal to a exposure time of $t_{\text{exposure}} = 0.08$ ms. This ensures a maximum charge generation of fast particles. For a line rate of 20000 lines per seconds ($t_{\text{exposure}} = 0.05$ ms) maximum charge generation is not ensured anymore. Thus the required line rate for the detector is stated as:

Required line rate: 12500 lines / second

4 DARK FIELD

4.3 Illumination

Since the simulations in section 4.1 showed that high intensities are required for generating a sufficient signal on the detector, the usage of a focused laser beam is inevitable. This section discusses the requirements on a laser beam in the dark field regime in terms of power and collimation.

4.3.1 Power

To generate a sufficient signal output from the scattering process the power of the laser should be as high as possible. Common methods in the particle measurements industry, except for the laser induced incandescence (LII) method, apply lasers in the ~ 100 mW regime. This refers to the laser class 3B. Apart from the much higher price level, high power lasers in a commercial particle counter need to fulfill a lot of safety requirements. Thus, a laser in a higher class than 3B is excluded.

4.3.2 Collimation

A collimated laser beam is a prerequisite in order to generate a sufficient signal across the whole pipe diameter. For divergent flat laser beams the intensity drops with the distance to the focus line. If the effective line width, which is the width at $\frac{1}{e^2}$ intensity maximum, increases, the probability for two particles passing consecutively within a read-out process rises. Thus, a simulation using the *Matlab*-routine was performed to determine the counting limit as function of the line rate for several line widths. The computation was based on an orthogonal alignment of two linear detectors. Each detector was assumed with 4000 pixel elements. The line width was varied from $W = 5 \mu\text{m}$ to $W = 30 \mu\text{m}$ in $5 \mu\text{m}$ steps.

As depicted in figure 44, a high dependency of counting limit with respect to the line width is observable. For wider laser beams the maximum counting limit decreases. To reach the maximum counting limit for thin laser beams (e.g. $W = 5 \mu\text{m}$) line rates above 30000 lines per seconds are required. This simulation was performed for a perfectly collimated beam. Since common lasers do not get along without divergence angles, a beam which broadens with the distance needs to be treated. Thus a simulation, including a flat laser beam with $10 \mu\text{m}$ line width at focus position, was performed for different divergence angles. The computed counting limits as a function of line rate are plotted in figure 45. With larger divergence angles the counting limit and the minimal line rate in order to obtain maximum performance decreases.

4 DARK FIELD

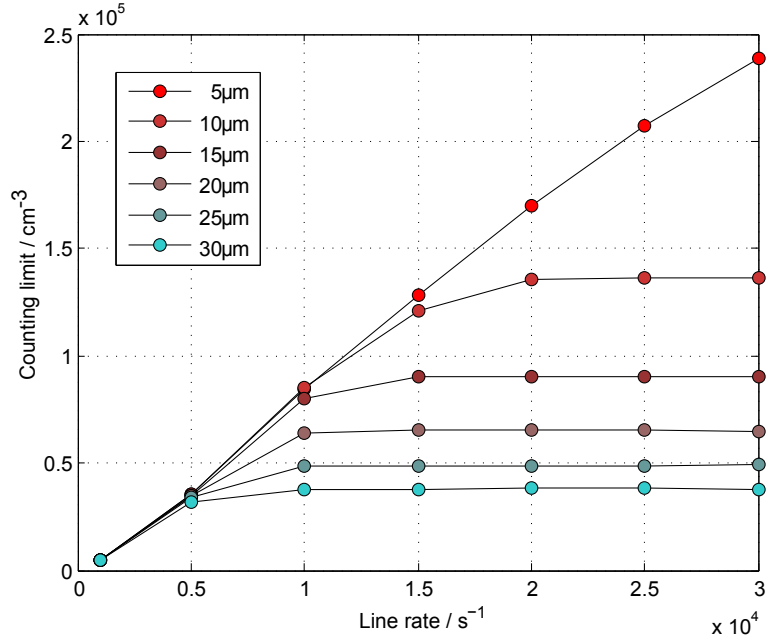


Figure 44: Counting limits for certain line widths as a function of line rate. Small changes in line width cause huge drops in counting limit. With decreasing line width of the laser the minimum line rate to gain maximum performance increases. Parameters: see appendix.

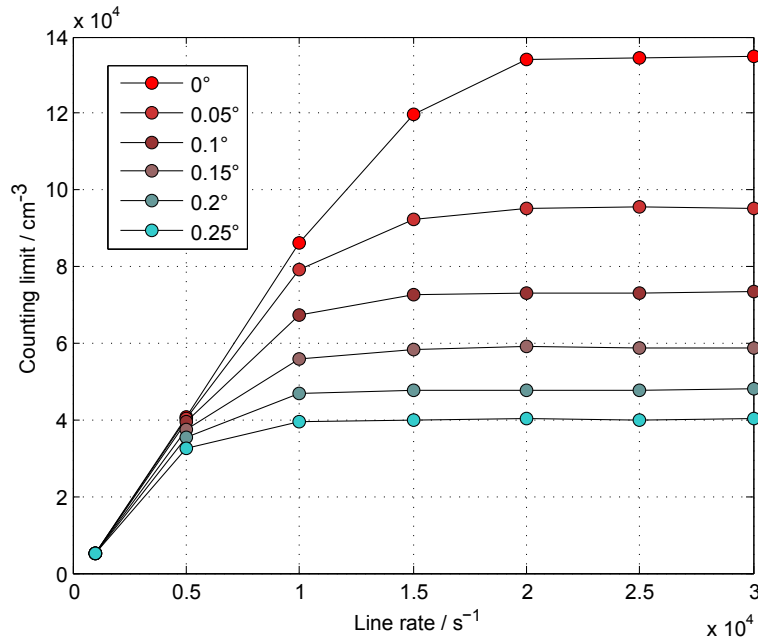


Figure 45: Counting limit as function of line rate for different divergence angles. For larger angles the maximum counting limit drops, since the laser beam broadens over the pipe cross-section. List of parameters: see appendix (section 8).

4 DARK FIELD

Both parameters (line width and divergence angle) of common laser line generators behave inversely. Thin laser lines ($\sim 10 \mu\text{m}$) are only available with large divergence angles ($\gg 0.2^\circ$) and vice versa. Thus the elaborated light source requirements cannot be fulfilled by common laser line generators. A signal analysis is indispensable. Two theoretical ways to identify time dependent coincidence cases by a signal analysis are discussed in the following:

Linearity in charge generation: The generated charge on the detector is linearly dependent on the number of particles within the light band (see figure 40). If two particles pass the flat laser beam consecutively, the generated signal on the detector should double (next figure, right part). This could be used to identify coincidence events.

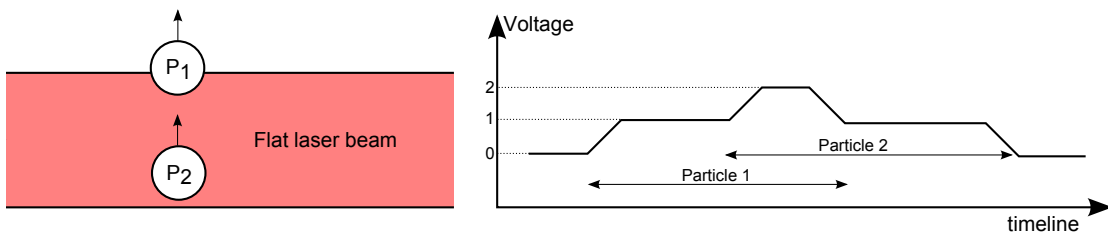


Figure 46: Left picture: Two particles pass the illuminated area in a row. Thus, they generate charge on the detector at once. Right picture: Generated voltage by a single pixel as a function of time for a high line rate. The voltage doubles while two particles are within the illuminated area.

Image processing: A second way to identify time dependent coincidence cases is the usage of an efficient image processing. The following figure depicts a matrix of pixel elements which is illuminated by two particles.

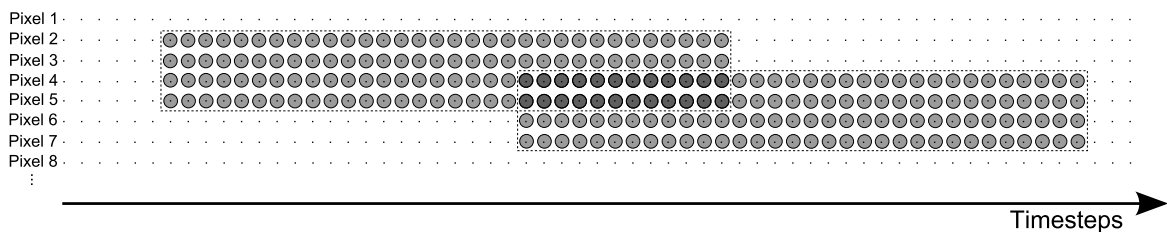


Figure 47: Pixel matrix for different time steps. The gray shaded circles indicate two imaged particles. In this scheme always 4 pixels are illuminated since in practice, the imaging of a particle on one single pixel is almost impossible. An algorithm which processes a binary matrix like this could identify coincidence cases.

By setting a comparator threshold a 0-1-matrix can be generated and processed by an image analysis algorithm. Therefore, particles which cross the light band consecutively can be distinguished.

4.4 Summary

The optical setups for a dark field implementation were introduced in this section in terms of imaging quality, detector and light source requirements. In the following section the advantages ("+") and disadvantages ("-") are summarized for each setup and a short evaluation concerning the feasibility is given.

1. Simple imaging using two aspherical lenses

- + The basic and cheap setup shows high potential for realization.
- + High quantum yields due to large angle of apertures and the possibility of imaging forward scattered light.
- Only particles within the focal plane are focused on the detector.

An multi lens system is necessary to image particles aside the focal plane. Therefore, this basic optic is not sufficient for a consistent particle number analysis in a two-dimensional detector setup.

2. Telecentric lens setup

- + Due to the small angle of aperture the depth of focus is increased. All particles, independent of their position, are imaged sharply on the detector.
- + Forward scattered light is focused on the detector.
- Only parallel rays or rather light within a very small cone (which is defined by the diameter of aperture), is imaged on the detector.

Due to the small numerical aperture of the setup only a small fraction of scattered light is imaged on the detector. Therefore, the sensitivity of detector is the main criterion for realization of this setup. Since the noise levels (NEE) of common photo detectors are in the range of the generated intensity, charge generation is not guaranteed by a single particle.

3. Orthogonal alignment

- + Due to the orthogonal alignment, particles with arbitrary positions are imaged properly on the detector.
- + Since large lenses are applicable a bigger stray light cone is imaged on the detector.
- The total amount of generated signal is in a very low range.
- A powerful signal analysis is necessary since the detector is two-dimensional and not just a linear pixel array.
- High frames rates are necessary to gain maximum performance in terms of

4 DARK FIELD

coincidence probability.

Since light from the $\varphi = 90^\circ$ scattering regime is imaged, the generated signal is in the same low intensity range as the telecentric lens setup. Therefore, the detector requirements in terms of noise level cannot be fulfilled. Additionally, high frame rates and the complex signal analysis indicates that this dark field setup is not feasible.

4. Scheimpflug alignment

- + The geometric principle of Scheimpflug allows tilting the focal plane and gain maximum sharpness anyhow.
- + Scattered light from higher intensity regions is imaged on the detector.
- High frame rates and a complex signal analysis is necessary.

By using a detector with a very low noise level, charge generation is possible. Since two-dimensional matrix cameras with frame rates beyond 10000 frames per seconds are not available, a Scheimpflug setup is not feasible for this application.

5. Fiber bundles

- + Gaining spatial resolution due to the numerical aperture of the single fibers.
- The signal width on the detector is a function of the distance between fiber bundle and particle.
- The signal strength on the detector drops with the numerical aperture.

Fiber bundles with low numerical apertures and a high number of fibers are necessary for a consistent analysis. Bundles which fulfill these requirements are not available in the basic range of products.

Conclusion:

A spatially resolved particle counter in the dark field mode is not feasible for the approaches discussed in this thesis. Since most optical setups require small angles of aperture to realize sharp images, the amount of scattered light is not sufficient to generate a signal on the detector. A way to overcome the low signal to noise ratio can be realized by a special alignment which obeys the geometric rule of Scheimpflug. Since the generated signal is still in a critical range and two-dimensional matrix arrays are not available for sufficiently high frame rates the Scheimpflug alignment is not realizable either. Therefore, a visual-based particle counter in the dark field regime, taking into account the detector and laser requirements in a two dimensional setup, is not feasible with common technology.

5 Bright field

In the bright field mode different requirements in terms of optic, detector and light source are crucial compared to the dark field setups discussed above. As depicted in figure 27, a detector in the bright field mode is positioned directly within the flat laser beam. Thus, the contrast is gained by attenuation caused by absorbed and scattered light. This section discusses the ways of removing scattered light and obtaining spatial resolution exclusively in the bright field regime.

5.1 Imaging setups

5.1.1 Aperture stop setup

By removing scattered light in the bright field regime maximum contrast can be obtained. Therefore a setup like shown in the next figure is most promising.

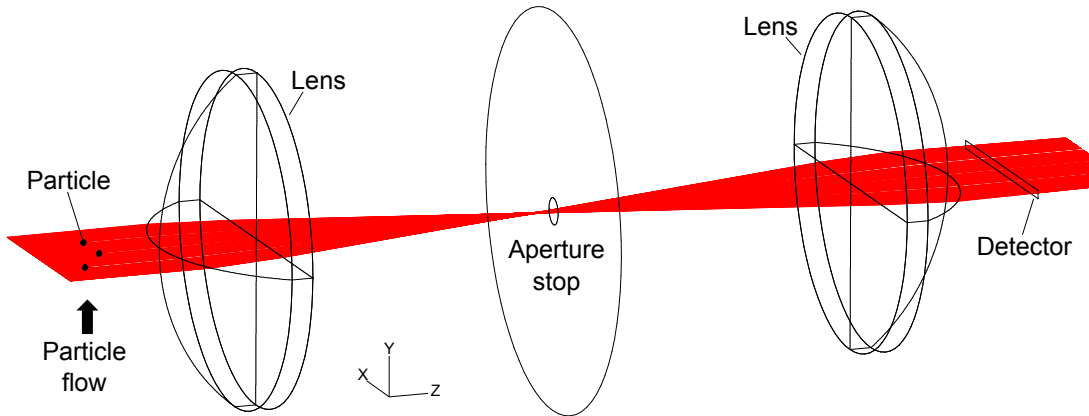


Figure 48: Bright field setup of a visual-based particle counter. A flat laser beam (from the left) is focused by a lens and collimated again behind an aperture stop. Therefore, scattered light is removed. The detector (right side) is positioned directly within the light band.

Particles which pass the illuminated area (shown in figure 48) scatter and absorb light. This causes an attenuation in detector signal at the positions of the particles. In a setup like this, an additional imaging optic is not necessary, if we assume that the beam is highly collimated. The following figure shows the detector intensity as a function of pixel position for a simulation with 4×10^9 analysis rays. Three particles were positioned within the flat laser beam. For the purpose of detection a 4096×1 pixel sensor was positioned behind the second lens directly into the flat laser beam.

5 BRIGHT FIELD

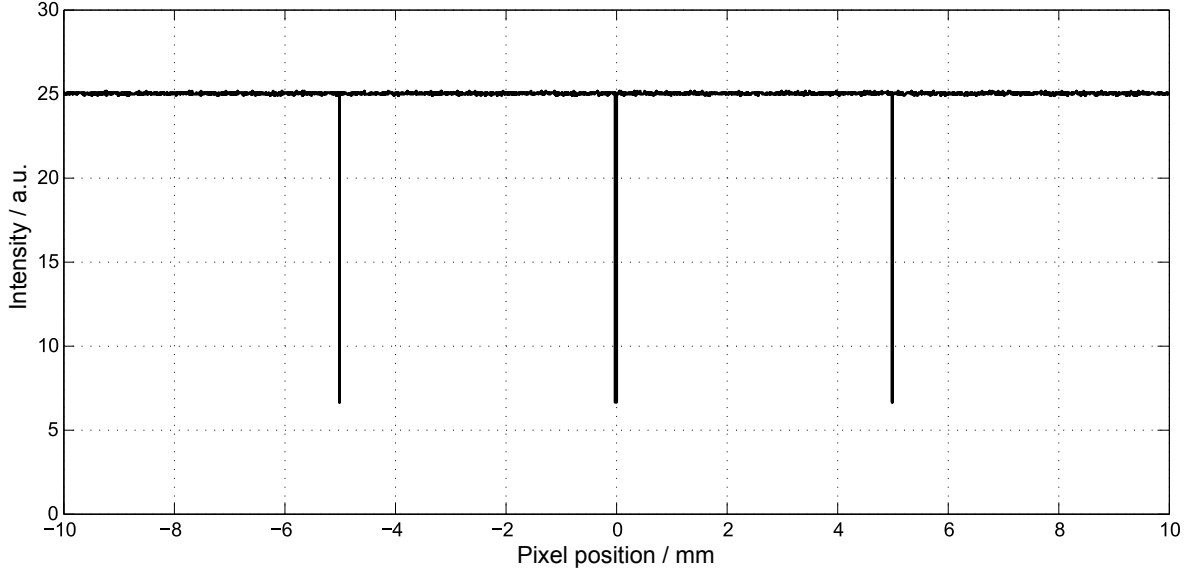


Figure 49: Detector intensity of a bright field setup as a function of pixel position. The particles within the flat laser beam cause a consistent signal attenuation, independent of their positions. List of parameters: see appendix (section 8).

The plot in figure 49 shows a drop in intensity at the positions of the particles. The simulation was performed in the non-sequential mode. This means only classical traced rays are considered. Since the collimated light source illuminates the detector directly diffraction becomes important. The flat laser beam is diffracted by particles and thus the disturbed beam is imaged. In *Zemax* it is not possible to simulate diffraction in the non-sequential mode. As a consequence, a separate simulation using "physical optics propagation" in the sequential mode was performed. The next figure depicts a diffracted beam by a single particle and an undisturbed beam propagating the same distance without inhomogeneity in logarithmic scale. The detector was positioned in 10 mm distance to the particle. For different distances the diffraction pattern does not change its shape, it just broadens and the absolute irradiance drops. Thus the differences between disturbed and undisturbed beam are crucial. The initial beam, which is assumed to be highly collimated (divergence angle: $\varphi = 0.1^\circ$) is diffracted by the particle with a diameter of $D_{\text{particle}} = 5 \mu\text{m}$. As shown in figure 50 the diffraction patterns occur over a wide range. The irradiance of the diffracted beam at position zero is decreased by a factor of $\sim 10^4$ compared to not diffracted beam. Therefore, diffraction does not effect the attenuation contrast, caused by the particles significantly. To minimize diffraction effects in the bright field setup small aperture diameters can be used. Since a diffracted beam broadens with optical length or rather with detector distance, a compact setup will reduce diffraction effects as well.

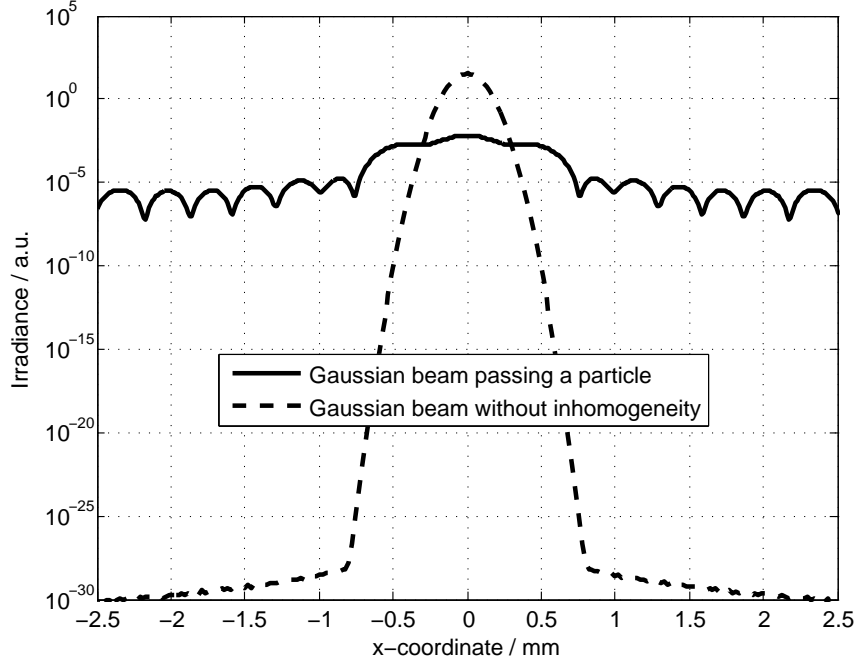


Figure 50: Detector irradiance of a Gauss beam simulated in the sequential mode. The dashed line shows the beam without particle or rather without inhomogeneity. The continuous line indicates the diffracted beam as a consequence of the $5\ \mu\text{m}$ particle. Besides the widened main peak, the diffraction patterns are clearly visible in the logarithmic scale. List of parameters: see appendix (section 8).

5.1.2 Fiber bundles

Instead of applying an aperture stop to remove scattered light, fiber bundles may be used (introduced in section 4.1.5). With fiber bundles short optical lengths are realizable and therefore, diffraction effects can be avoided. Bundles with a high number of fibers (>500 fibers) and low numerical apertures are required in order to obtain great spatial resolution. If these bundles are available someday, more investigations can be done in a second step.

5.2 Detection

In a bright field setup the detector is illuminated permanently. It is very important to keep in mind that in this setup the width of the flat light beam is not essential. The height of the detector defines the area which is dimmed by passing particles.

5 BRIGHT FIELD

5.2.1 Responsivity

An important criterion in a bright field setup is the responsivity R_{detector} of the detector. It must be high enough to generate a voltage signal which overcomes the noise:

$$R_{\text{detector}} \cdot \Delta I \stackrel{!}{>} \text{Noise} \quad (16)$$

ΔI indicates the signal attenuation caused by a single particle. It is determined by the laser intensity I_0 and the attenuation factor A .

$$\Delta I = I_0 \cdot A; \quad 0 \leq A \leq 1 \quad (17)$$

Thus the condition for the responsivity R_{detector} can be stated as:

$$R_{\text{detector}} \stackrel{!}{>} \frac{\text{Noise}}{I_0 \cdot A} \quad (18)$$

To determine the required responsivity R_{detector} the signal attenuation caused by a passing particle needs to be known. In a simulation with **Zemax** the signal attenuation as a function of particle position was determined. The particle was assumed to pass two pixel elements in between. This alignment ensures the worst case in terms of signal attenuation. For example a particle positioned directly in front of one pixel would cause a much higher attenuation. The simulation was performed for three particle diameters: $D = 2.5 \mu\text{m}$, $D = 5 \mu\text{m}$ and $D = 7.5 \mu\text{m}$. The size of a single pixel element was assumed to be $5 \mu\text{m} \times 5 \mu\text{m}$. Following figure depicts the relative signal attenuation as a function of vertical particle position. The attenuation factor A was computed by integrating over a certain distance x_{max} . x_{max} is given by the distance the fastest particle travels within a read-out process. The read-out frequency was assumed to be 12500 lines per second. For higher read-out frequencies the exposure time or rather x_{max} decreases. Thus, the integrated attenuation within a single read-out process increases.

As depicted in figure 51 a particle with a diameter of $5 \mu\text{m}$ generates an effective signal attenuation of $\sim 12\%$ at least within one read out process on a single detector pixel. For a small particle ($D = 2.5 \mu\text{m}$) with a diameter below the detector length the effective attenuation drops. For a particle with a diameter of $D = 7.5 \mu\text{m}$ the effective signal attenuation for 12500 lines per second rises up to 26%. Theoretically, with very high read-out frequencies the effective attenuation is increasable up to $\sim 62.5\%$ (see attenuation maximum at position zero in figure 51 for $D = 7.5 \mu\text{m}$).

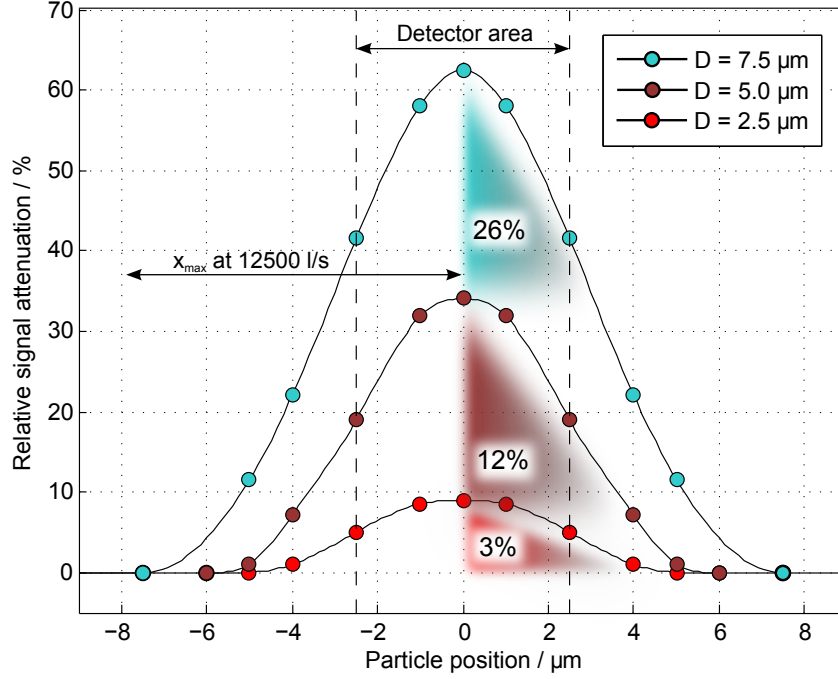


Figure 51: Signal attenuation as a function of particle position for three particle diameters. The size of a single detector element ($5 \mu\text{m} \times 5 \mu\text{m}$) is marked in the plot with two dashed lines. The three per cent declarations indicate the effective attenuation the fastest particle causes within a single read out process (12500 lines per seconds). x_{max} indicates the distance this particle travels within a read out process. List of parameters: see appendix (section 8).

For different intensities the relative signal attenuation caused by a particle stays constant, as well as the absolute noise value of a photo diode does. By applying a working intensity I_0 at the SEE level, the responsivity must overcome only a very low value to ensure sufficient charge generation. SEE and signal noise of common detectors are in a range of:

$$SEE = 75 \frac{\text{nJ}}{\text{cm}^2}$$

$$\text{Noise} = 0.1\text{mV}$$

By applying a light intensity at the saturation limit ($I_0 = SEE$), the responsivity can be determined by equation 18 to:

$$R_{\text{detector}} \stackrel{!}{>} 0.1 \frac{\text{V}}{\frac{\mu\text{J}}{\text{cm}^2}}$$

5 BRIGHT FIELD

The responsivity for common detectors lies in a range of:

$$R_{\text{detector}} = 10 \frac{\text{V}}{\frac{\mu\text{J}}{\text{cm}^2}}$$

Thus the responsivity of these common detectors is in a sufficient high range. Even at a working point of $I_0 = 0.1 \cdot SEE$, the responsivity is high enough to generate a sufficient contrast:

$$R_{I_0=SEE \cdot 0.1} = 1.1 \frac{\text{V}}{\frac{\mu\text{J}}{\text{cm}^2}}$$

$R_{I_0=SEE \cdot 0.1}$ is the required responsivity (determined with equation 18) for a setup operating the light source at $I_0 = 0.1 \cdot SEE$. R_{detector} of common detectors is still in a higher range. To keep the output voltage below the saturation limit and therefore, in the linear range (see figure 40) the output power of the light source has to be chosen properly. As a consequence, the condition in terms of saturation limit can be stated as:

$$SEE_{\text{detector}} \stackrel{!}{>} I_{\text{laser}} \cdot t_{\text{exposure}} \quad (19)$$

Like introduced above, typical saturation limits (SEE values) are in an order of $75 \frac{\text{nJ}}{\text{cm}^2}$. With 12500 lines per seconds very low light intensities are required to stay below this critical value. With these proposed values the intensity range for the light source can be determined using equation 19 to:

$$I_{\text{laser}} < 1 \frac{\text{W}}{\text{m}^2}$$

Low power lasers below laser class 3B or LEDs fulfill this condition easily.

5.2.2 Read-out frequency

In terms of minimal read-out frequency the same requirements as the ones determined in section 4.2.2 can be stated. The dependence of counting limit on different line rates does not change in the bright field regime. Thus, the required line rate to obtain at least 75% of performance in terms of maximum counting limit can be stated as:

$$\boxed{\text{Required line rate: 12500 lines / second}}$$

To generate the highest contrast and obtain maximum performance the line rate should be chosen as high as possible. Since some detectors with an exposure control function are available, a higher contrast can be regulated additionally. (With an exposure control the exposure time within a read-out process can be specified.)

5 BRIGHT FIELD

5.3 Illumination

5.3.1 Power

Like determined in section 5.2 the condition for the intensity of the light source, using a common detector with a SEE-value of $75 \frac{nJ}{cm^2}$, can be stated as

$$I_{\text{laser}} < 1 \frac{W}{m^2}$$

Since the source's required power is in a moderate range, a laser source is not the only possibility for illumination. A LED source including a collimation system meets the power requirements as well. The application of a laser source, which basically works in higher power ranges, requires a power control. If a potentiometer turns down the laser power the noise rises in most cases. Therefore, additional filters may be applied in the setup to realize low intensities and low noise. Since the relative attenuation in the bright field setup adds up to approximately 12% (see figure 51) the noise condition for the laser can be specified as:

$$\text{Noise} \leq 1\%$$

As a matter of course the laser noise should be kept as low as possible. Common low noise lasers are in a range of 0.1% root-mean-square noise.

5.3.2 Collimation

To ensure a consistent intensity drop, caused by a passing particle, the rays of the light source need to be collimated. In terms of LEDs the emitting area is big and works like a Lambertian emitter, which can be considered diffuse. Thus, an additional set of collimators and aperture stops are necessary to ensure parallel rays. If this is not the case a drop in intensity would not be detectable any more. Therefore, the generation of a sufficiently collimated beam out of a forward-spaced LED over a wide range is necessary. Since a high level of collimation is an intrinsic characteristic of a laser, a laser should be used instead of a LED for setting up first tests and prototypes. Evaluating a LED source, including collimation and aperture stop systems should be done in a second step. The line width does not affect the measuring setup, since the height of the detector determines the observed area.

5 BRIGHT FIELD

5.4 Summary

A visual-based particle counter in the bright field regime shows a high potential in feasibility. By applying a collimated flat laser beam, a simple setup like depicted in figure 48 is sufficient in order to generate contrast on the detector. An additional objective is not necessary. Further requirements for the laser, such as the low power range and low noise are fulfilled easily.

Since the *NEE* of the detector is not crucial in a bright field setup, demands like read-out frequency or responsivity are fulfilled by almost all linear detector arrays.

In conclusion, further investigations into applying a bright field setup like discussed in this section should be done. Dark field considerations did not show potential. Thus, an experiment to verify the general feasibility of a bright field was carried out.

6 Experimental verification

The theoretical considerations in section 2 indicate a high potential in increasing the counting limit of a condensation particle counter. Dark field setups implicate huge challenges in terms of detector and light source requirements. Thus, the focus of this section lies on the verification of the feasibility of applying a bright field setup like introduced in the section above. An implementation of a new measuring cell in the condensation particle counter is not the aim of the experiment; it should rather demonstrate the general feasibility of counting particles with a bright field setup. To integrate it in the self-contained flow circuit of a condensation particle counter further investigation needs to be done. The first step here is to prove the physical characteristics and feasibility of the setup.

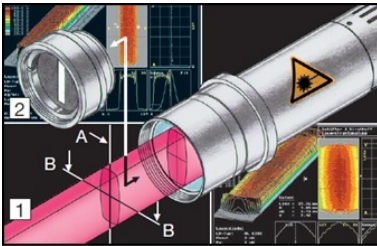
6.1 Setup

Basically the setup consists of five different units: a collimated laser beam, the particle flow, an aperture stop, a linear detector array and an analysis control for the detector. The choice and arrangement of the components is discussed and explained in the following section:

1. Collimated laser beam

The laser was provided by *Schäfter & Kirchhoff* and is characterized by a high degree of collimation and a low output power. The following table lists the properties of the laser:

Table 6: Laser data specifications

| | |
|--|----------------------------|
| Identifier: | LNC-91CM-M60-635-1-H02-H-6 |
|  | |
| Output power: | 1 mW |
| Intensity distribution: | Rectangular |
| Beam aperture: | (14×3) mm |
| Beam divergence: | 0.03 mrad |
| Wave length: | (625 ± 10) nm |

6 EXPERIMENTAL VERIFICATION

The output power is adjustable by a potentiometer from 1% up to 100%. For the power range from 20% to 100% the noise of the laser stays below $< 0.1\%$ RMS.

2. Particle flow

Since decane particles in the condensation particle counter require a self-contained system, a flexible setup for verification, independent of the condensation process is more suitable. Polystyrene (PS) spheres with $D = 20 \mu\text{m}$ nominal diameter, which are available in very narrow size distributions are used instead. The spheres are provided by *Phosphorex* (product number: 122) as colloidal dispersion. The refractive index of the particles is stated as $n_{PS} = 1.587$ at $\lambda = 632.8 \text{ nm}$ by the manufacturer. To generate the particle flow an atomizer from *Palas* (product name: AGK 2000) was applied. It is an air-supplied device which can be used to disperse the polystyrene particles. The flow rate of the atomizer is adjustable from 3 l/min to 10 l/min. The outlet diameter is stated to be $D = 2 \text{ cm}$. In the experiment a slow particle flow like assumed in the new measuring cell should be realized (Pipe diameter: $D = 2 \text{ cm}$, Flow rate: 1 l/min; see section 2.1). An applied flow rate of 3 l/min results in a maximum velocity of polystyrene spheres which is 3 times higher than the assumed velocity of decane particles. Thus the line rate of the detector needs to be three times higher than the required read-out frequency determined in the bright field section (Required read-out frequency: 12500 lines per seconds).

3. Aperture stop

An aperture stop setup basically consists of two focusing lenses and an aperture in between. The second lens is used to re-collimate the beam after it was focused by the first lens through the aperture. Two identical plan-convex lenses by *Qioptiq* (stock number: G063103322) with a diameter of $D = 31.5 \text{ mm}$ and focal length of $F = 80 \text{ mm}$ were used to focus the flat laser beam. Since the lens diameter is much bigger than the beam aperture of $(14 \times 3) \text{ mm}$, spherical aberrations are minimized. An iris aperture with a minimum diameter of $D = 0.5 \text{ mm}$ is used to remove scattered light. Since a collimated beam is imaged, the lenses need to be aligned in a way that the focus of both lenses meets at the position of aperture.

4. Detector array

A linear detector array provided by *Schäfter & Kirchhoff* is used for imaging. The following table lists the essential properties of the detector chip:

6 EXPERIMENTAL VERIFICATION

Table 7: Line detector data specifications

| | |
|---------------------------------------|--|
| Manufacturer: | <i>DALSA</i> |
| Identifier: | IT-P1-1024-B |
| Maximum line rate: | 87 kHz |
| Number of pixels: | 1024 |
| Pixel size: | $10\ \mu\text{m}$ (H) \times $10\ \mu\text{m}$ (V) |
| Responsivity: | $12\ \frac{\text{V}}{\frac{\mu\text{J}}{\text{cm}^2}}$ |
| Noise Equivalent Exposure (NEE): | $23\ \frac{\text{pJ}}{\text{cm}^2}$ |
| Saturation Equivalent Exposure (SEE): | $75\ \frac{\text{nJ}}{\text{cm}^2}$ |

The electronic implementation of this sensor by *Schäfter & Kirchhoff* still provides a maximum line rate of 45000 lines per second. This line rate is 3.5 times higher than the required read-out frequency (12500 lines per second). Thus, polystyrene spheres dispersed by the atomizer are still observable. The size of a single detector element is $10\ \mu\text{m}$ (H) \times $10\ \mu\text{m}$ (V). Since the diameter of the polystyrene spheres is $D = 20\ \mu\text{m}$ a greater signal attenuation than determined in bright field section (see figure 51) should be observable. As an interface between detector and computer an *USB 3.0* gateway is used.

5. Analysis control

Schäfter & Kirchhoff provides a driver-software for the detector and a start-up routine. It includes a direct signal illustration with the possibility of setting some main parameters, like read-out frequency. Therefore, an additional *LabVIEW*-control was required in order to implement a video functionality. The detector was operated with an 8-bit signal resolution and 43478 lines per second. This line rate promises a very high contrast (see section 5.2.1). On the other hand, it results in a huge amount of data since the number of pixels is 1024. For a measurement time of 1 second this results in $\sim 45,000,000$ points of data. Thus, the measurement time was defined as short as necessary.

All components are mounted on a plate provided by *Qioptiq* (order number: G061327000). As a consequence; specially designed and milled clamps are used to reach a consistent optical height. The following picture shows the experimental setup which was introduced above.

6 EXPERIMENTAL VERIFICATION

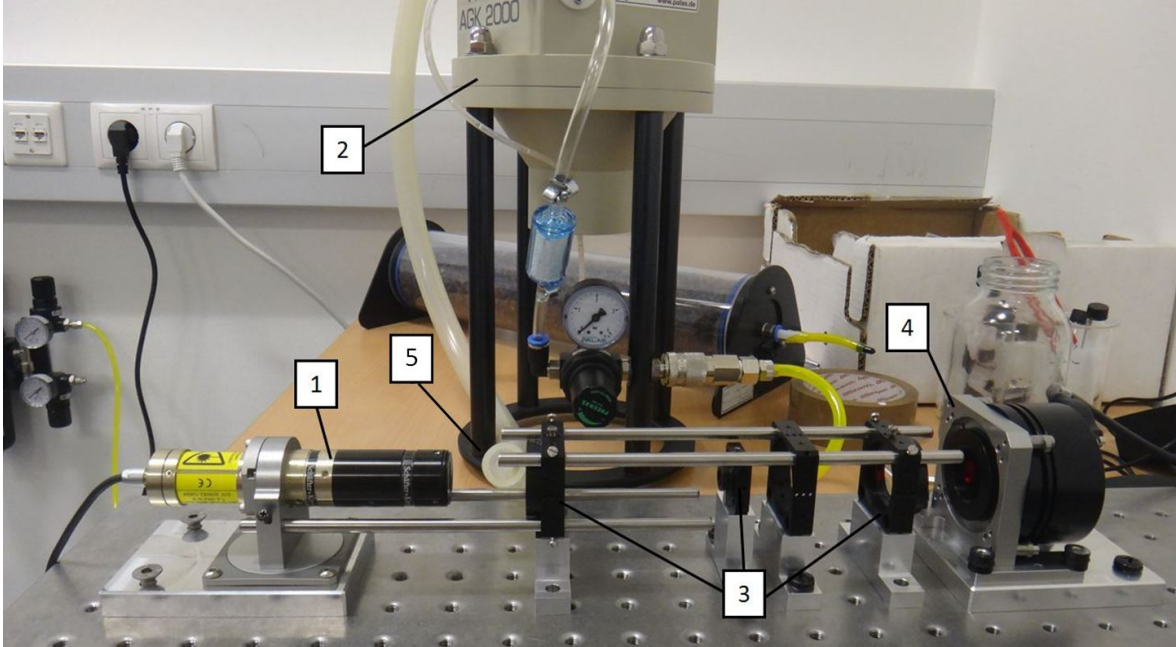


Figure 52: Laser (1), aperture stop (3) and detector (4) are mounted on a plate and aligned by rods. The atomizer (2) is supplied by compressed air and generates a vapor stream containing the polystyrene spheres. The laser is tilted 90° , so that the flow out from the hose (5) can pass the flat beam along a horizontal direction.

Since the data rate is enormous the measurement time was defined to be half a second. Basically the polystyrene percentage in the suspension is 1%. To avoid dissipation, the suspension was additionally diluted with a ratio of 1:20. In combination with short measurement times this results in rare counting events. In the next section the results of the measurements are discussed.

6 EXPERIMENTAL VERIFICATION

6.2 Results

To work out the signal attenuation a passing particle will cause, the generated laser signal on the detector without particle flow has to be known. Thus, the detector signal over 1 second measurement time was averaged. The sensor was operated with an 8-bit signal resolution and 43478 lines per second. The next figure shows the time-averaged detector signal of the laser profile without any particle flow.

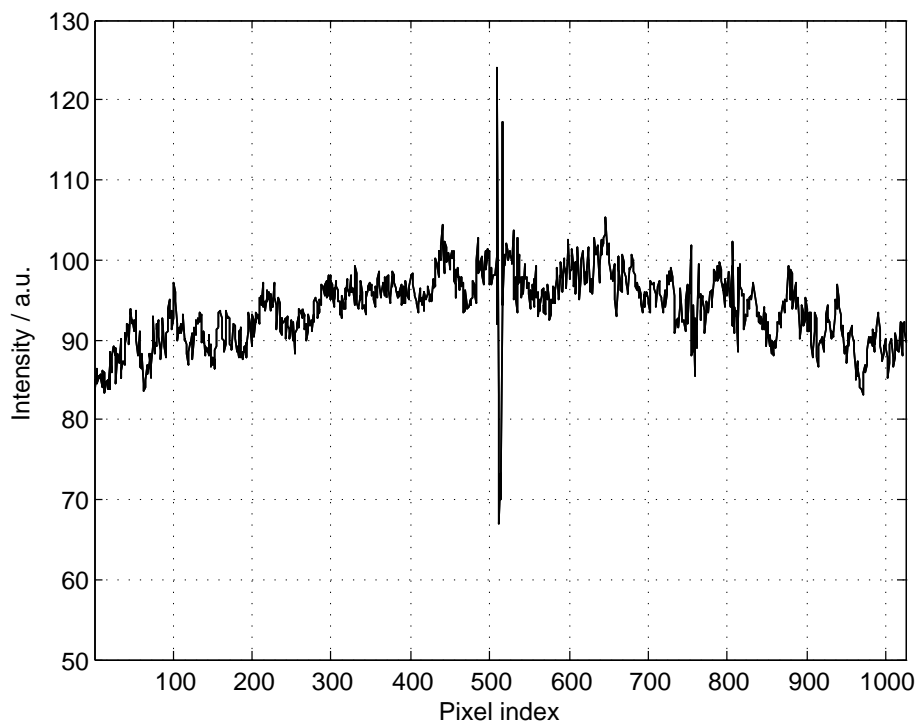


Figure 53: Time-averaged laser profile determined for one second measurement time. The detector was operated with 43478 lines per second and the laser with $P = 1$ mW. The standard deviation is not plotted in the figure since it is $< 1\%$ for all pixels and would not be visible for this plot scale anyway. Therefore, the accumulated signal noise of the laser and the detector is in a very low range.

As depicted in figure 53, the absolute laser intensity is inhomogeneously distributed over the detector area. (By moving the laser it was verified that this effect is not caused by the detector). Especially at pixel number ~ 500 a huge non-uniformity is visible. But since the noise of the laser and the detector is in a very low range (standard deviation $< 1\%$), this does not affect the measurements. The saturation region (SEE-level) of the detector starts at 256 a.u., since the *LabVIEW*-control is performed in the 8-bit ($2^8 = 256$) mode. Thus, the experiment was operated at $\sim 40\%$ SEE-level.

6 EXPERIMENTAL VERIFICATION

In the next step the detector signal with applied particle flow was stored for a measurement time of 0.5 s. The following figure depicts the detector signal as a function of time and pixel index.

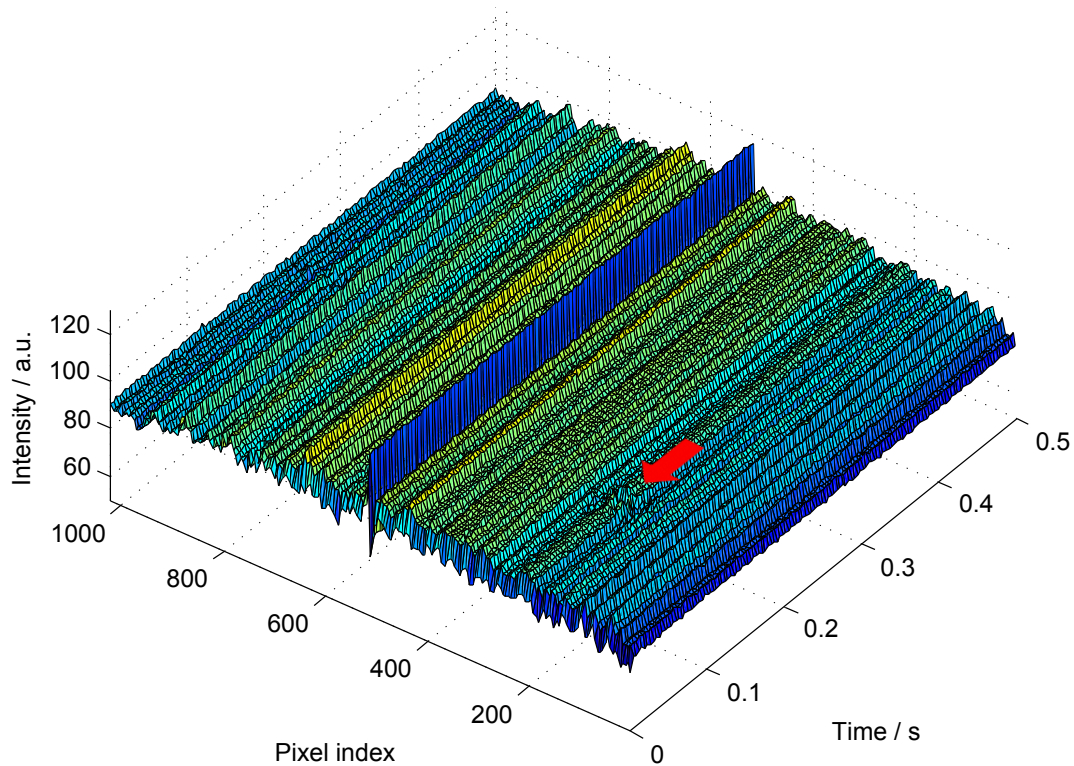


Figure 54: Detector signal as function of time and pixel index. The detector was operated with 43478 lines per second and the laser with $P = 1$ mW. Every 150th time step and 5th pixel is plotted. If the whole data is plotted, only a black surface would be visible since the amount of data in time line is so high. The red array indicates an inhomogeneity.

It seems as if the detected signal in figure 54 stays constant during the whole measurement period. But if you have a closer look at special regions (indicated by the red arrow) with higher resolution in time and space an inhomogeneity is visible. Therefore, this indicated region is plotted with high resolution in the next figure. To remove the laser profile dependent signal the time averaged signal, depicted in figure 53 was subtracted. A second, similar picture of a passing particle can be observed at $t \sim 0.25$ s at pixel 950. Since the flat laser beam is tilted by 90° and the experiment was done in a closed room it can be ruled out that gravitational accelerated dust particles generated the signal inhomogeneity.

Like figure 55 shows, a polystyrene particle which passed the flat laser beam within the 0.5 s measurement time is imaged clearly by the detector.

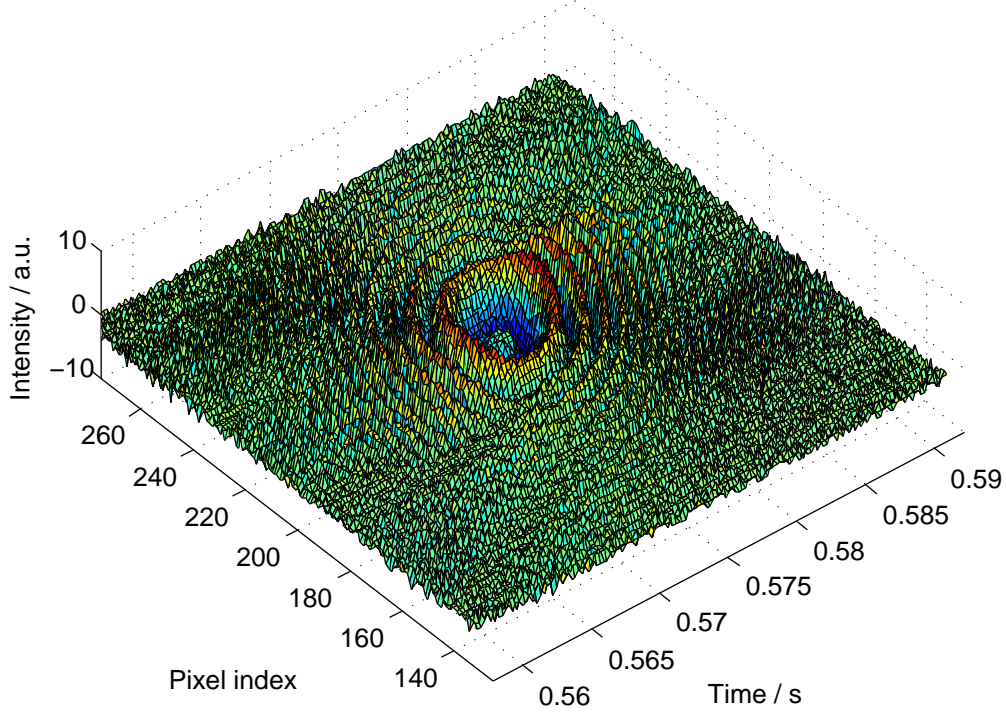


Figure 55: High resolution plot of the area with the assumed inhomogeneity from figure 54. The time-averaged laser profile is subtracted to remove the characteristic laser intensity. A particle with passes the laser beam is clearly visible.

The line rate of the detector was high enough, to detect the polystyrene sphere. Thus, a higher time-resolution is not necessary for this experiment. For detailed analysis the time line and the spatial image at the position of the particle are plotted in figure 56 and 57.

The plot in figure 56 indicates that diffraction becomes important. A possible reason for the broad disturbance is the large width of the flat laser beam ($W = 3 \text{ mm}$). A passing particle is illuminated for a long time period, and, hence generates a diffracted wave which disturbs the signal. Applying a thin rectangular aperture which reduces the illuminating time of the particle should results in a narrower peak in time-line.

Figure 57 depicts the detector signal as a function of pixel index at the time when the particle was passing the flat laser beam. Diffraction effects like observed in the time line plot are clearly visible. Since the width of a single pixel array is $10 \mu\text{m}$ and the signal attenuation extends over a range of ~ 20 pixels, the effective diameter of the particle on the detector can be determined to $D_{\text{image}} \sim 200 \mu\text{m}$. Certainly the exact diameter of the polystyrene sphere is known to be $D_{\text{real}} = 20 \mu\text{m}$. Since the diffraction effects obviously plays a role in this setup, the broadened peak can be explained by the long optical path.

6 EXPERIMENTAL VERIFICATION

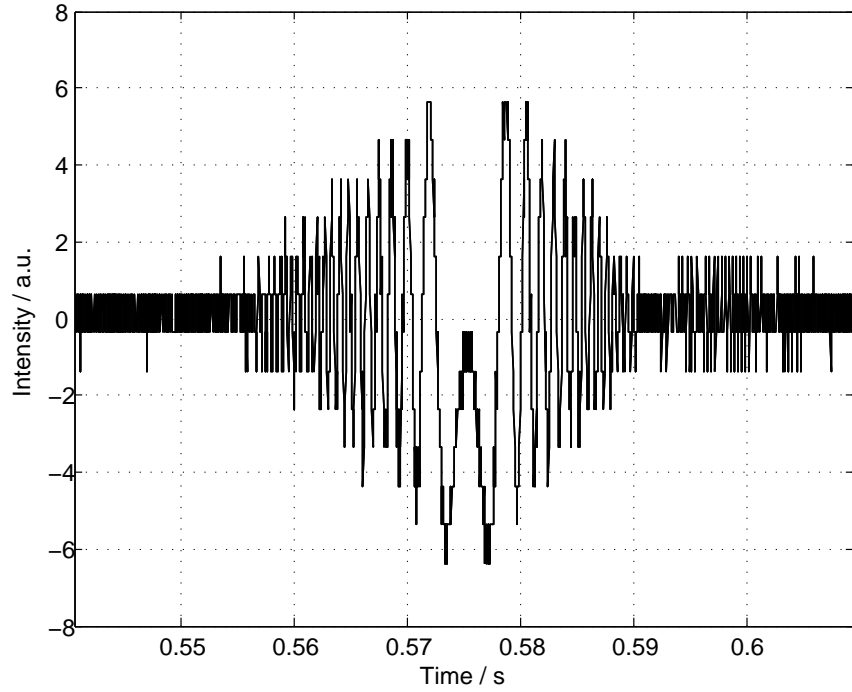


Figure 56: Time-line of the detector image at the position of the particle: Pixel no. 206 is plotted for a time period of $\tau = 70$ ms.

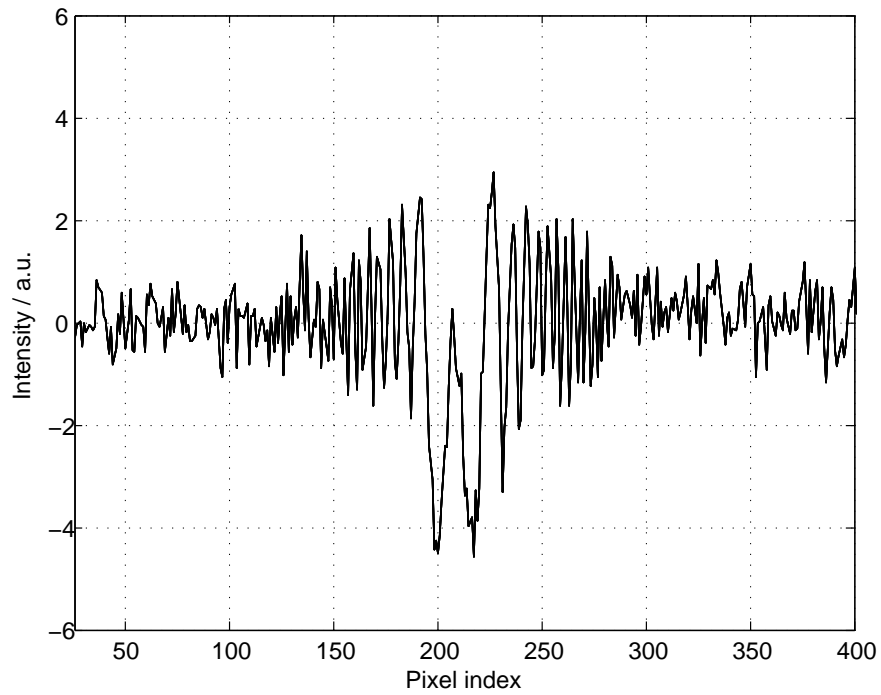


Figure 57: Detector picture of pixel index 25 to 400 at point of time $t = 0.125$ s.

6 EXPERIMENTAL VERIFICATION

The distance between pipe-outlet and detector is in a range of 25 cm. A diffracted wave on a single particle broadens with the length of this optical path. Thus, the effective signal attenuation decreases. As shown in figure 57 most attenuation has vanished. Two ways to minimize these diffraction effects are stated in the following:

1. The usage of smaller aperture diameters will remove the diffraction patterns of particles to a certain point (The diffraction caused by the aperture is not crucial).
In this experiment the diameter of aperture was $D = 500 \mu\text{m}$. The next step should be to apply smaller apertures with respect to the optical imaging quality, which is limited by the spherical aberrations of the lenses.
2. By reducing the optical path length a narrower attenuation peak will be observable. Additionally, the complete optical lens-aperture-setup should be omitted and the detector should just be put rearward the particle flow in a next step.

7 Conclusion

The maximum counting rate of currently used condensation particle counters is limited by a high probability of coincidence events. This thesis focuses on the simulation and design of new concepts for a visual-based particle counter. Setups implementing detector arrays to realize spatial resolution and in order to enhance the maximum counting limit have been investigated.

To determine the theoretical counting limit of linear detector arrays in one- and two-dimensional alignments a particle-flow simulation in *Matlab* was set up. The time resolution of detector arrays is considerably lower compared to simple photo diodes. Thus, a single linear detector array with 4000 pixels only causes a gain in performance of approximately 150%. Instead an alignment of two orthogonal detectors indicates a gain in counting limit, up to approximately 500%. Using detectors with a higher number of pixels increase the maximum counting rate even more compared to currently used photo diode setups.

To develop a visual-based particle counter including detector arrays, simulations with *Zemax* were performed to design imaging optics and determine requirements concerning detectors and light sources. In the dark field mode simple optical imaging setups did not show feasibility as the whole pipe cross-section cannot be imaged with sufficient high spatial resolution on the detector. For more complex setups like a telecentric lens or an orthogonal alignment of laser and optical axis, detector requirements, especially in terms of the critical noise level, cannot be fulfilled. A special setup, which obeys the geometric rules of "Scheimpflug", images a sufficiently high amount of light to overcome the critical noise level. Since this setup is based on a two-dimensional detector array, it is limited by the low frame rates of these camera chips. As none of the dark field setups showed high potential for realization, further considerations for a bright field alignment were given. The relative attenuation of a single particle was determined and the requirements for the detector and light source were elaborated. Due to the fact that the bright field setup showed high potential, an experiment to verify its feasibility was set up.

The results of the experiment clearly indicate that particles in the micrometer range are detectable with a setup in the bright field mode. It is highly advisable to do further investigations into this field.

8 Appendix

List of parameters:

Figure 11: Density: $\rho = 175000$ particles/cm³; Particle density distribution: $\rho(r) = 1$; Time steps: $T = 1000$; Number of pixels: $N = 4000$; Pixel size: $S = 5 \mu\text{m} \times 5 \mu\text{m}$; Width of illuminated area: $W = 10 \mu\text{m}$; Particle diameter: $D_{\text{Particle}} = 5 \mu\text{m}$; Pipe diameter, $D_{\text{Pipe}} = 2 \text{ cm}$

Figure 12: Density: $\rho = 175000$ particles/cm³; Particle density distribution: $\rho(r) = 1 - r^6$; Time steps: $T = 1000$; Number of pixels: $N = 4000$; Pixel size: $S = 5 \mu\text{m} \times 5 \mu\text{m}$; Width of illuminated area: $W = 10 \mu\text{m}$; Particle diameter: $D_{\text{Particle}} = 5 \mu\text{m}$; Pipe diameter, $D_{\text{Pipe}} = 2 \text{ cm}$

Figure 13: Density: $\rho = 175000$ particles/cm³; Particle density distribution: $\rho(r) = 1 - r^2$; Time steps: $T = 1000$; Number of pixels: $N = 4000$; Pixel size: $S = 5 \mu\text{m} \times 5 \mu\text{m}$; Width of illuminated area: $W = 10 \mu\text{m}$; Particle diameter: $D_{\text{Particle}} = 5 \mu\text{m}$; Pipe diameter, $D_{\text{Pipe}} = 2 \text{ cm}$; Pipe diameter, $D_{\text{Pipe}} = 2 \text{ cm}$

Figure 14: Densities: $\rho = 10^3 \times [0, 10, 20, 30, 40, 50, 60, 70, 80, 1000]$ particles/cm³; Particle density distribution: $\rho(r) = 1$; Time steps: $T = 250$; Number of pixels: $N = 4000$; Pixel size: $S = 5 \mu\text{m} \times 5 \mu\text{m}$; Coincidence radius: $R_{\text{coincidence}} = 15 \mu\text{m}$; Width of illuminated area: $W = 10 \mu\text{m}$; Particle diameter: $D_{\text{Particle}} = 5 \mu\text{m}$; Pipe diameter, $D_{\text{Pipe}} = 2 \text{ cm}$; Note: The high density $\rho = 1000000$ particles/cm³ was simulated to ensure low errors of the fit-coefficients of function $y(x) = a(1 - e^{-bx})$. $y(x)$ converges to 100% relative coincidence. Thus, the fit requires a value next to this limit.

Figure 15: Densities: $\rho = 10^3 \times [0, 10, 20, 30, 40, 50, 60, 70, 80, 1000]$ particles/cm³; Particle density distribution: $\rho(r) = 1 - r^6$; Time steps: $T = 250$; Number of pixels: $N = 4000$; Pixel size: $S = 5 \mu\text{m} \times 5 \mu\text{m}$; Coincidence radius: $R_{\text{coincidence}} = 15 \mu\text{m}$; Width of illuminated area: $W = 10 \mu\text{m}$; Particle diameter: $D_{\text{Particle}} = 5 \mu\text{m}$; Pipe diameter, $D_{\text{Pipe}} = 2 \text{ cm}$

Figure 16: Densities: $\rho = 10^3 \times [0, 10, 20, 30, 40, 50, 60, 70, 80, 1000]$ particles/cm³; Particle density distribution: $\rho(r) = 1 - r^2$; Time steps: $T = 250$; Number of pixels: $N = 4000$; Pixel size: $S = 5 \mu\text{m} \times 5 \mu\text{m}$; Coincidence radius: $R_{\text{coincidence}} = 15 \mu\text{m}$; Width of illuminated area: $W = 10 \mu\text{m}$; Particle diameter: $D_{\text{Particle}} = 5 \mu\text{m}$; Pipe diameter, $D_{\text{Pipe}} = 2 \text{ cm}$

Figure 17: Densities: $\rho = 10^3 \times [0, 25, 50, 75, 100, 125, 150, 175, 200]$ particles/cm³; Particle density distribution: $\rho(r) = 1$; Time steps: $T = 250$; Two detectors in an orthogonal alignment (cross-coincidence) with each $N = 4000$ pixels; Pixel size: $S = 5 \mu\text{m} \times 5 \mu\text{m}$; Coincidence

8 APPENDIX

radius: $R_{\text{coincidence}} = 15 \mu\text{m}$; Width of illuminated area: $W = 10 \mu\text{m}$; Particle diameter: $D_{\text{Particle}} = 5 \mu\text{m}$; Pipe diameter, $D_{\text{Pipe}} = 2 \text{ cm}$

Figure 18: Densities: $\rho = 10^3 \times [0, 25, 50, 75, 100, 125, 150, 175, 200]$ particles/cm³; Particle density distribution: $\rho(r) = 1 - r^6$; Time steps: $T = 250$; Two detectors in an orthogonal alignment (cross-coincidence) with each $N = 4000$ pixels; Pixel size: $S = 5 \mu\text{m} \times 5 \mu\text{m}$; Coincidence radius: $R_{\text{coincidence}} = 15 \mu\text{m}$; Width of illuminated area: $W = 10 \mu\text{m}$; Particle diameter: $D_{\text{Particle}} = 5 \mu\text{m}$; Pipe diameter, $D_{\text{Pipe}} = 2 \text{ cm}$

Figure 19: Densities: $\rho = 10^3 \times [0, 25, 50, 75, 100, 125, 150, 175, 200]$ particles/cm³; Particle density distribution: $\rho(r) = 1 - r^2$; Time steps: $T = 250$; Two detectors in an orthogonal alignment (cross-coincidence) with each $N = 4000$ pixels; Pixel size: $S = 5 \mu\text{m} \times 5 \mu\text{m}$; Coincidence radius: $R_{\text{coincidence}} = 15 \mu\text{m}$; Width of illuminated area: $W = 10 \mu\text{m}$; Particle diameter: $D_{\text{Particle}} = 5 \mu\text{m}$; Pipe diameter, $D_{\text{Pipe}} = 2 \text{ cm}$

Figure 20: Densities: $\rho = 10^3 \times [0, 80, 160, 240, 320, 400]$ particles/cm³; Particle density distribution: $\rho(r) = 1 - r^2$; Time steps: $T = 500$; Two detectors in an orthogonal alignment (cross-coincidence) with each $N = [500, 2000, 4000, 6000, 8000, 10000, 12000, 14000, 16000]$ pixels; Pixel size: $S = 5 \mu\text{m} \times 5 \mu\text{m}$; Coincidence radius: $R_{\text{coincidence}} = 15 \mu\text{m}$; Width of illuminated area: $W = 10 \mu\text{m}$; Particle diameter: $D_{\text{Particle}} = 5 \mu\text{m}$; Pipe diameter, $D_{\text{Pipe}} = 2 \text{ cm}$

Figure 22: Rectangular source, x -width: $5 \mu\text{m}$, y -width: $5 \mu\text{m}$, Analysis rays: 4×10^9 , Power: $P = 0.1 \text{ W}$, Wavelength: $\lambda = 632.8 \text{ nm}$; Particle diameter: $D_{\text{Particle}} = 5 \mu\text{m}$; Refractive index of particle: $n = 1.411$; Spherical Detector, Number of pixels: 721 (radial), 720 (angular)

Figure 24: Rectangular source, x -width: $5 \mu\text{m}$, y -width: $5 \mu\text{m}$, Analysis rays: 4×10^9 , Power: $P = 0.1 \text{ W}$, Wavelength: $\lambda = 632.8 \text{ nm}$; Particle diameters: $D_{\text{Particle}} = [0, 1, 2.5, 5, 7.5, 10, 12.5, 15, 17.5, 20] \mu\text{m}$; Refractive index of particles: $n = 1.411$; Spherical Detector, Number of pixels: 721 (radial), 720 (angular)

Figure 25: Rectangular source, x -width: 20 mm, y -width: 2 mm, Analysis rays: 4×10^9 , Power: $P = 0.1 \text{ W}$, Wavelength: $\lambda = 632.8 \text{ nm}$; Particle diameter: $D_{\text{Particle}} = 5 \mu\text{m}$; Refractive index of particle: $n = 1.411$; Position of particles $[x, y, z]$ in mm: $P_1 = [5, 0, 0]$, $P_2 = [-5, 0, 0]$; Rectangular Detector, x -width: 20 mm, y -width: 2 mm, Number of pixels: 4000×1

Figure 29: Rectangular source, x -width: 20 mm, y -width: $5 \mu\text{m}$, Analysis rays: 4×10^9 , Power: $P = 0.1 \text{ W}$, Wavelength: $\lambda = 632.8 \text{ nm}$; Particle diameter: $D_{\text{Particle}} = 5 \mu\text{m}$; Refractive index of particle: $n = 1.411$; Position of particles $[x, y, z]$ in mm: $P_1 = [2.5, 0, 0]$, $P_2 = [0, 0, 0]$, $P_3 = [-2.5, 0, -2.5]$; Rectangular Detector, x -width: 20 mm, y -width: 2 mm, Number of pixels: 4000×1 ; Lenses by *Edmund optics*: Stock No. #48182

8 APPENDIX

Figure 32: Rectangular source, x -width: 20 mm, y -width: $5\ \mu\text{m}$, Analysis rays: 4×10^9 , Power: $P = 0.1\ \text{W}$, Wavelength: $\lambda = 632.8\ \text{nm}$; Particle diameter: $D_{\text{Particle}} = 5\ \mu\text{m}$; Refractive index of particle: $n = 1.411$; Position of particles $[x,y,z]$ in mm: $P_1 = [5, 0, 0]$, $P_2 = [0, 0, 0]$, $P_3 = [-5, 0, -5]$; Rectangular Detector, x -width: 20 mm, y -width: 2 mm, Number of pixels: 4000×1 ; Lenses by *Edmund optics*: Stock No. #69456; Aperture Diameter: $D_A = 1\ \text{mm}$

Figure 34: Rectangular source, x -width: 20 mm, y -width: $5\ \mu\text{m}$, Analysis rays: 4×10^9 , Power: $P = 0.1\ \text{W}$, Wavelength: $\lambda = 632.8\ \text{nm}$; Particle diameter: $D_{\text{Particle}} = 5\ \mu\text{m}$; Refractive index of particle: $n = 1.411$; Position of particles $[x,y,z]$ in mm: $P_1 = [0, 0, 0]$, $P_2 = [5, 0, 0]$, $P_3 = [-5, 0, 0]$, $P_4 = [0.1, 0, 5]$, $P_5 = [-0.1, 0, -5]$, Rectangular Detector, Size of a single sensor element: x -width: 5 mm, y -width: 5 mm, Number of pixels: 1000×1000 ; Lenses by *Edmund optics*: Stock No. #48182

Figure 36: Rectangular source, x -width: 20 mm, y -width: $5\ \mu\text{m}$, Analysis rays: 4×10^9 , Power: $P = 0.1\ \text{W}$, Wavelength: $\lambda = 632.8\ \text{nm}$; Particle diameter: $D_{\text{Particle}} = 5\ \mu\text{m}$; Refractive index of particle: $n = 1.411$; Position of particles $[x,y,z]$ in mm: $P_1 = [0, 0, 0]$, $P_2 = [5, 0, 0]$, $P_3 = [-5, 0, 0]$, $P_4 = [0.1, 5, 5]$, $P_5 = [-0.1, -5, -5]$, Rectangular Detector, Size of a single sensor element: x -width: 5 mm, y -width: 5 mm, Number of pixels: 1000×1000 ; Lenses by *Edmund optics*: Stock No. #48260

Figure 38: Rectangular source, x -width: 20 mm, y -width: $5\ \mu\text{m}$, Analysis rays: 4×10^9 , Power: $P = 0.1\ \text{W}$, Wavelength: $\lambda = 632.8\ \text{nm}$; Particle diameter: $D_{\text{Particle}} = 5\ \mu\text{m}$; Refractive index of particle: $n = 1.411$; Position of particles $[x,y,z]$ in mm: $P_2 = [0, 0, 0]$, $P_1 = [5, 0, 5]$, $P_3 = [-5, 0, -5]$; Fiber bundle layer: $NA = 0.2$; Rectangular Detector, x -width: 20 mm, y -width: 2 mm, Number of pixels: 4000×1 ;

Figure 41: Rectangular source, x -width: 20 mm, y -width: $5\ \mu\text{m}$, Analysis rays: 4×10^9 , Power: $P = 0.1\ \text{W}$, Wavelength: $\lambda = 632.8\ \text{nm}$; Particle diameter: $D_{\text{Particle}} = 5\ \mu\text{m}$; Refractive index of particle: $n = 1.411$; Position of particles / μm : $x = z = 0$, $y = [-5.5, -5, -4, -2.5, -1.5, 0, 1.5, 2.5, 4, 5, 5.5]$; Rectangular Detector, x -width: 20 mm, y -width: 2 mm, Number of pixels: 4000×1 ; Lenses by *Edmund optics*: Stock No. #69456; Aperture Diameter: $D_A = 1\ \text{mm}$

Figure 42: Densities: $\rho = 10^3 \times [0, 25, 50, 75, 100, 125, 150, 175, 200]$ particles/cm³; Particle density distributions: $\rho(r) = 1$, $\rho(r) = 1 - r^6$, $\rho(r) = 1 - r^2$; Time steps: $T = 800$; Two detectors in an orthogonal alignment (cross-coincidence) with each $N = 4000$ pixels; Pixel size: $S = 5\ \mu\text{m} \times 5\ \mu\text{m}$; Coincidence radius: $R_{\text{coincidence}} = 15\ \mu\text{m}$; Width of illuminated area: $W = 10\ \mu\text{m}$; Particle diameter: $D_{\text{Particle}} = 2\ \text{mm}$; Pipe diameter, $D_{\text{Pipe}} = 2\ \text{cm}$; Line rates: $[1000, 5000, 7500, 10000, 12500, 15000, 17500, 20000, 22500, 25000, 30000]$ lines/s

8 APPENDIX

Figure 43: Densities: $\rho = 10^3 \times [0, 25, 50, 75, 100, 125, 150, 175, 200]$ particles/cm³; Particle density distributions: $\rho(r) = 1 - r^2$; Time steps: $T = 500$; Two detectors in an orthogonal alignment (cross-coincidence) with each $N = [1000, 2000, 3000, 4000, 6000, 8000]$ pixels; Pixel size: $S = 5 \mu\text{m} \times 2000 \mu\text{m}$; Coincidence radius: $R_{\text{coincidence}} = 15 \mu\text{m}$; Width of illuminated area: $W = 10 \mu\text{m}$; Particle diameter: $D_{\text{Particle}} = 5 \mu\text{m}$; Pipe diameter, $D_{\text{Pipe}} = 2 \text{cm}$; Line rates: $[1000, 5000, 10000, 12500, 15000, 17500, 20000, 25000, 30000]$ lines/s

Figure 44: Densities: $\rho = 10^3 \times [0, 50, 100, 150, 200, 250, 300]$ particles/cm³; Particle density distributions: $\rho(r) = 1 - r^2$; Time steps: $T = 800$; Two detectors in an orthogonal alignment (cross-coincidence) with each $N = 4000$ pixels; Pixel size: $S = 5 \mu\text{m} \times 2000 \mu\text{m}$; Coincidence radius: $R_{\text{coincidence}} = 15 \mu\text{m}$; Width of illuminated area: $W = [0.5 * 10^{-3}, 1.0 * 10^{-3}, 1.5 * 10^{-3}, 2.0 * 10^{-3}, 2.5 * 10^{-3}, 3.0 * 10^{-3}] \text{cm}$, Divergence angle: $\phi = 0^\circ$; Particle diameter: $D_{\text{Particle}} = 5 \mu\text{m}$; Pipe diameter, $D_{\text{Pipe}} = 2 \text{cm}$; Line rates: $[1000, 5000, 10000, 15000, 20000, 25000, 30000]$ lines/s

Figure 45: Densities: $\rho = 10^3 \times [0, 50, 100, 150, 200, 250, 300]$ particles/cm³; Particle density distributions: $\rho(r) = 1 - r^2$; Time steps: $T = 800$; Two detectors in an orthogonal alignment (cross-coincidence) with each $N = 4000$ pixels; Pixel size: $S = 5 \mu\text{m} \times 2000 \mu\text{m}$; Coincidence radius: $R_{\text{coincidence}} = 15 \mu\text{m}$; Width of illuminated area: $W = 10^{-3} \text{cm}$, Divergence angle: $\phi = [0, 0.05, 0.1, 0.15, 0.2, 0.25]^\circ$; Particle diameter: $D_{\text{Particle}} = 5 \mu\text{m}$; Pipe diameter, $D_{\text{Pipe}} = 2 \text{cm}$; Line rates: $[1000, 5000, 10000, 15000, 20000, 25000, 30000]$ lines/s

Figure 48: Rectangular source, x -width: 20 mm, y -width: $5 \mu\text{m}$, Analysis rays: 4×10^9 , Power: $P = 0.1 \text{W}$, Wavelength: $\lambda = 632.8 \text{nm}$; Particle diameter: $D_{\text{Particle}} = 5 \mu\text{m}$; Refractive index of particle: $n = 1.411$; Position of particles $[x, y, z]$ in mm: $P_1 = [0, 0, 0]$, $P_2 = [5, 0, 0]$, $P_3 = [-5, 0, 0]$; Rectangular Detector, x -width: 20 mm, y -width: $5 \mu\text{m}$, Number of pixels: 4000×1 ; Lenses by *Edmund optics*: Stock No. #69445; Aperture Diameter: $D_A = 1 \text{mm}$

Figure 50: Particle diameter: $D_{\text{Particle}} = 5 \mu\text{m}$; Refractive index of particle: $n = 1.411$; Beam definition: Gaussian beam, x - and y -size: 0.01 mm; x - and y -angle: 0.1° , Distance particle-detector: 10 mm

Figure 51: Rectangular source, x -width: 20 mm, y -width: $5 \mu\text{m}$, Analysis rays: 4×10^9 , Power: $P = 0.1 \text{W}$, Wavelength: $\lambda = 632.8 \text{nm}$; Particle diameters: $D_{\text{Particle}} = [2.5, 5, 7.5] \mu\text{m}$; Refractive index of particles: $n = 1.411$; Position of particles / μm : $x = z = 0$ $y = [-7.5, -5.0, -4.0, -2.5, -1.0, 0.0, 1.0, 2.5, 4.0, 5.0, 7.5,]$; Rectangular Detector, x -width: 20 mm, y -width: $5 \mu\text{m}$, Number of pixels: 4000×1 ;

Section 2.3.3: Densities: $\rho = 10^3 \times [0, 5, 10, 15, 20, 25, 30]$ particles/cm³; Time steps: $T = 1000$; Number of pixels: $N = 1$; Width of illuminated area: $W = 10 \mu\text{m}$; Particle diameter:

8 APPENDIX

$D_{\text{Particle}} = 5 \mu\text{m}$; Pipe diameter, $D_{\text{Pipe}} = 2 \text{ cm}$

Table 1: Densities: $\rho = 10^3 \times [0, 10, 20, 30, 40, 50, 60, 70, 80, 1000]$ particles/cm³; Time steps: $T = 250$; Number of pixels: $N = 4000$; Pixel size: $S = 5 \mu\text{m} \times 5 \mu\text{m}$; Coincidence radius: $R_{\text{coincidence}} = 15 \mu\text{m}$; Width of illuminated area: $W = 10 \mu\text{m}$; Particle diameter: $D_{\text{Particle}} = 5 \mu\text{m}$; Pipe diameter, $D_{\text{Pipe}} = 2 \text{ cm}$

Table 2: Densities: $\rho = 10^3 \times [0, 25, 50, 75, 100, 125, 150, 175, 200]$ particles/cm³; Time steps: $T = 250$; Two detectors in an orthogonal alignment (cross-coincidence) with each $N = 4000$ pixels; Pixel size: $S = 5 \mu\text{m} \times 5 \mu\text{m}$; Coincidence radius: $R_{\text{coincidence}} = 15 \mu\text{m}$; Width of illuminated area: $W = 10 \mu\text{m}$; Particle diameter: $D_{\text{Particle}} = 5 \mu\text{m}$; Pipe diameter, $D_{\text{Pipe}} = 2 \text{ cm}$

Table 2: Densities: $\rho = 10^3 \times [0, 25, 50, 75, 100, 125, 150, 175, 200]$ particles/cm³; Time steps: $T = 500$; Two detectors in an orthogonal alignment (cross-coincidence); Pixel size: $S = 5 \mu\text{m} \times 5 \mu\text{m}$; Coincidence radius: $R_{\text{coincidence}} = 15 \mu\text{m}$; Width of illuminated area: $W = 10 \mu\text{m}$; Particle diameter: $D_{\text{Particle}} = 5 \mu\text{m}$; Pipe diameter, $D_{\text{Pipe}} = 2 \text{ cm}$, Laminar velocity distribution: $v(r) = 1 - r^2$;

REFERENCES

References

- [1] Kulkarni, P., Baron, P. A., & Willeke K., (2012). *Aerosol Measurement: Principles, Techniques, and Applications*. New Jersey, *Hoboken: Wiley*.
- [2] Aitken, J. (1920). *Collected Scientific Papers*, ed. G.G.Knott. (London: College University)
- [3] Vonnegut, B. (1949). A continuous recording condensation nuclei matter. *First National Air Pollution Symposium*, Los Angeles, CA, pp. 36-44
- [4] Rich, T.A. (1966). Apparatus and method for measuring the size of aerosols. *J. Rech. Atmos*, 2:79-85
- [5] Skala, G.F. (1963). An automatic Aitken nuclei counter. *Anal. Chem.*, 35:702-706
- [6] AVL List Gmabh. (2014). (*AVL Particle Counter*, Retrieved May 10, 2014 from <https://www.avl.com/particle-counter>
- [7] Stemmer, Ch., *Grenzschichttheorie* (Lecture notes, TU München). Retrieved September 24, 2013 from <http://www.aer.mw.tum.de/fileadmin/tumwaer/www/pdf/lehre/grenzschicht/skript.pdf>
- [8] Ham, J. H. (2003). *Zur Berechnung der Verweilzeitverteilung von Partikeln* (Doctoral dissertation, Universität Duisburg-Essen). Retrieved September 24, 2013 from <http://www.qucosa.de/fileadmin/data/qucosa/documents/4727/data/hamDiss.pdf>
- [9] LSTM Erlangen. *Rohrströmungen* .Retrieved September 24, 2013 from <http://www10.informatik.uni-erlangen.de/Teaching/Courses/SS2011/CE2/lecture/Rohrstroemungen.pdf>]
- [10] The University of Manchester (2012). *Condensation Particle Counters (CPC)* (Centre for Atmospheric Science). Retrieved September 24, 2013 from <http://www.cas.manchester.ac.uk/restools/instruments/aerosol/cpc/>
- [11] V. S. Hering and F. R. a. O. D. R. Stolzenberg, Mark R. an Quant, (2007). "Laminar-Flow, Water- Based Condensation Particle Counter (WCPC)". *Aerosol Science and Technology*
- [12] Evertz, H. G. (WS 2009). *Computer Simulations* (Lecture notes, TU Graz). Retrieved September 24, 2013 from <http://itp.tugraz.at/~evertz/Computersimulationen/cs2009.pdf>

REFERENCES

- [13] Sager, Ch. (2007). *Der Partikeltransport in turbulent durchströmten Rohrleitungen und seine besondere Bedeutung für die Partikelmesstechnik* (Doctoral dissertation, Universität Duisburg-Essen). Retrieved September 24, 2013 from <http://duepublico.uni-duisburg-essen.de/servlets/DocumentServlet?id=15551>
- [14] Wikipedia. (2013). *Decane*. Retrieved November 18, 2013 from <http://en.wikipedia.org/wiki/Decane>
- [15] Palas. (2014). *AGK 2000 - datasheet*. Retrieved May 15, 2014 from <http://www.palas.de/de/product/agk2000#datasheet>
- [16] Mie-Streuung. (2013). Retrieved November 19, 2013 from <http://de.wikipedia.org/wiki/Mie-Streuung>
- [17] Wikipedia. (2013). *Bright-field microscopy*. Retrieved November 19, 2013 from http://en.wikipedia.org/wiki/Bright-field_microscopy
- [18] Wikipedia. (2013). *Dark-field microscopy*. Retrieved November 19, 2013 from http://en.wikipedia.org/wiki/Dark_field_microscopy
- [19] Radiant Zemax. (2014). *Zemax Manual*. Retrieved May 15, 2014 from <http://physics.ucsd.edu/C38F1FA1-023D-4B0D-B7B5-A3FA8D0D42B1/FinalDownload/DownloadId-D2271A280D3165DA0086F049C535583F/C38F1FA1-023D-4B0D-B7B5-A3FA8D0D42B1/neurophysics/Manuals/Zemax/ZemaxManual.pdf>
- [20] Radiant Zemax. (2014). *Sequential Ray Tracing*. Retrieved May 15, 2014 from <http://www.zemax.com/products/opticstudio/feature-explorer/optical-system-design/sequential-ray-tracing>
- [21] Radiant Zemax. (2014). *Non-Sequential Ray Tracing*. Retrieved May 15, 2014 from <http://www.zemax.com/products/opticstudio/feature-explorer/illumination-system-design/non-sequential-ray-tracing>
- [22] Ukiva. (2013). *What is sensitivity and why are sensitivity statements often misleading?*. Retrieved December 12, 2013 from <http://www.ukiva.org/vision-system-application-articles/multipix.html>
- [23] Ted Pella. (2009). *Background Information on CCD and CMOS Technology*. Retrieved January 09, 2013 from http://www.tedpella.com/cameras_html/ccd_cmos.htm

REFERENCES

- [24] Dalsa. (2013). *CCD vs. CMOS, Facts and Fiction*. Retrieved January 09, 2013 from http://www.dalsa.com/shared/content/Photonics_Spectra_CCDvsCMOS_Litwiller.pdf
- [25] Marc Winter. (2011). *Introduction to CMOS Pixel Sensors*, EDIT School - CERN. Retrieved January 09, 2013 from <https://indico.cern.ch/getFile.py/access?contribId=4&resId=0&materialId=slides&confId=124393>
- [26] Bhautik, J. (2010). *How do tilt shift lenses work?*. Retrieved March 28, 2014 from <http://cow.mooh.org/projects/tiltshift/howdoesitwork.html>